JOHANNES GUTENBERG UNIVERSITÄT MAINZ

DOCTORAL THESIS

Structure, Dynamics and Vibrational Spectroscopy of Interfacial Alkali Nitrate Aqueous Solutions from *ab initio* Molecular Dynamics

---

Author:
Gang HUANG

Supervisor:
Apl. Prof. Dr. Marialore SULPIZI

A thesis submitted in fulfillment of the requirements
for the degree of Doctor of Philosophy

in the

Condensed Matter Theory Group
Institute for Physics

November 26, 2020

Declaration of Authorship

I, Gang Huang, declare that this thesis titled, "Structure, Dynamics and Vibrational Spectroscopy of Interfacial Alkali Nitrate Aqueous Solutions from *ab initio* Molecular Dynamics" and the work presented in it are my own. I confirm that:

- This work was done wholly or mainly while in candidature for a research degree at this University.
- Where any part of this thesis has previously been submitted for a degree or any other qualification at this University or any other institution, this has been clearly stated.
- Where I have consulted the published work of others, this is always clearly attributed.
- Where I have quoted from the work of others, the source is always given. With the exception of such quotations, this thesis is entirely my own work.
- I have acknowledged all main sources of help.
- Where the thesis is based on work done by myself jointly with others, I have made clear exactly what was done by others and what I have contributed myself.

Signed:

Date:

“*The accurate description of water has been and continues to be a challenge for both experiment and simulations due to the directional nature and the weakness of the hydrogen bonds in conjunction with its autodissociation properties.*”

Dominik Marx and Jürg Hutter

“*If a problem is worth looking at at all, then no mathematical technique is to be judged too sophisticated.*”

David Ruelle

JOHANNES GUTENBERG UNIVERSITÄT MAINZ

Abstract

Condensed Matter Theory
Institute for Physics

Doctor of Philosophy

Structure, Dynamics and Vibrational Spectroscopy of Interfacial Alkali Nitrate Aqueous Solutions from *ab initio* Molecular Dynamics

by Gang Huang

I have analyzed the interfacial structure and dynamics of solutions containing alkali nitrates by Density Functional Theory-based Molecular Dynamics (DFTMD) simulations. In particular I have presented a detailed analysis of the Hydrogen Bond (HB) structure at the interface and have calculated the interface vibrational spectra in order to provide a molecular interpretation of available experimental data. As a first system I have analyzed the behaviour of a salty water/vapor interface containing $LiNO_3$. Both the measured and calculated Vibrational Sum-Frequency Generation (VSFG) spectra shows a reduced intensity of the lower frequency portion region, when compared to the pure water/vapor interface. This reduction is attributed to the H-bonds established between the NO_3^- and the surrounding water molecules at the interface. This effects is only related to the presence of NO_3^- at the water surface and is not affected by the presence of alkali metal ions. I have shown that the use of simple models, such as small cluster is not suitable to reproduce the experimental spectra and cannot provide a microscopic interpretation of the spectra. Realistic models of the interface are required to address the perturbation of the ion on the water surface.

The difference between the HB dynamics outside the first shell of the Li^+ and that of nitrate-water Hydrogen (H-) bonds at interfaces is not visible from the values of the HB relaxation time. They reflect the difference between HB dynamics in bulk water and that at the water/vapor interfaces. For the water/vapor interface of alkaline iodine solutions, I find that the cations does not alter the H-bonding network outside the first hydration shell of cations. It is concluded that no long-range structural-changing effects for alkali metal cations.

From the results of nonlinear susceptibilities, I conclude that these water molecules at the water/vapor interfaces of LiI, NaI, and KI solutions are participating in weaker H-bonds, compared with those at the pure water surface. The origin of the characteristics may come from a unique distribution of I^- ions and alkali metal cations, which form a double layer over the thickness on the order of 5–10 Å.

For the bulk and interfacial systems, I calculated the correlation functions of the hydrogen bond (HB) population, and obtained the reaction rate constants with the HB formation and breakage. To analyze the HB dynamics on the interface, we propose a statistical method which is based on the instantanous interface HB population for the instantaneous interface. With the help of instantaneous HB population operator, one do not need to know which molecules are within the instantaneous interface, so there is no need to select the molecules on the interface and calculate the statistical average of physical quantities. Except for the case where the interface thickness is low, this method can efficiently analyze the HB dynamics of the instantaneous interface. And it can be easily applied to general interface systems or aqueous solutions.

Acknowledgements

I wish to express my sincere gratitude to my supervisor, Prof. Dr. Marilore Sulpizi for her excellent guidance during my research, and her detailed and valuable advice for my writing. I thank her for bringing me into interesting and novel areas of density functional theory-based molecular dynamics simulation and interface physics and chemistry. By communicating with her, I was implicitly and positively affected. She is rigorous in academic studies, optimistic and active, and has a wide range of interests. All these have kept in my heart and gave me greater confidence in future scientific research work.

I wish to thank Prof. Dr. Thomas Kühner, Dr. Giovanni Settanni, PD Dr. Peter Virnau, Dr. Hans Behringer and Prof. Dr. Thomas Speck in the Institute for Physics for leading me to the fundamental statistical physics and excellent lectures and discussions. I am grateful to Prof. Dr. Friederike Schmid and Prof. Dr. Kurt Binder for their talks and guidance.

I am grateful to Dr. Rémi Khatib for programing skills and helpful guidance on the programs for calculating the VSFG spectra. I also thank Dr. Shuanhu Qi, Dr. Jiajia Zhou and Dr. Fei Yu for useful discussions on the the calculation of response functions. I would like to thank Leila Salimi, Isidro Lorenzo Geada, Santosh Kumar Meena and Anusha Lalitha, at the Institute for Physics, for their encouragement and assistance.

I thank Prof. Honggang Luo and Prof. Haiping Fang for their great help in my study during my PhD. The cooperation and discussions with Dr. Guosheng Shi, Dr. Bo Zhou and Dr. Chunlei Wang have benefited me a lot. I express my sincere thanks to them.

I thank Prof. Dr. Yuliang Jin for his support, trust and teachings over the past year.

I am also grateful to my parents Yuhua Diao and Dehuai Huang and my brother Jialiang for his care, understanding and support for me in the past few years. I am especially grateful to my dear parents, who have worked hard for decades and nurtured me.

The financial supports of the China Scholarship Council and TRR146 are gratefully acknowledged.

Contents

Declaration of Authorship iii

Abstract viii

Acknowledgements ix

1 Introduction 1

2 Methods 3
- 2.1 Modeling Interfaces with *ab initio* Molecular Dynamics . . . 3
- 2.2 Density Functional Theory . . . 4
- 2.3 Born-Oppenheimer Molecular Dynamics . . . 9
- 2.4 Vibrational Density of States . . . 11
- 2.5 Calculation of VSFG Spectroscopy for Water/Vapor Interfaces . . . 11
  - 2.5.1 Nonlinear Susceptibility of Water Molecules at Water/Vapor Interfaces . . . 12
  - 2.5.2 Sum Frequency Generation Spectra from Velocity-Velocity Correlation Functions . . . 14

3 Experimental SFG spectra of salty interfaces 17

4 Alkali Nitrate Clusters 19
- 4.1 Cluster of Nitrate and Water Molecules . . . 19
- 4.2 Cluster of Alkali Metal Cation and Water Molecules . . . 20
- 4.3 Clusters of Alkali Nitrate and Water Molecules . . . 21

5 VSFG Spectroscopy of Water/Vapor Interfaces 25
- 5.1 VSFG Spectra of the Interface of $LiNO_3$ Aqueous Solutions . . . 26
- 5.2 VSFG Spectra of the Interface of Alkali Iodine Aqueous Solutions . . . 30

6 Hydrogen Bond Dynamics of Water/Vapor Interfaces 35
- 6.1 Definitions of Hydrogen Bond Population and Correlation Functions . 35
- 6.2 Distribution of Hydrogen Bond Lifetimes . . . 41
- 6.3 Water-water Pair Based Hydrogen Bond Dynamics . . . 45

7 Summary 55

A Calculation of Nonlinear Optical Susceptibilities 57

B Structural Characterization of Water Clusters 61

C Propensities of Ions 65
- C.1 Free Energy of the Water Separated and the Contact Ion Pair . . . 65
- C.2 Surface Tension Increment . . . 65
- C.3 Gibbs surface excess . . . 66

D Thickness of the Interface of the Aqueous Solutions **71**

E HB Lifetime Distributions and Instantaneous Interfaces **75**
  E.1 Relations between HB Lifetime Distributions 75
  E.2 Dynamics of Interfacial Hydrogen Bonds 79

Bibliography **81**

List of Figures

2.1 The schematic of the VSFG process which involves IR and Raman transitions. The $\nu = 0$, $\nu = 1$ levels denote the ground and the first excited state of the oscillator, respectively. The dashed line denotes a virtual electronic state in the Raman transition. 12
2.2 The representation of the bond (a) and the molecular (b) frameworks. (from Ref. [117]) 16

3.1 Experimental VSFG intensity of $LiNO_3$ solutions, compared with that of neat water. [130] 18

4.2 The VDOS for the two OH bonds in w1 (Fig. 4.1(a)) of $[NO_3{\cdot}(H_2O)_3]^-$. 19
4.1 The geometry optimized structure of the clusters: (a) $[NO_3{\cdot}(H_2O)_3]^-$; (b) $RNO_3(H_2O)_3$; (c) $RNO_3(H_2O)_4$; (d) $RNO_3(H_2O)_5$ (R=Li,Na,K). More structural properties are shown in Appendix B. 20
4.3 The cluster $[Li{\cdot}(H_2O)_4]^-$. 20
4.4 The RDFs $g_{\text{Li-O}}$ and $g_{\text{Li-H}}$ for the cluster $[Li{\cdot}(H_2O)_4]^-$. 20
4.5 The VDOS for the four water molecules (all water molecules) in the cluster $[Li{\cdot}(H_2O)_4]^-$. 21
4.6 The VDOS for the water molecules bound to Li (three water molecules) in the cluster $[Li{\cdot}(H_2O)_4]^-$. 21
4.7 (a) The RDF $g_{\text{R-O}}$ for clusters $RNO_3(H_2O)_3$ (R=Li, Na, K); (b) The RDF $g_{\text{O-H}}$ for clusters $RNO_3(H_2O)_3$ and $[NO_3{\cdot}(H_2O)_3]^-$ (no alkali metal cation). 22
4.8 The VDOS for each water molecule in the cluster $LiNO_3(H_2O)_n$: (a) $n = 3$; (b) $n = 4$; (c) $n = 5$. w1: H_2O bound to Li and H_2O; w2: H_2O bound to nitrate and H_2O; w3: H_2O bound to Li and nitrate; w4: H_2O bound to H_2O; w5: H_2O only bound to Li. 22
4.9 The VDOS for water molecules in clusters (a) $LiNO_3(H_2O)_3$, (b) $NaNO_3(H_2O)_3$ and (c) $KNO_3(H_2O)_3$. w1: H_2O bound to R and H_2O; w2: H_2O bound to nitrate and H_2O; w3: H_2O bound to R and nitrate. 23

5.1 The water/vapor interfaces of $LiNO_3$ solution and pure water. The right panel shows that the Li^+ and the NO_3^- ions are separated by a water molecule at the salty interface. 25
5.2 The probability distributions of ions and water molecules for $LiNO_3$ water interface along the normal direction, through the trajectory of 40 ps. 26
5.3 (a) The Im$\chi^{(2),\text{R}}_{SSP}$ and (b) the $|\chi^{(2),\text{R}}_{SSP}|^2$ of water molecules at water/vapor interface of $LiNO_3$ solution. The simulation time: 40 ps; d=9 Å. . . . 27
5.4 The VDOS $g_z(\nu)$ of water molecules in the water/vapor interface of $LiNO_3$ solution (solid line) and in vapor-pure water interface (dashed line). (a): $d = 1$ Å; (b): $d = 2$ Å; (c): $d = 5$ Å. 27

5.5 The VDOS for 6 water molecules bound to NO_3^- in vapor/$LiNO_3$ solution interface (salty water) and that for 15 water molecules at the top layer (d=1 Å) of the neat water. 28

5.6 The free energy profile with respect to the distance r between Li^+ and the nitrogen in NO_3^- in the cluster $LiNO_3(H_2O)_{30}$. A: configuration A where $r = 2.9$ Å; B: configuration B where $r = 4.3$ Å; C: the transition states. 29

5.7 The probability distributions $P(z)$, along the normal direction, of Li^+, I^- and O in LiI solution-air interface, through the trajectory of 60 ps. 30

5.8 (a) The RDF $g_{\text{Li-O}}$ and $g_{\text{Li-H}}$ for LiI–water interface. The first two peaks of $g_{\text{Li-O}}$ and $g_{\text{Li-H}}$: 1.97 and 4.12 Å, and, 2.61 and 4.73 Å, respectively. (b)The RDF $g_{\text{I-O}}$ and $g_{\text{I-H}}$ for LiI-water interface. The first two peaks of $g_{\text{I-O}}$ and $g_{\text{I-H}}$: 3.62 and 5.28 Å; and, 2.69 and 4.11 Å, respectively. 31

5.9 (a) The RDF $g_{\text{Na-O}}$ and $g_{\text{Na-H}}$ for NaI–water interface. The first two peaks of $g_{\text{Na-O}}$ and $g_{\text{Na-H}}$: 2.41 and 4.55 Å, and, 3.02 and 4.96 Å, respectively. (b)The RDF $g_{\text{I-O}}$ and $g_{\text{I-H}}$ for NaI-water interface. The first two peaks of $g_{\text{I-O}}$ and $g_{\text{I-H}}$: 3.59 and 5.04 Å; and, 2.63 and 4.15 Å, respectively. 32

5.10 (a) The RDF $g_{\text{K-O}}$ and $g_{\text{K-H}}$ for KI–water interface. The first two peaks of $g_{\text{K-O}}$ and $g_{\text{K-H}}$: 2.84 and 4.71 Å, and, 3.40 and 5.51 Å, respectively. (b)The RDF $g_{\text{I-O}}$ and $g_{\text{I-H}}$ for KI-water interface. The first two peaks of $g_{\text{I-O}}$ and $g_{\text{I-H}}$: 3.59 and 5.43 Å; and, 2.65 and 4.10 Å, respectively. 32

5.11 The (a) $\text{Im}\chi_{SSP}^{(2),\text{R}}$ and (b) $|\chi_{SSP}^{(2),\text{R}}|^2$ of the water/vapor interface of 0.9 M NaI solution (solid line) and pure water/vapor (dashed line) interface. The data for pure water/vapor interface is calculated from the DFTMD simulation for the water interface with the same thickness (5 Å) at the same temperature (330 K). The same below. 33

5.12 The (a) $\text{Im}\chi_{SSP}^{(2),R}$ and (b) $|\chi_{SSP}^{(2),\text{R}}|^2$ of the water/vapor interface of 0.9 M LiI solution (solid line) and pure water/vapor interface (dashed line). 33

5.13 The (a) $\text{Im}\chi_{SSP}^{(2),R}$ and (b) $|\chi_{SSP}^{(2),\text{R}}|^2$ of the water/vapor interface of 0.9 M KI solution (solid line) and pure water/vapor interface (dashed line). 33

5.14 $\text{Im}\chi_{XXZ}^{(2),R}$ (black solid) and $\text{Im}\chi_{YYZ}^{(2),R}$ (grey solid) spectra are very close, because the interfaces have rotational symmetry about the z-axis. . . 34

6.1 The dynamics of $r_{\text{OO}}(t)$ (top), $\cos\phi(t)$ (middle), and $h(t)$ (bottom) for a HB in a water cluster. The dashed lines show the interoxygen distance boundary r_{OO}^{c}=3.5 Å (top) and criterion of cosine of H−O$\cdots$O angle $\cos\phi^{\text{c}}$ with ϕ^{c}=30°, respectively. 37

6.2 The time dependence of $C_{\text{HB}}(t)$ ($c(t)$ for short)for the DFTMD simulated bulk water at 300 K with density $\rho = 1.00$ g/cm^3. Ref:[186] . . . 37

6.3 The time dependence of $S_{\text{HB}}(t)$ (denoted by $s(t)$ for short) for the DFTMD simulated bulk water at 300 K with density $\rho = 1.00$ g/cm^3. 38

6.4 The partial RDFs of liquid water at ambient conditions. (a) Bulk water (box size: 15.64 × 15.64 × 15.64 Å^3; $T = 300$ K); (b) water/vapor interface (box size: 15.64 × 15.64 × 31.28 Å^3; $T = 300$ K). 40

6.5 Time dependence of the correlation functions (a) $n(t)$, $c(t)$ and (b) the rate function $k(t)$ of water–water H-bonds for *bulk* water, calculated from the trajectory of a DFTMD simulation. The definition of $h(t)$ is based on specific H–O bond, instead of water-water pairs. The simulation was for bulk water at $T = 300$ K, and with a density of 1.00 g cm^{-3}. The length of the trajectory is 50 ps of physical time. 40

6.6 Time dependence of the correlation functions (a) $n(t)$, $c(t)$ and (b) the $k(t)$ of water–water H-bonds for water/vapor *interface* at 300 K, calculated from the trajectory of a DFTMD simulation. The definition of $h(t)$ is based on specific H–O bond, instead of water-water pairs. The length of the trajectory is 50 ps of physical time. 40

6.7 Time dependence of the correlation functions $k(t)$ of water–water H-bonds for (a) bulk water and (b) water/vapor interface at 300 K. . . . 41

6.8 The H-bonds with lifetime τ in a certain configuration. At time t, we assume that there are totally n_{tot} H-bonds can be detected, and n_τ H-bonds are of lifetime τ, therefore, the fraction of H-bonds that have the lifetime τ in the configuration at time t is $P_{tc}(\tau) = n_\tau/n_{tot}$. Let τ take all the values in the interval $[0, \infty]$, we can get the HB lifetime distribution $P_{tc}(t)$. 42

6.9 The time dependence of the population functions $n(t)$ for (a) bulk water and (b) water/vapor interface, as computed from the ADH (solid line) and AHD (dashed line) criterion of H-bonds with the expression $n(t) = \int_0^t dt' k_{in}(t')$. 42

6.10 A slab of LiNO$_3$ solution with the instantaneous interface **s** represented as a blue mesh on the upper and lower phase boundary. The initial position of each ion in the solution is random. The slab is periodically replicated in the horizontal directions. 44

6.11 The time dependence of (a) $C_{\mathrm{HB}}(t)$ and (b) ln$S_{\mathrm{HB}}(t)$ of all water–water and nitrate–water H-bonds at 300 K for the slab of LiNO$_3$ solution, as computed from the ADH (solid line) and AHD (dashed line) criterion of H-bonds. The definition of the correlation function is based on the specific HB configuration between molecules. 44

6.12 The correlation functions $C_{\mathrm{HB}}(t)$ for bulk water, based on water-water pair HB population operator $h(t)$, as computed from the ADH (solid line) and AHD (dashed line) criterion of H-bonds. 45

6.13 The correlation functions $C^s_{HB}(t)$ for the instantaneous interfacial H-bonds, based on water-water pair HB population operator $h^s(t)$, as computed from the (a) ADH and (b) AHD criterions of H-bonds. . . . 47

6.14 The correlation functions $C_{\mathrm{HB}}(t)$ for the instantaneous interfacial H-bonds, based on water-water pair HB population operator $h(t)$, as computed from the (a) ADH and (b) AHD criterions of H-bonds. These results are based on selecting the water molecules in the interface and then averaging the HB dynamics of these water molecules. Sampling is performed every 4 ps. 47

6.15 The dependence of (a) the rate constants k and k' and (b) the lifetime τ_{HB} on the interface thickness, obtained by the Instantaneous interface Hydrogen Bond (IHB) and by selecting the water molecules in the interface, respectively. The corresponding k, k' and τ_{HB} in the bulk water are also drawn with dashed lines as a reference. In sub-figure (a), the k of bulk water is represented by a *black dashed* line, and its k' is represented by a *blue dashed* line; in sub-figure (b), the τ_{HB} of bulk water is represented by a *black dashed* line. The constants are calculated based on the ADH criterion of H-bonds and the least square fits are carried on the time region 0.2 ps $< t <$ 12 ps. 48
6.16 The distances between ions and the instantaneous surfaces (blue meshes) for a slab of aqueous $\mathrm{LiNO_3}$ solution. 51
6.17 Time dependence of the cation–surface and nitrate–surface distances at 300 K. 51
6.18 (a)Li–water O, Li–water H RDFs; (b) Nitrate O–water O, nitrate O-water H RDFs for $\mathrm{LiNO_3}$ solutions at 300 K. 52
6.19 Time dependence of the intermittent correlation functions $C_{\mathrm{HB}}(t)$ of $\mathrm{I^-}$–water ($\mathrm{I^-}$–W) and water–water H-bonds at 300 K. A base-10 log scale is used for the x-axis. 52
6.20 Time dependence of the continuous correlation functions $S_{\mathrm{HB}}(t)$ of $\mathrm{I^-}$–water ($\mathrm{I^-}$–W) and water–water H-bonds at 300 K. 53
6.21 Time dependence of the correlation functions $n_{\mathrm{HB}}(t)$ of $\mathrm{I^-}$–water ($\mathrm{I^-}$–W) and water–water H-bonds at 300 K. 53
6.22 Time dependence of the correlation functions $n_{\mathrm{HB}}(t)$ of $\mathrm{I^-}$–water ($\mathrm{I^-}$–W) and water–water H-bonds at 300 K. A base-10 log scale is used for the x-axis. 54

B.1 The nitrate O ($\mathrm{O_n}$)–water O ($\mathrm{O_w}$) and nitrate O–water H ($\mathrm{H_w}$) RDFs for $[\mathrm{NO_3{\cdot}(H_2O)_3}]^-$. The peaks for the former are 1.93, 2.95 and 3.95 Å, and for the later are 2.95 and 4.80 Å. 62
B.2 The VDOS $g(\nu)$ for water molecules in the cluster $[\mathrm{NO_3{\cdot}(H_2O)_3}]^-$ at 100 K shows that the vibrational peaks for the three water molecules are very close to each other ($\Delta\nu <$ 10 $\mathrm{cm^{-1}}$)for both vibrational and bending modes. 63
B.3 The comparison between the VDOS for H and of a whole water molecule, for a water molecule (w1, Fig. 4.1a), in $[\mathrm{NO_3{\cdot}(H_2O)_3}]^-$ at 300 K. . . . 63

D.1 The calculated $|\chi^{(2),\mathrm{R}}_{SSP}|^2$, of water molecules at the aqueous/vapor interfaces with different thickness. This calculation is done for a model for the water/vapor interface where a slab of 117 water molecules containing one $\mathrm{Li^+}$ and one $\mathrm{NO_3^-}$ is included in a period simulation box of 15.60 Å ×15.60 Å ×31.00 Å at 300 K. 71
D.2 The calculated $|\chi^{(2),R}_{SSP}|^2$, of water molecules at water/vapor interfaces with different thickness. This calculation is done for a model for water/vapor interface where a slab of 118 water molecules containing one $\mathrm{Li^+}$ and one $\mathrm{I^-}$ is included in a period simulation box of 15.60 Å × 15.60 Å × 31.00 Å. 71

D.3 The RDF $g_{\mathrm{OH}}(r)$ in the NaI solution/vapor interface. The simulation system includes one Na^{+} ion, one I^{-} ion, and 124 water molecules in 15.60 Å × 15.60 Å × 31.00 Å simulation box. The solid and dashed lines are corresponding to one of the two interfaces in our simulation, respectively. The simulation time is 22.5 ps. 72

D.4 The logarithms of the function $S_{\mathrm{HB}}(t)$ for water-water H-bonds at interfaces with different thickness in 0.9 M LiI solution. 72

D.5 The resolution dependence of the continuum lifetime τ_{HB} of water–water H-bonds at interfaces of different 0.9 M alkali-iodine solutions at 330 K, calculated for six temporal resolutions (t_t). [212–214] For $t_t = 5$ fs, the calculated continuum HB lifetime is 0.30 ps, 0.31 ps and 0.23 ps, for the interface of LiI, NaI and KI solution, respectively. . . . 73

E.1 The correlation functions $C_{HB}(t)$ of water molecules in bulk water. Here $h(t)$ is based on two different definitions, one is based on a pair of water molecules (solid line), and the other is based on O–H pairs between water molecules (dashed line). 78

List of Tables

4.1 The average length r_a of H-bonds (Li-O bonds) in the cluster $LiNO_3(H_2O)_3$. 22

5.1 The peaks of $g_{\text{Li-O}}$ and $g_{\text{Li-H}}$ for 0.9 M LiI solution at 330 K. (unit:Å, the same below) . . . 31
5.2 The peaks of $g_{\text{Na-O}}$ and $g_{\text{Na-H}}$ for 0.9 M NaI solution at 330 K. 31
5.3 The peaks of $g_{\text{K-O}}$ and $g_{\text{K-H}}$ for 0.9 M KI solution at 330 K. 31

6.1 The k and k' for the bulk water and the water/vapor interface. We carried on the short time region 0.2 ps $< t <$ 2 ps. The unit for k (k') is ps^{-1}, and that for τ_{HB} ($= 1/k$) is ps. 43
6.2 The k and k' for the bulk water and the water/vapor interface. We carried on the long time region 2 ps $< t <$ 12 ps. The unit for k (k') is ps^{-1}, and that for τ_{HB} ($= 1/k$) is ps. 43
6.3 The k and k' for the interfacial hydrogen dynamics of the water/vapor interface (by the method of IHB and of ADH criteria). We carried on the longer time region 0.2 ps $< t <$ 12 ps. The unit for k (k') is ps^{-1}, and for τ_{HB} ($= 1/k$) is ps. The thickness d (Å) denotes the thickness of the interface, which is obtained from the instantaneous surface. The parameter values and units are the same below. 50
6.4 The k and k' for the interfacial hydrogen dynamics of the water/vapor interface (by the method of IHB and of AHD criteria). 50
6.5 The k and k' for the interfacial hydrogen dynamics of the water/vapor interface (by the method of molecule selection and of ADH criteria). . 50
6.6 The k and k' for the interfacial hydrogen dynamics of the water/vapor interface (by the method of molecule selection and of AHD criteria). . 50
6.7 The Dynamical properties of anion–water and water–water H-bonds at 300 K. Data are from DFTMD for the aqueous solutions. The values are expressed in ps. 53

B.1 The HB lengths r_a in $[NO_3{\cdot}(H_2O)_3]^-$ at 300 K. 61
B.2 The parameters of water molecules and HBs in $[NO_3{\cdot}(H_2O)_3]^-$ at 300 K. 61
B.3 The structural parameters of $RNO_3(H_2O)_3$ from geometry optimization. 61
B.5 The lengths of H-bonds in $[NO_3{\cdot}(H_2O)_3]^-$. The indices of H atoms: H6, H7 in w1; H9, H10 in w2 and H12, H13 in w3. 62
B.4 The parameters of $RNO_3(H_2O)_3$ at 300 K, obtained from the averaging during a DFTMD trajectory. For $RNO_3(H_2O)_3$, R_{OH} and R'_{OH} denote the lengths of O-H bonds in which H atoms is H-bonded and is free, respectively. 62

E.1 The k and k' for the bulk water. We carried on the short time region 0.2 ps $< t <$ 2 ps. The unit for k (k') is ps^{-1}, and that for τ_{HB} ($= 1/k$) is ps. The $h(t)$ is bond-based. 78

E.2 The k and k' for the bulk water. We carried on the long time region 2 ps $< t <$ 12 ps. The unit for k (k') is ps^{-1}, and that for τ_{HB} ($= 1/k$) is ps. The $h(t)$ is bond-based. 78

List of Abbreviations

ACF	**A**uto-**C**orrelation **F**unction
AIMD	*ab initio* **M**olecular **D**ynamics
BLYP	**B**eck-**L**ee-**Y**ang-**P**arr
BOMD	**B**orn-**O**ppenheimer **M**olecular **D**ynamics
CPMD	**C**ar-**P**arrinello **M**olecular **D**ynamics
DFT	**D**ensity **F**unctional **T**heory
DFTMD	**D**ensity **F**unctional **T**heory-based **M**olecular **D**ynamics
GGA	**G**eneralised **G**radient **A**pproximation
H-	**H**ydrogen
HB	**H**ydrogen **B**ond
HK	**H**ohenberg-**K**ohn
IHB	**I**nstantaneous interface **H**ydrogen **B**ond
KS	**K**ohn-**S**ham
LDA	**L**ocal **D**ensity **A**pproximation
MD	**M**olecular **D**ynamics
MP2	**M**oller-**P**lesset **P**erturbation
PBE	**P**erdew-**B**urke-**E**rnzherhof
PS	**P**hase-**S**ensitive
RDF	**R**adial **D**istribution **F**unction
SCF	**S**elf **C**onsistent **F**ield
VDOS	**V**ibrational **D**ensity **O**f **S**tates
VSFG	**V**ibrational **S**um-**F**requency **G**eneration
XC	e**X**change and **C**orrelation

Physical Constants

speed of light in vacuum	$c = 299\,792\,458\,\mathrm{m\,s^{-1}}$ (exact)
Boltzmann constant	$k_\mathrm{B} = 1.380\ 650\ 3(24)\times 10^{23}\ \mathrm{J\,K^{-1}}$
elementary charge	$e = 1.602\ 176\ 462(63)\times 10^{-19}\ \mathrm{C}$
electron mass	$m_\mathrm{e} = 9.109\ 381\ 88(72)\ \times 10^{-31}\ \mathrm{kg}$
proton mass	$m_\mathrm{p} = 1.672\ 621\ 58(13)\ \times 10^{-27}\ \mathrm{kg}$
Avogadro constant	$N_\mathrm{A} = 6.022\ 141\ 99(47)\ \times 10^{23}\ \mathrm{mol}$
Planck constant	$h = 6.626\ 068\ 76(52)\ \times 10^{-34}\ \mathrm{J\ s}$
molar gas constant	$R = 8.314\ 472(15)\ \mathrm{J\ mol^{-1}\ K^{-1}}$

List of Symbols

Z_{X}	atomic number of atom X
$\mathbf{R}$	atomic coordinates
τ_{a}	average lifetime of H-bonds: $\langle\tau_{\mathrm{a}}\rangle = \int_0^\infty tP_{\mathrm{a}}(t)dt$
κ_i	decay rate of $C_2(t)$
n_{X}	coordination number of ion X
δ_1	difference between the first peaks' positions of the RDFs g_{X-O} and g_{X-H}
$\mathbf{M}$	dipole moment
$\mu^{i,l,\epsilon}$	dipole moment of the bond ϵ of the i-th water molecule in the lab frame
A	dipole polarizability (tensor)
D	direction cosine matrix
r	distance
μ	electric dipole vector
$\mathbf{E}$	electric field strength
$n(\mathbf{r})$	electron density
H_{e}	electronic many-body Hamiltonian
$V(\mathbf{r})$	external potential
V_{ee}	electron-electron repulsion energy
$T[n]$	electronic kinetic energy
$E^{(2)}_{\mathrm{disp}}$	empirical two-body dispersion correction of energy
$E^{(3)}_{\mathrm{disp}}$	empirical three-body nonadditivity dispersion correction of energy
ΔF_{AB}	free energy difference between configuration A and B
F_A	free energy of configuration A
$L_{\eta\kappa}$	Fresnel coefficients
ω_{SFG}	frequency of the sum-frequency generation beam
ω_{vis}	frequency of the incident visible beam
ω_{IR}	frequency of the incident infrared beam
$h(t)$	HB population operator
$h^{(d)}(t)$	HB population operator (it is 1 if the tagged pair are closer than $r^{\mathrm{c}}_{\mathrm{OO}}$)
$H(t)$	HB population operator (continuously)
$C_{\mathrm{HB}}(t)$ (or $c(t)$)	HB population operator correlation function
ω_{I}	highest nuclear phonon frequency
θ	H-O-H angle in a water molecule
β	hyperpolarizability; reciprocal temperature
$h^s(t)$	interfacial HB population operator
$j(t)$	integrated flux departing the HB configuration space at time t
I_{SFG}	intensity of the sum-frequency generation beam
I_{vis}	intensity of the incident visible beam
I_{IR}	intensity of the incident infrared beam
r_{OO}	interoxygen distance
ω_{e}	the lowest electronic frequency
$r^{\mathrm{c}}_{\mathrm{OO}}$	the maximum value of the interoxygen distance (in the definition of HB)
ϕ^{c}	the maximum value of the angle between the O–O axis and one of the

	O–H bonds (in the definition of HB)
N	number of water molecules
R_{OH}	O-H length in water molecule
$C_2(t)$	orientational anisotropy decay
Z	partition function
α	polarizability tensor
$\alpha^{i,l,\epsilon}$	polarizability of the bond ϵ of the i-th water molecule in the lab frame
$P_a(t)$	probability distribution of the first HB breaking in time t
$C_z(t)$	projected velocity auto-correlation function along z-axis
$x^{\mathrm{l}}, y^{\mathrm{l}}, z^{\mathrm{l}}$	position coordinates in the lab frame
$x^{\mathrm{m}}, y^{\mathrm{m}}, z^{\mathrm{m}}$	position coordinates in the molecular frame
$x^{\mathrm{b}}, y^{\mathrm{b}}, z^{\mathrm{b}}$	position coordinates in the bond frame
$g_z(\nu)$	projected VDOS for selected atoms along z-axis
$g_{\mathrm{A–B}}$	radial distribution function
k	rate constant of breaking a HB
k'	rate constant of reforming a HB
θ_{SFG}	reflected angle of SFG beam w.r.t. the normal direction in the medium
$k(t)$	reactive flux
τ_{R}	relaxation time of HB population operator correlation function
$P_2(x)$	the second Legendre polynomial
$\chi^{(2),\mathrm{R}}$	second-order resonant susceptibility
$\chi^{(2),\mathrm{NR}}$	second-order nonresonant susceptibility
E_{KSDFT}	self consistent KS energy
$\Delta\nu'$	shift of vibrational frequency
$K_{\mathrm{p,X}}$	surface/bulk molar concentration ratio of ion X
$S_{\mathrm{HB}}(t)$ (or $s(t)$)	survival probability of HB
t_t	temporal resolutions for calculating HB dynamics
d	thickness of layer of interface (model)
τ	time for switching allegiance of a HB
$\hat{\mu}(t)$	unit vector of the transition dipole
$g(\nu)$	VDOS for selected atoms
$\mathbf{v}$	velocity of an atom
$C(t)$	velocity auto-correlation function
ν	vibrational frequency

To my family.

Chapter 1

Introduction

Interfaces of water and electrolyte solutions exist in many biological and industrial chemical systems, and are essential for all kinds of physical [1–3] and chemical processes. [4–6] Many phenomena in biology and chemistry, such as adsorption, bubble formation, occur at aqueous interfaces. [7] Particularly, water/vapor interfaces are the most common liquid interface. [8] Water/vapor interfaces of aqueous solutions play a important role in environmental chemistry, biological systems, [9, 10] man-made systems [11–13] and atmospheric science. [14, 15] Ions at the water/vapor interface can undergo heterogeneous or interfacial reactions. [16–20] Therefore, the distribution of ions at water/vapor interfaces is essential for understanding the structure and dynamics of interfaces. The hydrogen (H-) bonding network [**Poole1992**, **Soper2008**, 21–25] as well as electrostatic force, and van der Waals force are the main factors that determine the structure of interfaces. Salts change the H-bonding structure of water in the interfacial region. [7, 26, 27] The difference between anions' distribution may have significant influence on the H-bonding network of interfacial water. [28]

Compared to bulk atoms or molecules, interfacial atomic or molecular layers generally have very different optical properties. Experimentally, in order to determine the structure of an interface, one can use Vibrational Sum-Frequency Generation (VSFG) spectroscopy. The VSFG spectroscopy utilizes a second-order nonlinear optical process and the resulting signal is very sensitive to surface ions and molecules of a submonolayer level. [28–32] This technique allows for detecting intramolecular vibrational modes, and molecular orientation by detecting polarization dependence of the VSFG signals. [33] Furthermore, the VSFG spectroscopy does not require ultrahigh-vacuum environment. [34] The advantage is its wide applicability to almost every interface as long as light can reach them. Therefore, the VSFG spectroscopy can be used to probe many types of interfaces, namely, liquid-liquid and solid-liquid interfaces. [11, 28, 35–40] With the electric dipole approximation, the VSFG process is forbidden in any centrosymmetric bulk medium, [41] such as isotropic liquids and glasses, but it is allowed at interfaces because of the broken inversion symmetry at the interfaces. [42] The VSFG spectroscopy can also be applied to metal and semiconductor surfaces. [43, 44] The VSFG spectra suggest that the interfacial H-bonding between water molecules is changed by the presence of salt, especially the anions. [26] Molecular-level properties of interfacial materials arising from interactions between water and minerals, such as swelling, wetting, hydrodynamics can also be studied by the VSFG spectroscopy. [45]

However, the quantitative interpretation of the VSFG spectra is not straightforward, because the VSFG intensity is influenced by several factors, including ions' concentration, molecular orientation and distribution and local field correction. [28]

Although there is some general consensus on the fact that anions propensity inversely correlates with the order of the Hofmeister series, namely $CO_3^{2-} > SO_4^{2-} > F^- > Cl^- > Br^- > NO_3^- > I^- > ClO_4^- > SCN^-$, [46–49] the driving force and the microscopic details of the solvation structure are still debated. In terms of the Gibbs adsorption equation, the traditional theory predicts that no atomic ions will exist at interfacial regions of solutions. However, Molecular Dynamics (MD) simulations have shown that more polarizable anions (e.g., larger halide anions) are present in the surface region. [50, 51] Tian and coworkers [52] also have predicted that some ions, such as I^- and Br^-, could accumulate at the interface. The surface tension has been used to infer the composition of water/vapor interface, since the surface tension of the water/vapor interface is generally altered by dissolved substance. [51]

Recently considerable attention has been given to the nitrate ions in aqueous phase for their ubiquitous and diverse role in atmospheric aerosols, polluted water, and the remote troposphere. [53, 54] In order to clarify the variations of the structural and dynamical properties of water containing ions with high surface propensity, MD simulations are a valuable tool, which can provide detailed information on the structure and dynamics of water in a simple and well-known system like alkali metal nitrate and alkali metal halide solutions. [55] In recent years, MD simulations have been used for calculating properties, such as the depth profile of ion concentrations of interfaces, [50, 51] and the VSFG spectra of electrolyte solution surfaces, [31, 39, 56, 57] but the results depend heavily on the molecular model and interaction potentials used. [58–61] In this thesis, we use Density Functional Theory-based Molecular Dynamics (DFTMD) simulations to compute the interfacial VSFG spectra of eletrolyte solutions and to provide their molecular interpretation. The advantageof DFTMD is that it does not require a priori parameterization and it is capable to include polarization effects, [62] also including electronic polarization. DFTMD at the gradient corrected level, and also including dispersion corrections [63–67] has been shown to provide an accurate description of the vibrational properties at interface. [68]

The thesis is organized as follows. In chapter 2, we present the methods of *ab initio* Molecular Dynamics and one of its implementations— the DFT, the calculation of the Vibrational Density of States (VDOS), and the method to calculate the VSFG spectra. In chapter 3, we showed the experimental VSFG spectra of salty interfaces. In chapter 4, we present the results of VDOS for water clusters including alkali metal nitrates, which are calculated for interpreting the vibrational characteristics of water molecules in a special water/vapor interface—the water clusters. The theoretical results of VSFG spectra of water/vapor interfaces of alkali metal nitrate solutions are included in chapter 5. Chapter 6 focuses on the Hydrogen Bond (HB) dynamics of water/vapor interfaces, and the rotational anisotropy decay of water at interfaces of alkaline iodine solutions. The conclusions are summarized in chapter 7.

Chapter 2

Methods

In this chapter, we describe the methods we use to study the structure and dynamics of water and aqueous solutions. We use DFTMD simulations to calculate the theoretical VSFG spectra. Our motivations for adopting DFTMD simulations are manifold. In general, by using DFTMD, (1) Structure and reactivity can be treated in a consistent way; (2) Efficient treatments of basis sets and long range interactions in the DFT do extend the simulation capabilities to thousands of atoms, i.e. it allows realistic models for interfaces; (3) They provide information on the structural organization of the solvent in the interfaces. In particular, the interface of the solution contains a large number of water molecules and a HB network composed of H-bonds between them. As Stillinger said, "Since hydrogen bonding is the most important interaction in liquid water and since these interactions are cooperative (that is, nonadditive), it is insufficient for the purposes of computer simulation to use the potential energy function for dimers alone."[69] Paragraph 2.1 to 2.3 will give an introduction to the basic ideas of AIMD and DFT as well as the BOMD we adopted. Paragraph 2.4 and 2.5 will introduce the analysis methods used in this paper, including the method of calculating VDOS from velocity autocorrelation and the method of calculating SFG spectrum from velocity correlation function.

2.1 Modeling Interfaces with *ab initio* Molecular Dynamics

Modern theoretical methodology, aided by the advent of high speed computing, has advanced to a level where the microscopic details of dynamical processes in condensed phases can be treated on a relatively routine basis. One common theoretical approaches for obtaining these microscopic details of the system is the MD method. In the MD simulations, the classical Newtonian equations of motion for a system are solved numerically starting from a prespecified initial state, and subject to a set of boundary conditions appropriate to the problem. The MD methodology allows both equilibrium thermodynamic and dynamical properties of a system at finite temperature to be computed, while simultaneously providing a view of the microscopic motion of individual atoms in the system. [70]

Despite the success of classical molecular dynamics simulations, they have some limitations. First, charges are treated as static parameters, therefore electronic polarization effects are not included. The so-called polarizable models, [71–73] in which charges and induced dipoles are allowed to fluctuate in a changing environment, have been proposed to overcome this problem. While they have considerable success, they also have serious limitations, including a lack of transferability and standardization. [74] Second, force fields assume a pre-specified connectivity among the atoms, therefore, they suffer from an inability to describe chemical bond-forming and -breaking.

This problem can be treated using techniques such as the empirical valence bond method [75] or other semi-empirical approaches. Unfortunately, these methods are also not transferable and, therefore, need to be reparametrized for each type of reaction and may end up biasing the reaction path in undesirable ways.

To overcome these limitations of force field based approaches, *ab initio* molecular dynamics (AIMD) simulation techniques [76–82] can be used. The AIMD combines finite temperature dynamics with forces obtained from electronic structure calculations performed 'on the fly' as the MD simulation proceeds. [81] Because the electronic structure is treated explicitly in the AIMD calculations, many-body forces, electronic polarization and bond-forming and -breaking events are described with the accuracy of the electronic structure representation. Moreover, the AIMD method can be easily extended to incorporate nuclear quantum effects via the Feynman path integral approach, [83, 84] leading to the *ab initio* path integral technique. [85–87]

The AIMD method have been used to study a wide variety of chemically interesting problems in areas such as chemical reactivity, H-bonds for the interfacial structure, pKa, and vibrational spectroscopy. AIMD applications include calculations of the structure and dynamics of water and other H-bonded liquids, proton transport in aqueous and condensed phase environments, structure, proton order/disorder and dynamical properties of ice, structure of liquid silicates and glasses, mechanisms of polymer knotting, Ziegler-Natta industrial catalysis and other surface catalytic processes. More recently, the AIMD methods have started to impact the biological sciences and have been applied in calculations of nuclear magnetic resonance chemical shifts in drug-enzyme complexes, structure of nucleic acids, exploration of the design of possible biomimetics and structure, dynamics and binding mechanisms in myoglobin. In many of these applications, new physical phenomena have been revealed, which could not have been uncovered using empirical models, often leading to new interpretations of experimental data and even suggesting new experiments to perform. [74]

To study the heterogenous environment at water interface, AIMD is particularly suitable for the following reasons: (1) AIMD is only relying on the atomic coordinates of the model system $\mathbf{R}$, and not on any adjustable parameter, i.e., the interatomic forces $\mathbf{F_I} = -\bigtriangledown_{\mathbf{R_I}} V(\mathbf{R})$, where $V(\mathbf{R})$ is the potential energy, [88] are determined using the first principle electronic structure methods on the fly; (2) New phenomena that are not foreseen before starting the simulation can simply happen if necessary. Therefore, AIMD is also a good predictive tool. However, as a drawback, the AIMD simulations are expensive and can nowadays be performed on size-limited system of 100–1000 atoms for up to a few hundred ps.

2.2 Density Functional Theory

In most currently performed AIMD simulations, the dynamics is performed within the so-called Born-Oppenheimer approximation. Since the mass of an electron is much smaller than that of any nuclei, there is a strong separation of timescales between the electronic and nuclear motion. We assume that the kinetic energy of nuclei is zero and their potential energy is constant in each moment of the dynamics. Therefore, the electrons can be treated independently at constant nuclear coordinates $\mathbf{R}$. Applying Born-Oppenheimer approximation, the potential energy $V(\mathbf{R})$ is written as

$$V(\mathbf{R}) = \langle \Psi_0 | H_\mathrm{e} | \Psi_0 \rangle + E_I(\mathbf{R}), \tag{2.1}$$

where $|\Psi_0\rangle$ is the ground state, and H_e is the electronic many-body Hamiltonian, which depends on the electronic coordinates but parametrically on the nuclear degrees of freedom.

After the Born-Oppenheimer approximation, a formidable task is to solve the electronic, non-relativistic, time independent many-body Schödinger equation

$$H_\mathrm{e}|\Psi_0\rangle = \epsilon_0(\mathbf{R})|\Psi_0\rangle, \tag{2.2}$$

where $E_I(\mathbf{R})$ is the energy of the nuclei. This is a high-dimensional eigenvalue problem, and it is still time consuming. One great solution to the electronic structure problem (to solve the electronic, non-relativistic, time independent many-body Schödinger equation) is the DFT. [89, 90]

DFT can be used to map the problem of a interacting electron gas onto that of a single particle in an effective non-local potential. [77] It provides a favorable compromise between computational cost and accuracy.

Hohenberg and Kohn (HK) proved that the total energy of a many-electron system is a unique functional of the electron density $n(\mathbf{r})$. The first HK theorem proves that there exists a one-to-one correspondence between the ground state electronic density $n_0(\mathbf{r})$ and an external potential $v(\mathbf{r})$, i.e., the electron density n determines all properties of a non-degenerate ground state of an atom or molecule (for a degenerate ground state the density n determines the energy). (If we want to solve variationally for the ground state energy of a system with $H = T+V_{ee}+\sum_{i=1}^{N} v(i)$) the HK theorem says that there exists a valid functional $Q[n]$ that delivers the sum of the electronic kinetic energy $T[n]$ and electron-electron repulsion energy $V_{ee}[n]$ of each trial electron density n. [91]

The electronic density $n(\mathbf{r})$ which depends on just 3 electronic degrees of freedom, become the central quantity in DFT in place of the complex $3N_\mathrm{e}$-dimensional many-body wave-function.

The second HK theorem states that the total energy in the electronic density space satisfies

$$E^{\mathrm{DFT}}[n_0] = \psi_0 H_\mathrm{e}\psi_0 \leq \psi' H_\mathrm{e}\psi' = E^{\mathrm{DFT}}[n'], \tag{2.3}$$

for which the equality holds iff $n_0 = n'$. (variational principle) One try to choose different n to optimize $E^{\mathrm{DFT}}[n]$, the quantum expectation value of $H_\mathrm{e}[n]$, thus to determine $E^{\mathrm{DFT}}[n_0]$, i.e.

$$E^{\mathrm{DFT}}[n_0] = \min_{\psi} \psi H_\mathrm{e}\psi = \min_{n} \psi[n]H_\mathrm{e}[n]\psi[n] = \min_{n} E^{\mathrm{DFT}}[n], \tag{2.4}$$

Eq. (2.2) can be solved by iteratively diagonalizing $H_\mathrm{e}[n]$ within a self consistent field (SCF) procedure.

Assuming atomic units and considering the physical relevant Coulomb interaction, the total Hamiltonian is

$$\begin{aligned} H_\mathrm{e} =& \frac{1}{2}\sum_{i=1}^{N_\mathrm{e}} \nabla_i^2 + \sum_{i<j}^{N_\mathrm{e}} \frac{1}{|\mathbf{r}_i - \mathbf{r}_j|} + \sum_{I,i}^{N,N_\mathrm{e}} \frac{Z_I}{|\mathbf{R}_I - \mathbf{r}_i|} \\ =& \hat{T} + \hat{U} + \hat{V}, \end{aligned} \tag{2.5}$$

where Z_I is the atomic number of atom I, $\hat{T}$ is the operator of kinetic energy of electrons, $\hat{U}$ is the electron-electron interaction and $\hat{V} = \sum_i v(\mathbf{r}_i)$ is the electron-nuclei operator.

In DFT, we obtain the ground state energy of a many-electron system as minimum of an energy functional

$$E^{\mathrm{DFT}}[n(\mathbf{r})] = T[n(\mathbf{r})] + U[n(\mathbf{r})] + V[n(\mathbf{r})]. \tag{2.6}$$

The next problem is how to provide an explicit form for the three terms appearing in Eq. (2.6). The solution is the Kohn-Sham approach to DFT. A reference system with the same electron density as the density for the full interacting system and without electron electron repulsion is introduced. For such reference system, the kinetic energy functional is

$$T_{\mathrm{s}}[n(\mathbf{r})] = -\frac{1}{2}\sum_{i=1}^{N_{\mathrm{e}}}\int d\mathbf{r}\psi_i^*(\mathbf{r}) \bigtriangledown^2 \psi_i(\mathbf{r}) = T_{\mathrm{s}}[\{\psi_i[n(\mathbf{r})]\}], \tag{2.7}$$

and the electronic density can be written as

$$n(\mathbf{r}) = \sum_{i=1}^{N_{\mathrm{occ}}} f_i\psi_i(\mathbf{r})\psi_i^*(\mathbf{r}), \tag{2.8}$$

in which N_{occ} is the number of occupied orbitals and f_i the occupation number of the ith state, so that

$$\sum_{i=1}^{N_{\mathrm{occ}}} f_i = N_{\mathrm{e}}, \tag{2.9}$$

and $\psi_i(\mathbf{r})$ is the wave-function of the i-th state.

The total energy functional of the Kohn-Sham (KS) system is

$$\begin{aligned} E^{\mathrm{KS}}[n(\mathbf{r})] =& E^{\mathrm{KS}}[\{\psi_i[n(\mathbf{r})]\}] \\ =& T_{\mathrm{s}}[\{\psi_i[n(\mathbf{r})]\}] + U_H[n(\mathbf{r})] + V[n(\mathbf{r})] + E_{\mathrm{XC}}[n(\mathbf{r})] \qquad (2.10) \\ =& -\frac{1}{2}\sum_{i=1}^{N} f_i \int d\mathbf{r}\psi_i^*(\mathbf{r}) \bigtriangledown^2 \psi_i(\mathbf{r}) + \frac{1}{2}\int d\mathbf{r}\int d\mathbf{r}'\frac{n(\mathbf{r})n(\mathbf{r}')}{\mathbf{r}-\mathbf{r}'} \\ &+ \int d\mathbf{r}v_{\mathrm{ext}}(\mathbf{r})n(\mathbf{r}) + E_{\mathrm{XC}}[n(\mathbf{r})], \qquad (2.11) \end{aligned}$$

where $E_{\mathrm{XC}}[n(\mathbf{r})] \equiv (T[n(\mathbf{r})] - T_{\mathrm{s}}[\{\psi_i[n(\mathbf{r})]\}]) + (U[n(\mathbf{r})] - U_H[n(\mathbf{r})])$ is the exchange and correlation (XC) energy functional and $v_{\mathrm{ext}} = \delta V[n(\mathbf{r})]/\delta n(\mathbf{r})$ is the external potential. The energy functional $E_{\mathrm{XC}}[n(\mathbf{r})]$ is the only unknown part of the total energy functional. This definition of XC energy functional shows that a significant of part E_{XC} is due to correlation effects of the kinetic energy, that is expressed explicitly only with the reduced 2-particle density matrix.

Directly minimizing Eq. (2.10) is not straightforward because $T_{\mathrm{s}}[\{\psi_i[n(\mathbf{r})]\}]$ is an explicit orbital functional. However, it is more appropriate to make $E_{\mathrm{KS}}[\{\psi_i[n(\mathbf{r})]\}]$ stationary by the following Euler-Lagrange equation. It is possible to use the variational principle to derive the corresponding Euler-Lagrange equation of the non-interacting system within the potential v_{ext}. The KS scheme permits to map the full interacting many-body problem, with the electron-electron interaction $\hat{U}$ onto an equivalent fictitious single-body problem, with an effective potential operator $\hat{V}_{\mathrm{KS}} = \hat{U}_s + \hat{V}_{\mathrm{H}} + \hat{V}_{\mathrm{XC}}$.

If we figure out a way to approximate the V_{XC} accurately, we will have a much less demanding set of equations to solve than those of the true system. [92] Using the variational principle is possible to derive the corresponding Euler-Lagrange equation of the reference system (non-interaction system) within the potential v. To determine the set of wave-functions ψ_i which minimize the KS energy functional , we can iteratively solve the equation

$$[T_{\mathrm{s}}[n(\mathbf{r})] + V_{\mathrm{H}}[n(\mathbf{r})] + V[n(\mathbf{r})] + E_{\mathrm{XC}}[n(\mathbf{r})]]\,\psi_i(\mathbf{r}) = \varepsilon_i\psi_i(\mathbf{r}), \tag{2.12}$$

where ε_i is the eigenvalue of each equation, V_{H} is the Hartree potential of the electrons:

$$V_{\mathrm{H}} = e^2 \int \frac{n(\mathbf{r})n(\mathbf{r}')}{|\mathbf{r}-\mathbf{r}'|} d\mathbf{r}', \tag{2.13}$$

and the exchange and correlation potential

$$V_{\mathrm{XC}} = \frac{\delta E_{\mathrm{XC}}[n(\mathbf{r})]}{\delta n(\mathbf{r})}. \tag{2.14}$$

Given the explicit form of the exchange and correlation functional E_{XC}, the exchange and correlation potential V_{XC} can be determined, and thus electron density $n(\mathbf{r})$. Thus the KS equation must be solved self-consistently.

The simplest density functional approximation is the Local Density Approximation (LDA). In LDA, the exchange and correlation energy of an electronic system is

$$E_{\mathrm{XC}}[n(\mathbf{r})] = \int \varepsilon_{\mathrm{XC}}(\mathbf{r})n(\mathbf{r})d\mathbf{r}, \tag{2.15}$$

and

$$\frac{\delta E_{\mathrm{XC}}[n(\mathbf{r})]}{\delta n(\mathbf{r})} = \frac{\partial n(\mathbf{r})\varepsilon_{\mathrm{XC}}(\mathbf{r})}{\partial n(\mathbf{r})}, \tag{2.16}$$

where

$$\varepsilon_{\mathrm{XC}}(\mathbf{r}) = \varepsilon_{\mathrm{XC}}^{\mathrm{hom}}[n(\mathbf{r})]. \tag{2.17}$$

The LDA is accurate for systems with slowly varying charge densities. It has a tendency to favor more homogeneous systems and over-binds solids and molecules. The dielectric and piezoelectric constant calculated from the LDA are approximately 10% over estimated. The limitations of the LDA suggest that care must be taken into its applications. For example, the independent particle picture breaks down in strongly correlated systems, where the LDA is very inaccurate. Furthermore, the LDA does not take into account variation of the electronic density and van der Waals interactions, [92] so it does not give a very accurate description of H-bonding. H-bonding is essential for a correct description of water and interfaces with water, therefore, a functional beyond the LDA is needed in the description of hydrogen-bonded systems, including water.

For any density that varies sufficiently slowly, an expansion of a functional f in gradients should have increasing accuracy:

$$f[n] = \int d^3r[an(\mathbf{r}) + bn(\mathbf{r})|\nabla n(\mathbf{r})|^2 + \cdots]. \tag{2.18}$$

But the gradient expansion of the exchange-correlation energy does not always improve results, sometimes it leads to divergences. Therefore, a more general approach which is called Generalised Gradient Approximation (GGA) is considered. An approach to improve the LDA is to include gradient corrections , in which E_{XC} is a functional of density and its gradient:

$$E_{\mathrm{XC}}^{\mathrm{GGA}}[n(\mathbf{r})] = \int \varepsilon_{\mathrm{XC}}(n(\mathbf{r}))n(F_{\mathrm{XC}}[n(\mathbf{r}), |\nabla n(\mathbf{r})|])d\mathbf{r}, \tag{2.19}$$

where $F_{\mathrm{XC}}[n(\mathbf{r})]$ is a correction chosen to satisfy conditions for E_{XC}. The XC energy depends locally on the gradient of the density ∇n as well as the density n. There are several forms of the GGAs.

The GGA is usually the best compromise between speed and accuracy in large systems. For solids, the most commonly used functional with the GGA is the one proposed by Perdew, Burke and Ernzherhof (PBE). [93] Another popular GGA functional is the BLYP functional. The electron densities of electric dipole and quadruple moments are not uniform in space. Physically, GGAs include information on the spatial variation in the electron densities, and thus they can create functionals with better flexibility to describe dipole and quadruple moments. Therefore, GGAs generally describe the dipole and quadruple moments of the monomer quite well. However, they somewhat overestimate polarizabilities, the predicted dipolar polarizability (also called dipole polarizability) being typically 10% too large.

Dispersion is a general term referring to weak, long-range correlations in electronic structure. It includes van der Waals interactions, which originates from the coupling of the electric field generated by fluctuations in the electronic density at position $\mathbf{r}$ in the system with the density at another point $\mathbf{r}'$. [94] These interactions are not well modelled by any mean-field level of theory, the *ab initio* wave-function theory such as second-order Moller-Plesset perturbation theory (MP2), or standard DFT functionals, eg. LDA, GGAs, etc. The mean-field theory does not include the electron correlation effect, MP2 theory usually overestimate the binding energies and underestimates intermolecular equilibrium distances, and all the gradient corrected DFT are unable to describe dispersion interactions,because they can not describe the long-range electron correlation. In the last two decades, a series of empirical corrections have been proposed which can improve the structural properties without more computational cost. [63–66, 95–97] Among such empirical approaches we choose the DFT-D3 correction which can be used in our application to interfaces with water. [66, 98]

In the DFT-D3 correction, also used in this thesis, the input parameters are cut-off radii and dispersion coefficients, and they can be calculated by KS-DFT methods using extended atomic orbital basis sets. The use of structure dependent dispersion coefficients, i.e., functional coordination number, to interpolate between dispersion coefficients of atoms in different chemical environments, increases the accuracy. Moreover, no atom connectivity information is required and all the properties are calculated only from Cartesian coordinates and atomic numbers. [66]

If the three-body nonadditivity terms are considered, as well as the pairwise terms, the total energy is given by

$$E_{\mathrm{DFT}} = E_{\text{KS-DFT}} + E^{(2)}_{\mathrm{disp}} + E^{(3)}_{\mathrm{disp}}, \tag{2.20}$$

where $E_{\text{KS-DFT}}$ is the usual self-consistent KS energy obtained from the chosen density functional, $E^{(2)}_{\mathrm{disp}}$ is the empirical two-body dispersion correction term and $E^{(3)}_{\mathrm{disp}}$ is the three-body nonadditivity term. $E^{(2)}_{\mathrm{disp}}$ is given by

$$E^{(2)}_{\mathrm{disp}} = \sum_{\mathrm{AB}} \sum_{n=6,8,10,\cdots} s_n \frac{C_n^{\mathrm{AB}}}{R_{\mathrm{AB}}^n} f_{\mathrm{dmp},n}(r_{\mathrm{AB}}), \tag{2.21}$$

where $\sum\limits_{\mathrm{AB}}$ denotes the sum over all atom pairs in the system, C_n^{AB} is the averaged n-order dispersion coefficients ($n = 6,8,10,\cdots$) for atom pair AB, r_{AB} is the internuclear distance of atom pair AB, and $f_{\mathrm{dmp},n}(r_{\mathrm{AB}})$ is the damping function used to avoid near-singularities for small distance R between nuclei. The damping function in Eq. (2.21) is given by

$$f_{\mathrm{dmp},n}(r_{\mathrm{AB}}) = \frac{1}{1+6(r_{\mathrm{AB}}/(s_{r,n}R_0^{\mathrm{AB}}))^{-\alpha_n}}, \tag{2.22}$$

where $s_{r,n}$ is the order-dependent scaling factor of the cutoff radii R_0^{AB}, which is the most important parameter that has to be adjusted for each density functional and α_n is a parameter which can be adjusted manually such that the dispersion correction is smaller than 1% of $\max(|E_{\mathrm{disp}}|)$ for typical covalent bond distances. In the Ref.[66] $s_{r,6}$ is optimized by a least-squares fitting procedure and $s_{r,8}$ is fixed to 1 for all density functionals.

The leading non-additive dispersion term for three atoms A, B and C is

$$E_{\mathrm{disp}}^{(3)} = \frac{C_9^{\mathrm{ABC}}(3\cos\theta_a\cos\theta_b\cos\theta_c + 1)}{(r_{\mathrm{AB}}r_{\mathrm{BC}}r_{\mathrm{CA}})^2}, \tag{2.23}$$

where θ_a, θ_b and θ_c are the internal angles of the ΔABC, and C_9^{ABC} is the triple-dipole constant defined by

$$C^{\mathrm{ABC}} = \frac{3}{\pi}\int_0^\infty \alpha^{\mathrm{A}}(i\omega)\alpha^{\mathrm{B}}(i\omega)\alpha^{\mathrm{C}}(i\omega), \tag{2.24}$$

which can be approximated by a geometric mean

$$C^{\mathrm{ABC}} \approx -\sqrt{C_6^{\mathrm{AB}}C_6^{\mathrm{AC}}C_6^{\mathrm{BC}}}, \tag{2.25}$$

since the total three-body contribution is typically 5–10% of $E_{\mathrm{disp}} = E_{\mathrm{disp}}^{(2)} + E_{\mathrm{disp}}^{(3)}$.

2.3 Born-Oppenheimer Molecular Dynamics

In computational material science, the most popular AIMD simulation methods are the Born-Oppenheimer Molecular Dynamics (BOMD) and Car-Parrinello Molecular Dynamics (CPMD) methods. In the BOMD, the potential energy $E[\{\psi_i\};\mathbf{R}]$ is minimized at each MD step with respect to $\{\psi_i(\mathbf{r})\}$ under the orthonormality condition

$$\langle\psi_i(\mathbf{r})|\psi_j(\mathbf{r})\rangle = \delta_{ij}. \tag{2.26}$$

Thus the Lagrangian density is

$$\begin{aligned} L_{\mathrm{BO}}(\{\psi_i\};\mathbf{R}_I) =& \frac{1}{2}\sum_{I=1}^{N} M_{\mathrm{I}}\dot{\mathbf{R}}_I^2 - \min_{\{\psi_i\}}E[\{\psi_i\};\mathbf{R}_I] \\ &+ \sum_{i,j}\Lambda_{ij}(\langle\psi_i|\psi_j\rangle - \delta_{ij}), \end{aligned} \tag{2.27}$$

in which Λ is the Hermitian Lagrangian multiplier matrix. By the Euler-Lagrange equations one obtains the equations of motion

$$\begin{aligned} M_I\ddot{\mathbf{R}}_I =& -\nabla_{R_I}\left[\min_{\{\psi_i\}} E[\{\psi_i\};\mathbf{R}_I]|_{\langle\psi_i|\psi_j\rangle=\delta_{ij}}\right] \\ =& -\frac{\partial E}{\partial \mathbf{R}_I}+\sum_{i,j}\Lambda_{ij}\frac{\partial}{\partial \mathbf{R}_I}\langle\psi_i|\psi_j\rangle \\ & -2\sum_i \frac{\partial\langle\psi_i|}{\partial \mathbf{R}_I}\left(\frac{\delta E}{\delta\langle\psi_i|}-\sum_j\Lambda_{ij}|\psi_j\rangle\right) \end{aligned} \tag{2.28}$$

The term $-\frac{\partial E}{\partial \mathbf{R}_\mathrm{I}}$ is the Hellmann-Feynman force, and the term $\sum_{i,j}\Lambda_{ij}\frac{\partial}{\partial \mathbf{R}_\mathrm{I}}\langle\psi_i|\psi_j\rangle$, i.e., the wave-function force F_WF, [99] is a constraint force due to the orthonormality constraint. The last term comes from the fact that there is always an implicit dependence on the atomic positions through the expansion coefficient $c_{ij}(\mathbf{r})$ that is defined by

$$\psi_i(\mathbf{r})=\sum_j c_{ij}(\mathbf{r})\phi_i(\mathbf{r}), \tag{2.29}$$

where the KS orbitals are assumed to be real.

The CPMD is an alternative method to the BOMD, which includes the electrons in a single state. [100] In the CPMD, a coupled electron-ion dynamics is performed. The CP Lagrangian is

$$\begin{aligned} L_\mathrm{CP}(\{\psi_i\};\mathbf{R},\dot{\mathbf{R}}) =& \frac{\mu}{2}\sum_i\langle\dot{\psi}_i|\dot{\psi}_i\rangle+\frac{1}{2}\sum_{I=1}^{N}M_\mathrm{I}\dot{\mathbf{R}}_\mathrm{I}^2-E[\{\psi_i\};\mathbf{R}] \\ &+\sum_{i,j}\Lambda_{ij}(\langle\psi_i|\psi_j\rangle-\delta_{ij}), \end{aligned} \tag{2.30}$$

where the electronic degrees of freedom carries a fictitious mass parameter μ, and are characterized by orbital velocities $\{\dot{\psi}_i\}$. Applying the Euler-Lagrangian equations leads the equations of motion:

$$\begin{aligned} M_\mathrm{I}\ddot{\mathbf{R}}_\mathrm{I} =& -\nabla_{R_\mathrm{I}}\left[E[\{\psi_i\};\mathbf{R}]|_{\langle\psi_i|\psi_j\rangle=\delta_{ij}}\right] \\ =& -\frac{\partial E}{\partial \mathbf{R}_\mathrm{I}}+\sum_{i,j}\Lambda_{ij}\frac{\partial}{\partial \mathbf{R}_\mathrm{I}}\langle\psi_i|\psi_j\rangle \end{aligned} \tag{2.31}$$

$$\begin{aligned} \mu\ddot{\psi}_i(\mathbf{r},t) =& -\frac{\partial\langle\psi_i|}{\partial \mathbf{R}_\mathrm{I}}\left(\frac{\delta E}{\delta\langle\psi_i|}+\sum_j\Lambda_{ij}|\psi_j\rangle\right) \\ =& -\hat{H}_\mathrm{e}\langle\psi_i|+\sum_j\Lambda_{ij}|\psi_j\rangle, \end{aligned} \tag{2.32}$$

where $-\delta E/\delta\psi_i$ are the electronic forces to propagate the electronic degrees of freedom in time within a fictitious Newtonian dynamics. No SCF cycle is required to quench the electrons to the Born-Oppenheimer surface and to force them to evolve adiabatically with respect to the nuclei.

To ensure the adiabatic energy-scale separation of the nuclear and the electronic degrees of freedom, i.e. to prevent energy transfer between them, the highest nuclear phonon frequency ω_I must be much smaller than the lowest electronic phonon frequency ω_e. The condition $\omega_\mathrm{I} \ll \omega_\mathrm{e}$ is ensured by a proper choice of the fictitious mass μ. The fictitious mass determines the computational accuracy.

Which method is to favor depends largely on the definition of accuracy, as well as on the particular application. In the applications in this thesis, we use the BOMD method, as implemented in CP2K package. [101, 102] In the BOMD (1) the nuclear positions are propagated in time followed Newton's equations of motion with the electronic ground state energy as the potential energy surface; (2) the time evolution of the atomic coordinates is performed with the velocity Verlet algorithm. [103]

Since there is no explicit electron dynamics, the maximum integration time step is simply given by the one intrinsic to nuclear motion, i.e., $\tau_e^{\mathrm{BO}} \approx \tau_{\mathrm{n}}$. In BOMD, the time step can be even larger if the nuclear dynamics becomes fairly slow. [104] But in order to resolve vibrations in molecular systems, the time step must be decreased to less than 1 fs in this thesis. [81]

2.4 Vibrational Density of States

In order to obtain information on the vibrational properties of a molecular systems, it is possible to use the velocities auto-correlation functions (ACFs), as calculated from the AIMD trajectories. The obtained Vibrational Density Of States (VDOS) can provide information on the local environments on the OH-stretching mode of water molecules. For a system comprised of N atoms, the velocity ACF $C(t)$ for a molecule is [60, 105, 106]

$$C(t) = \frac{\langle \sum_{i=1}^{N} \mathbf{v}_i(t) \cdot \mathbf{v}_i(0) \rangle}{\langle \sum_{i=1}^{N} \mathbf{v}_i(0) \cdot \mathbf{v}_i(0) \rangle}, \tag{2.33}$$

where $\langle \dots \rangle$ denotes the average over starting times, t is the time interval, and $\mathbf{v}_i$ denotes the velocity of the i-th atom. The VDOS $g(\nu)$ for selected atoms, which is a function of the vibrational frequency ν of atoms, is expressed in terms of the FT of the velocity ACF of the atoms. [107] In equilibrium, $C(-t) = C(t)$, and $g(\nu)$ is a real function, i.e.,

$$g(\nu) = \sqrt{\frac{2}{\pi}} \int_0^{\infty} \mathrm{d}t\cos(2\pi\nu t) C(t). \tag{2.34}$$

Single components of the velocities ACFs can be also calculated. For example in the case of an interface it may be of interest to look at z-component (where z is the direction perpendicular to the surface), we can calculate the Fourier transform $g_z(\nu)$ of the ACF of the vertical component of atomic velocity. $g_z(\nu)$ can be calculated by Eq. (2.34), if we replace $C(t)$ by

$$C_z(t) = \frac{\langle \sum_{i=1}^{N} v_{i,z}(t) v_{i,z}(0) \rangle}{\langle \sum_{i=1}^{N} \mathbf{v}_i(0) \cdot \mathbf{v}_i(0) \rangle}, \tag{2.35}$$

where $v_{i,z}$ is the vertical component of the velocity of the i-th atom. The VDOS $g_z(\nu)$ for water molecules is used to extract the O-H stretch along the vertical direction to the averaging water/vapor interface.

2.5 Calculation of VSFG Spectroscopy for Water/Vapor Interfaces

As we introduced in Chapter 1, the VSFG spectroscopy is a powerful tool for extracting structural and dynamical information on surfaces and interfaces. It can be applied to any interface as long as light can reach it, also including liquid/metal interfaces [108–112] and buried interfaces; [113, 114] It can probe liquid interface with molecular sensitivity. [115–117] Therefore, VSFG spectroscopy can yield structural information about water/vapor interfaces which could not be obtained with other techniques.

2.5.1 Nonlinear Susceptibility of Water Molecules at Water/Vapor Interfaces

Sum Frequency Generation The sum frequency generation is a coherent nonlinear optical process in which incident laser beams with frequency and wave vector $(\omega_1, \mathbf{k}_1)$ and $(\omega_2, \mathbf{k}_2)$ produce a signal with frequency and wave vector $(\omega_1+\omega_2, \mathbf{k}_1+\mathbf{k}_2$) (Fig. 2.1). In this process, the fields arise from the polarization induced over a macroscopically large volume superposition coherently. The VSFG signal intensity is proportional to the square of the resonant and non-resonant terms:

$$I_{\mathrm{SFG}}(\omega) \propto |\chi^{(2),\mathrm{R}}(\omega) + \chi^{(2),\mathrm{NR}}(\omega)|^2. \tag{2.36}$$

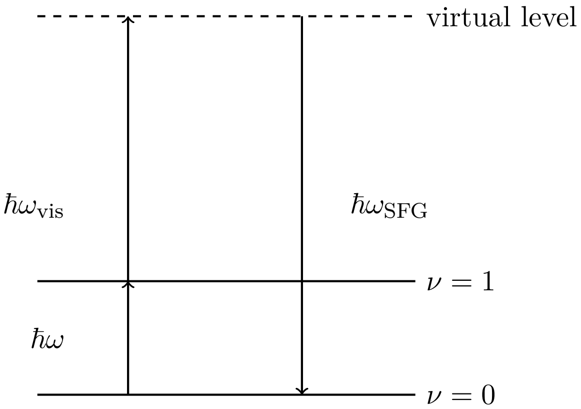

Figure 2.1: The schematic of the VSFG process which involves IR and Raman transitions. The $\nu = 0$, $\nu = 1$ levels denote the ground and the first excited state of the oscillator, respectively. The dashed line denotes a virtual electronic state in the Raman transition.

Because experiments usually employed visible and SFG frequencies are far from resonant conditions, $\chi^{(2),\mathrm{NR}}$ can be considered totally off-resonant and therefore insensitive to the laser beams' frequencies involved. Therefore, we can neglect the frequency dependence of the non-resonant term. The molecular information is contained in the resonant signal. The resonant susceptibility $\chi^{(2),\mathrm{R}}(\omega)$ is given by

$$\chi^{(2),\mathrm{R}}_{\eta\xi\kappa}(\omega) = \frac{-i}{\hbar}\int_0^\infty dt e^{i\omega t}\mathrm{Tr}[\rho, \mu_\kappa]\alpha_{\eta\xi}(t), \tag{2.37}$$

where the index η, ξ and κ are one of x, y and z labels of the laboratory coordinate frame. In Eq. (2.37) $\rho = e^{-\beta H/Z}$ for a system with Hamiltonian H and partition function Z at reciprocal temperature $\beta = 1/k_B T$; μ_κ is the κ-th component of the system electric dipole and $\alpha_{\eta\xi}$ is the $\eta\xi$-th component of the polarizabiltiy tensor. [118] Besides the vibrational resonance, $\chi^{(2),\mathrm{R}}$, which reflects the vibrational and orientational characteristics of the surface species, the VSFG signal also includes the contribution from the non-resonant signal background $\chi^{(2),\mathrm{NR}}$, due to static hyperpolarizability of the interface itself. [41] For example, there are strong non-resonant second-order nonlinear responses [112, 119, 120] of the interface in the case of some metal(-oxide). Generally, experiments employ visible light and VSFG frequencies far from resonant conditions, therefore, the non-resonant term $\chi^{(2),\mathrm{NR}}$ is approximately off-resonant to the light frequencies involved. [121]

Microscopic Expression of Molecular Hyperpolarizability As the electric field is increased, the description of the induced dipole moment $\boldsymbol{\mu}$ should include the normally insignificant nonlinear terms. We can express the induced dipole moment as

$$\boldsymbol{\mu} = \boldsymbol{\mu}_0 + \alpha \mathbf{E} + \beta \mathbf{E}\mathbf{E}. \tag{2.38}$$

The VSFG spectra are determined by the frequency-dependent hyperpolarizability in molecular level description. The frequency-dependent hyperpolarizability can be expressed as a sum of resonant and non-resonant terms:

$$\beta_{\eta\xi\kappa}(\omega_{\mathrm{SFG}}, \omega_{\mathrm{vis}}, \omega) = \beta^{\mathrm{R}}_{\eta\xi\kappa} + \beta^{\mathrm{NR}}_{\eta\xi\kappa}, \tag{2.39}$$

where η, ξ and κ are space-fixed axes. The resonant term of the frequency-dependent hyperpolarizability is

$$\beta^{\mathrm{R}}_{\eta\xi\kappa}(\omega_{\mathrm{SFG}}, \omega_{\mathrm{vis}}, \omega) = \sum_{v',v} \frac{\langle v|\alpha_{\eta\xi}|v'\rangle\langle v'|\mu_\kappa|v\rangle}{(\omega_{v'} - \omega_v) - \omega - i\gamma_{v'v}} \rho_v, \tag{2.40}$$

where the subscripts η, ξ and κ denote body-fixed axes, $\omega_{v'} - \omega_v$ is the vibrational energy gap, ρ_v is the thermal distribution function of the initial vibrational states v, $\alpha_{\eta\xi}$ is the $\eta\xi$-th component of the molecular dipole polarizability, μ_κ is the κ-th component of the molecular dipole moment, and $\gamma_{v'v}$ is the damping rate. Since (see Appendix A)

$$\int_0^\infty dt e^{-it((\omega_{v'}-\omega_v)-\omega-i\gamma_{v'v})} = \frac{-i}{(\omega_{v'} - \omega_v) - \omega - i\gamma_{v'v}}, \tag{2.41}$$

we can rewrite Eq. (2.40) as

$$\begin{aligned}
\beta^{\mathrm{R}}_{\eta\xi\kappa} &= i \int_0^\infty dt \sum_{v'v} e^{-i[(\omega_{v'}-\omega_v)-\omega-i\gamma_{v'v}]t} \langle v|\alpha_{\eta\xi}|v'\rangle\langle v'|\mu_\kappa|v\rangle\rho_v \\
&= i \int_0^\infty dt \sum_{v'v} e^{i\omega t} \langle v|e^{iHt}\alpha_{\eta\xi}e^{-iHt}|v'\rangle\langle v'|\mu_\kappa|v\rangle\rho_v \\
&= i \int_0^\infty dt e^{i\omega t} \langle \alpha_{\eta\xi}(t)\mu_{\eta\xi}(0)\rangle,
\end{aligned} \tag{2.42}$$

where H is the Hamiltonian of the system without external field. Eq. (2.42) indicates that the resonant term $\beta^{(2),\mathrm{R}}_{\eta\xi\kappa}$ is the Fourier-Laplace transformation of the quantity $\langle\alpha_{\eta\xi}(t)\mu_\kappa(0)\rangle$, i.e., the ensemble average of the time correlation function $\alpha(t)\mu_r(0)$. The damping rate $\gamma_{v'v}$ is not explicitly included in Eq. (2.42), because the dephasing is incorporated in the time development of the off-diagonal matrix elements of $\alpha_{\eta\xi}(t)$ and $\mu_\kappa(0)$.

The $\chi^{(2),R}_{\eta\xi\kappa}$ is microscopically represented as the average sum of first-order hyperpolarizability of the constituent molecules β in the space-fixed frame

$$\chi^{(2),R}_{\eta\xi\kappa} = \langle \sum_i^N \sum_{pqr} D_{\eta p}(\Omega_i) D_{\xi q}(\Omega_i) D_{\kappa r}(\Omega_i) \beta_{pqr} \rangle \tag{2.43}$$

where $D(\Omega_i)$ is the direction cosine matrix of the i-th molecule, projecting β onto the space-fixed frame. [122]

The Fresnel Factors Because of screening and dipole-dipole coupling, the local electric fields felt by molecules is different from the macroscopic fields. [120] The SFG signal depends on the magnitude of the local electric fields of the the interacting optical beams at the interfaces. While the magnitude of the local electric fields is related to both the intensity of the incident beams and the linear refractive indices of the different layers (bulk) of the sample. [115] The Fresnel coefficients define the magnitude of the electric fields at the interface. Therefore, to find out the magnitude of the local electric fields, we need to evaluate the Fresnel factors. The SFG intensity I_{SFG}, is proportional to the intensities of the incident visible and infrared beams, I_{vis}, I, and to the square of the second-order nonlinear susceptibilities, $\chi^{(2)}_{\eta\xi\kappa}(\omega_{\mathrm{SFG}})$, of the interface:

$$\chi^{(2)}_{\eta\xi\kappa}(\omega_{\mathrm{SFG}}) \propto |\sum_{\eta,\xi,\kappa} L_{\eta\eta}(\omega_{\mathrm{SFG}})\chi^{(2)}_{\eta\xi\kappa}(\omega_{\mathrm{SFG}})L_{\xi\xi}(\omega_{\mathrm{vis}})L_{\kappa\kappa}(\omega)|^2 \sec^2(\theta_{\mathrm{SFG}})I_{\mathrm{vis}}I \tag{2.44}$$

where η, ξ, κ are the Descartes coordinates of the reference frame; $\omega_{\mathrm{SFG}} = \omega_{\mathrm{vis}} + \omega$ is the frequency of SFG beam; $L_{\eta\eta}$, $L_{\xi\xi}$ and $L_{\kappa\kappa}$ are the Fresnel coefficients; θ_{SFG} is the reflected angle of SFG beam with respect to the normal direction in the medium.

2.5.2 Sum Frequency Generation Spectra from Velocity-Velocity Correlation Functions

In this paragraph I review the derivation an expression for the calculation of the sum frequency generation spectra of water interfaces that is based on the projection of the atomic velocities on the local normal modes, such an approach permits one to obtain the SFG signals from suitable velocity-velocity ACFs, reducing the computational cost to that of the accumulation of a molecular dynamics trajectory, and therefore cutting the overhead costs associated with the explicit calculation of the dipole and polarizability tensor. Moreover, the method permits to interpret the peaks in the spectrum in terms of local modes. The components of the resonant term $\chi^{(2),\mathrm{R}}_{\eta\xi\kappa}$ of the second order susceptibility can be calculated according to the classical formula [28, 121, 123]

$$\chi^{(2),\mathrm{R}}_{\eta\xi\kappa} = \frac{-i}{k_{\mathrm{B}}T\omega}\int_0^{\infty} dt e^{i\omega t}\left\langle \dot{A}_{\eta\xi}(t)\dot{M}_{\kappa}(0)\right\rangle \tag{2.45}$$

where k_{B} is the Boltzmann constant, ω is the frequency of the IR beam, $\mathbf{M}$ (A) are the dipole moment (dipole polarizability) of the system, and $\langle \dots \rangle$ denotes the average over all starting time points.

The total dipole moment and dipole polarizability derivatives for the system can be expressed in terms of the water and bond contributions:

$$\dot{A} = \sum_{i=1}^{N}\sum_{\epsilon}\dot{\alpha}^{i,\mathrm{l},\epsilon} \tag{2.46}$$

$$\dot{\mathbf{M}} = \sum_{i=1}^{N}\sum_{\epsilon}\dot{\mu}^{i,\mathrm{l},\epsilon} \tag{2.47}$$

where $\mu^{i,\mathrm{l},\epsilon}$ ($\alpha^{i,\mathrm{l},\epsilon}$) is the dipole moment (polarizability) of the bond ϵ of the i-th water molecule, the superscript (l) denote these quantities are measured in the lab frame, and N is the total number of the water molecules. Therefore, the correlation function in Eq. (2.45) can be written as

$$\begin{aligned}\langle \dot{A}_{\eta\xi}(t)\dot{M}_{\kappa}(0)\rangle &= \sum_{i=1}^{N}\sum_{\epsilon}\left\langle \dot{\alpha}^{\mathrm{l}}_{\eta\xi,i,\epsilon}(t)\dot{\mu}^{\mathrm{l}}_{\kappa,i,\epsilon}(0)\right\rangle \\ &+\sum_{i=1}^{N}\sum_{\epsilon}\left\langle \dot{\alpha}^{\mathrm{l}}_{\eta\xi,i,\epsilon}(t)\dot{\mu}^{\mathrm{l}}_{\kappa,i,-\epsilon}(0)\right\rangle \\ &+\sum_{i,j=1;i\neq j}^{N}\sum_{\epsilon,\epsilon'}\left\langle \dot{\alpha}^{\mathrm{l}}_{\eta\xi,i,\epsilon}(t)\dot{\mu}^{\mathrm{l}}_{\kappa,i,\epsilon'}(0)\right\rangle . \end{aligned} \tag{2.48}$$

In Eq. (2.48), the first term of the right-hand side is the bond auto-correlation, the second term accounts for the correlation between the two bonds in the same water molecule, and the third them for the correlation between bonds in two different water molecules.

We assume that the bond elongation are small compared to the total bond length and stretching frequencies of the bond are much larger than frequencies of bond reorientation, for example, the libration. Therefore, we can approximately write $\dot{\mu}(0)$ by

$$\begin{aligned}\dot{\mu}_{\kappa}(0) &= \sum_{i}^{x,y,z}\mathbf{D}_{\kappa i}(0)\dot{\mu}_{i}(0) \\ &= \sum_{i}^{x,y,z}\mathbf{D}_{\kappa i}(0)\left(\sum_{j}^{x,y,z}\frac{d\mu_i}{dr_j}\frac{dr_j}{dt}|_{t=0}\right) \\ &= \sum_{i}^{x,y,z}\mathbf{D}_{\kappa i}(0)\frac{d\mu_i}{dr_z}v_z(0), \end{aligned} \tag{2.49}$$

where $\mathbf{D}_{\kappa i}$ is the direction cosine between the laboratory-fixed κ axis and the molecular-fixed i axis, and $v_z = \frac{dr_z}{dt}|_{t=0}$ is the projection of the velocity on the bond axis.

Similarly, for the dipole polarizability, we have

$$\dot{\alpha}_{\eta\xi}(t) = \sum_{i,j}^{x,y,z}\left(\mathbf{D}_{\eta i}(t)\frac{\partial\alpha_{ij}}{\partial r_z}\mathbf{D}_{\xi j}(t)\right)v_z(t). \tag{2.50}$$

The Eq. (2.49) and Eq. (2.50) simplify the calculation of the $\left\langle \dot{A}_{\eta\xi}(t)\dot{\mathbf{M}}_{\kappa}(0)\right\rangle$ in Eq. (2.45), because $v_z(t)$ and $\mathbf{D}(t)$ can be readily determined from the DFTMD trajectory, and $\frac{d\mu_i}{dr_z}$ and $\frac{d\alpha_{ij}}{dr_z}$ can be parameterized. [115, 124]

We used three different frameworks: the lab framework $(x^{\mathrm{l}}, y^{\mathrm{l}}, z^{\mathrm{l}})$, the molecular framework $(x^{\mathrm{m}}, y^{\mathrm{m}}, z^{\mathrm{m}})$ and the bond framework $(x^{\mathrm{b}}, y^{\mathrm{b}}, z^{\mathrm{b}})$ (see Fig. 2.2). In the lab framework, the z^{l}-axis is perpendicular to the interface. The molecular frame will be used to decompose the signal into normal modes of water monomers. For the j-th molecule, the z^{m} axis is along the bisector of the H-O-H angle, the x^{m} axis is in the molecular plane, and the y^{m} axis is out of the molecular plane. [117]

In the bond framework, $z^{\mathrm{b},\epsilon}$ axis is along the bond ϵ of a molecule, $z^{\mathrm{b},\epsilon}$ is in the molecular plane and $y^{\mathrm{b},\epsilon}$ is out of the molecular plane.

$$\dot{\alpha}^{\mathrm{l},\epsilon} = \mathbf{D}^{\mathrm{m}}\mathbf{D}^{\mathrm{b},\epsilon}(\frac{\partial\alpha^{\mathrm{b}}}{\partial r}\dot{r}^{\epsilon})(\mathbf{D}^{\mathrm{b},\epsilon})^{\mathrm{T}}(\mathbf{D}^{\mathrm{m}})^{\mathrm{T}}, \tag{2.51}$$

$$\dot{\mu}^{\mathrm{l},\epsilon} = \mathbf{D}^{\mathrm{m}}\mathbf{D}^{\mathrm{b},\epsilon}(\frac{\partial\mu^{\mathrm{b}}}{\partial r}\dot{r}^{\epsilon}). \tag{2.52}$$

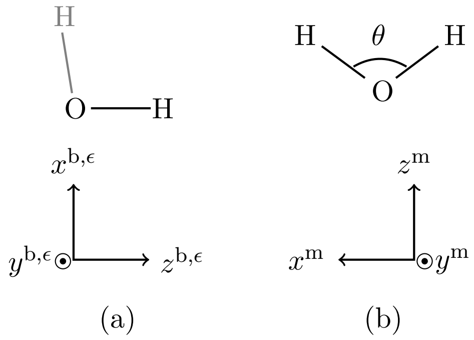
H
O
H
$x^{\mathrm{b},\epsilon}$
$y^{\mathrm{b},\epsilon}$
$z^{\mathrm{b},\epsilon}$
(a)
H
θ
H
O
z^{m}
x^{m}
y^{m}
(b)

FIGURE 2.2: The representation of the bond (a) and the molecular (b) frameworks. (from Ref. [117])

The direction cosine matrix $\mathbf{D}^{\mathrm{b},\epsilon=1}$ and $\mathbf{D}^{\mathrm{b},\epsilon=-1}$ can be expressed as

$$\mathbf{D}^{\mathrm{b},1} = \begin{pmatrix} \cos\frac{\theta}{2} & 0 & -\sin\frac{\theta}{2} \\ 0 & 1 & 0 \\ \sin\frac{\theta}{2} & 0 & \cos\frac{\theta}{2} \end{pmatrix}, \quad \mathbf{D}^{\mathrm{b},-1} = \begin{pmatrix} -\cos\frac{\theta}{2} & 0 & \sin\frac{\theta}{2} \\ 0 & 1 & 0 \\ \sin\frac{\theta}{2} & 0 & \cos\frac{\theta}{2} \end{pmatrix}, \tag{2.53}$$

where θ is the H-O-H angle in a water molecule. We can use $\mathbf{D}^{\mathrm{m}}$ to transform the coordinates in a molecular framework to coordinates in the lab framework. Because the orientation of water molecules is changing during the simulation, $\mathbf{D}^{\mathrm{m}}$ is time dependent.

The parametrization of $\frac{\partial \mu_k}{\partial r_z}$ and $\frac{\partial \alpha_{ij}}{\partial r_z}$ is based on the calculation of Maximally Localized Wannier Functions (MLWF) [125] and can be done through the approach developed by Salanne *et al.*[126] and Khatib *et al.*[117] The main advantage of such approximation for the calculation of the susceptibility is that still retain details of the water/vapor interfaces including the full electronic structure, but its computational cost is reduced with respect to a full calculation with the instantaneous evaluation of the molecular dipoles and polarizabilities. [127] The implementation of this parametrization is given in Appendix A.

Chapter 3

Experimental SFG spectra of salty interfaces

In this chapter, we will give the experimental results obtained on salty solutions containing alkali cations and nitrate (iodide) anions. [128–130]

From the experimental data of surface tension dependence on solute concentration $d\gamma/dm_2$ at low electrolyte concentrations ($\leq$1.5 M), [131–134] the relation of the surface/bulk molar concentration ratio K_p [135] among Li^+, Na^+ and K^+ is:

$$0 = K_{p,Na^+} < K_{p,K^+} < K_{p,Li^+}. \tag{3.1}$$

i.e., Na^+ is the most surface-excluded in the water solution RNO_3, K^+ is less excluded, and Li^+ is the least excluded cation. (See C.2 and C.3 for details.) In modeling the interfaces of aqueous sulitons of alkali metal nitrates, we decided to start with $LiNO_3$, because the Li^+ ion is the least excluded of the vapor-liquid interface among the alkali metal ions.

Hua *et al.*[130] have recently measured the VSFG spectra of water/vapor interface of $LiNO_3$ salt solutions in the OH stretching region (3000–3800 cm^{-1}) using Heterodyne Detected VSFG spectroscopy. [136–138] The experimental result of the VSFG intensity of the alkali nitrate interfaces is given by in Fig. 3.1. At a difference with the spectra for the water interface, in the spectra of $LiNO_3$ solutions, a depletion of the 3200 cm^{-1} peak is observed, with an enhancement of the 3400 cm^{-1} peak. A similar behaviour had been observed for the interface of $NaNO_3$ and $Mg(NO_3)_2$ solutions. [129, 130] It has been suggested that this depletion of the 3200 cm^{-1} peak, and in some cases the enhancement of the 3400 cm^{-1} peak, is an indication that nitrate ions reside at the interface. On the other hand the small cations should have little surface propensity. It has also been argued that the positive electric field found at the interface of NaCl, NaI and $NaNO_3$ salt solutions is due to the formation of an ionic double layer between anions located near the surface and their counter-cations (e.g. Na^+) located further below. In Phase-Sensitive (PS) VSFG experiments the magnitude of the induced change in the $\mathrm{Im}\chi^{(2)}$ spectra comparatively to that of the neat water suggested that NO_3^- has a surface propensity just in between I^- and Cl^-. [139, 140]

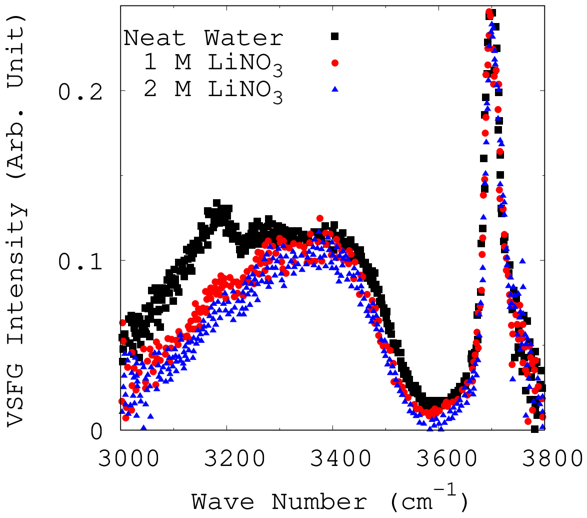

Figure 3.1: Experimental VSFG intensity of $LiNO_3$ solutions, compared with that of neat water. [130]

Chapter 4

Alkali Nitrate Clusters

In this chapter, gas phase clusters including alkali cations, nitrate ions and a few water molecules have been used to understand the effects of alkali cations and nitrate anions on hydrogen bonding. [141, 142] VDOS is used to extract the vibrational signatures for the water molecules in these systems. In the first two paragraphs the effect of the anion and the cation are separately investigated. The two clusters, $[NO_3{\cdot}(H_2O)_3]^-$ and $[Li{\cdot}(H_2O)_4]^-$, are used to study the structural and dynamical properties of water clusters with nitrate ions and with alkali cations at $T = 300$ K. In paragraph 4.3, the effects of the alkali metal cations and the nitrate anion are discussed within clusters containing both cations and anions and an increasing number of water molecules.

4.1 Cluster of Nitrate and Water Molecules

First, we consider the nitrate–water cluster, $[NO_3{\cdot}(H_2O)_3]^-$. The symmetric isomer of the cluster, as shown in Fig. 4.1(a), is obtained by geometry optimization at the BLYP/TZV2P level of theory. According to the definition of the H-bond, [143, 144] there are three H-bonds in it, i.e., only one of the two OH bonds is H-bonded to NO_3^- in each water molecule. Therefore, for each water molecule, we say there is one HB and one quasi-HB. Therefore, the two OH bonds in each water molecule exhibit different vibrational features. Fig. 4.2 shows the difference of VDOS for the OH bonds in the cluster. For each water molecule, one OH bond is vibrating in the frequency range 3680–3700 cm^{-1}, while the other in the frequency range 3380–3440 cm^{-1}. The difference of frequencies between the vibrational modes is about $\Delta\nu = 250$ cm^{-1}.

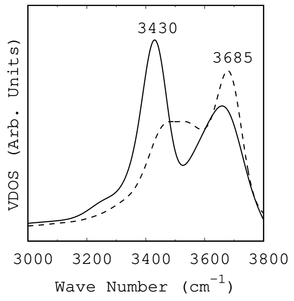

FIGURE 4.2: The VDOS for the two OH bonds in w1 (Fig. 4.1(a)) of $[NO_3{\cdot}(H_2O)_3]^-$.

Additionally, we label the three water molecules as w1, w2, and w3, respectively (Fig. 4.1(a)). For the three water molecules, we can find some difference in the structural parameters. Table B.5 gives the calculated lengths of H-bonds in the cluster $[NO_3{\cdot}(H_2O)_3]^-$. The average differences Δd between the H-bonds and the quasi-H-bonds are 0.69 Å (Table B.2).

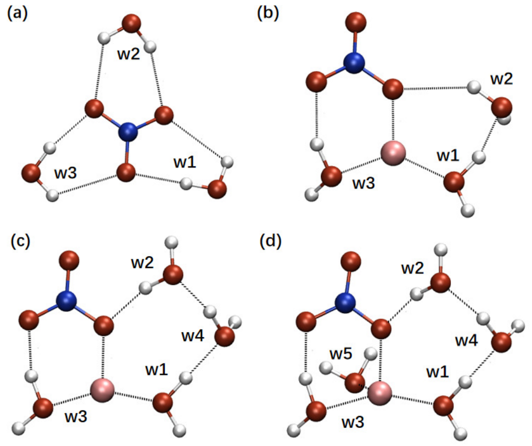

FIGURE 4.1: The geometry optimized structure of the clusters: (a) $[NO_3{\cdot}(H_2O)_3]^-$; (b) $RNO_3(H_2O)_3$; (c) $RNO_3(H_2O)_4$; (d) $RNO_3(H_2O)_5$ (R=Li,Na,K). More structural properties are shown in Appendix B.

4.2 Cluster of Alkali Metal Cation and Water Molecules

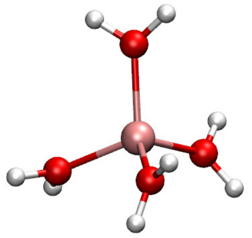

FIGURE 4.3: The cluster $[Li{\cdot}(H_2O)_4]^-$.

To find the effects of alkali cations on the structural properties of water, we investigate the cluster $Li^+(H_2O)_4$ (Fig. 4.3). We concentrate on two aspects: the radial distribution function (RDF), and the VDOS for water molecules of this cluster.

The sharp peaks in the RDF given in Fig. 4.4 show that the solvation shell of Li^+ is bound to all the four water molecules. The peak for g_{LiO} is at 2.02 Å, and for g_{LiH} is 2.69 Å.

The VDOS for water molecules in the cluster $[Li{\cdot}(H_2O)_4]^-$ is calculated from a 20-ps trajectory, during which one water molecule escaped from the bonding of the Li and then formed a new HB to another water molecule. First, Fig. 4.5 shows that, in this case, there are two types of OH stretching modes in the cluster $[Li{\cdot}(H_2O)_4]^-$: free OH stretch which peaks at 3705 cm^{-1} and bonded OH stretch at 3625 cm^{-1}. However, the water molecules just bound to Li has two degenerate free O-H stretching modes. The VDOS for water molecules only bound to Li (Fig. 4.6) shows that these water molecules only have free OH stretch, since there is only a broad stretching mode at 3705 cm^{-1}.

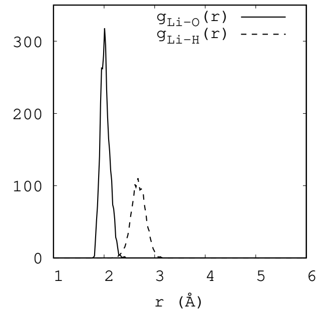

FIGURE 4.4: The RDFs $g_{\text{Li-O}}$ and $g_{\text{Li-H}}$ for the cluster $[Li{\cdot}(H_2O)_4]^-$.

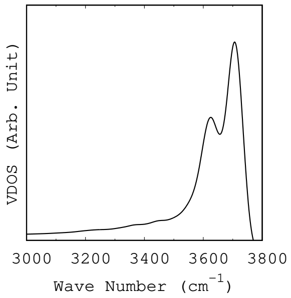

FIGURE 4.5: The VDOS for the four water molecules (all water molecules) in the cluster $[\mathrm{Li}\cdot(H_2O)_4]^-$.

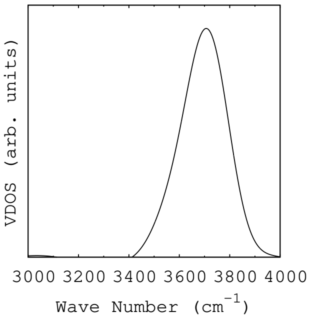

FIGURE 4.6: The VDOS for the water molecules bound to Li (three water molecules) in the cluster $[\mathrm{Li}\cdot(H_2O)_4]^-$.

4.3 Clusters of Alkali Nitrate and Water Molecules

As a first minimal model system for the interfaces of alkali nitrate solution, we consider alkali nitrate water clusters including 3 to 5 waters. The idea is to investigate the effect of the alkali nitrate on the vibrational properties of those water molecules which are directly H bonded to the ions. In our simulations, the clusters are geometry optimized and the most stable configurations are determined (Fig. 4.1(b)(c)(d)). The first interesting result is that for all the clusters containing 3 to 5 water molecules, a contact ion pair is maintained during the 300 K simulation trajectories where a direct interaction involves the cation and one of the nitrate oxygen's.

In the $LiNO_3(H_2O)_3$ cluster, there are three H-bonds and three Li-O bonds. The average lengths of them are given in Table 4.1. We use HB1, HB2 and HB3 to denote the HB between w1 and w2, w2 and NO_3^-, and w3 and NO_3^-, respectively (Fig. 4.1(b)). Both the average lengths of HB1 and HB3 are very close to each other and both of them are smaller than those of HB2. Since both w1 and w2 are bound to Li^+, we calculate an average value $\bar{d}_{\mathrm{HB}} = 1.81$ Å of the lengths of HB1 and HB3. The difference between length of HB2 and $\bar{d}_{\mathrm{HB}}$ is $\delta d_{\mathrm{HB}} = 0.19$ Å. By testing the difference of environment of each H-bonds, we obtain that δd_{HB} comes from the difference between Li-O and H-bonds. The RDF between the alkali (Li^+, Na^+ or K^+) and the water O (panel (a)) and the nitrate O – water H (panel (b)) are also reported in Fig. 4.7. The sharp peaks in the RDF (Fig. 4.7 (b)) show that the nitrate is solvated and in particular a stronger HB is formed in the presence of the cation. The vibrational features associated to the small clusters are calculated from the VDOS and reported in Fig. 4.9. In the frequency range 3000–3800 cm^{-1}, each water molecules has two vibrational bands. In addition to the free OH peak at 3700 cm^{-1}, we can

TABLE 4.1: The average length r_a of H-bonds (Li-O bonds) in the cluster $LiNO_3(H_2O)_3$.

Bonds	r_a(Å)
HB1	1.83 ± 0.14
HB2	2.00 ± 0.25
HB3	1.79 ± 0.16
O(w1)–Li	1.95 ± 0.09
O(w3)–Li	1.92 ± 0.07
nitrate O–Li	1.91 ± 0.08

see that the HB band is characterized by quite strong red-shifted peaks around 3200 cm^{-1}. These red-shifted peaks are associated to water molecules which are bound either to the cation or to both cation and anion and are different with respect to the peaks associated to the water molecules which only bound to the nitrate in the simple cluster $[NO_3{\cdot}(H_2O)_3]^-$ (3430 cm^{-1}, see e.g., in Fig. 4.2).

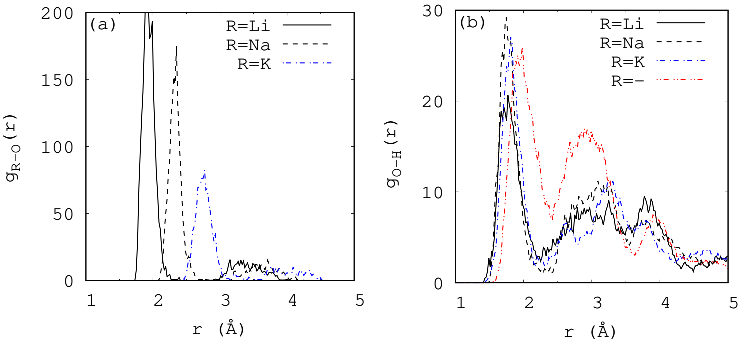

FIGURE 4.7: (a) The RDF $g_{\text{R-O}}$ for clusters $RNO_3(H_2O)_3$ (R=Li, Na, K); (b) The RDF $g_{\text{O-H}}$ for clusters $RNO_3(H_2O)_3$ and $[NO_3{\cdot}(H_2O)_3]^-$ (no alkali metal cation).

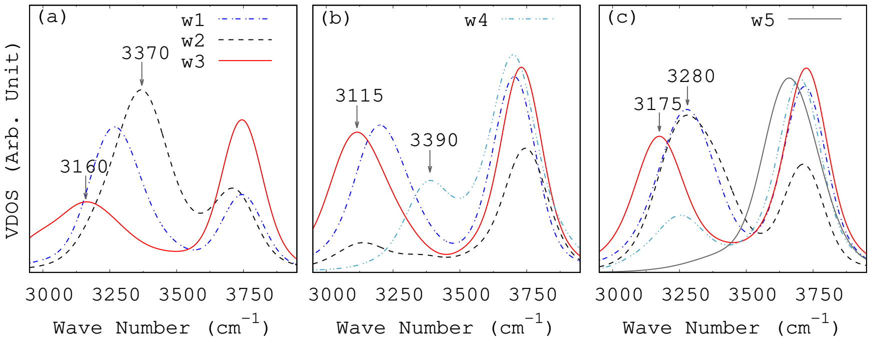

FIGURE 4.8: The VDOS for each water molecule in the cluster $LiNO_3(H_2O)_n$: (a) $n = 3$; (b) $n = 4$; (c) $n = 5$. w1: H_2O bound to Li and H_2O; w2: H_2O bound to nitrate and H_2O; w3: H_2O bound to Li and nitrate; w4: H_2O bound to H_2O; w5: H_2O only bound to Li.

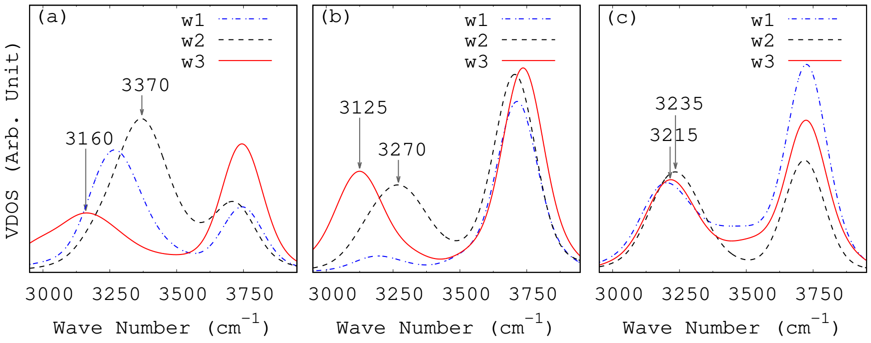

FIGURE 4.9: The VDOS for water molecules in clusters (a) $LiNO_3(H_2O)_3$, (b) $NaNO_3(H_2O)_3$ and (c) $KNO_3(H_2O)_3$. w1: H_2O bound to R and H_2O; w2: H_2O bound to nitrate and H_2O; w3: H_2O bound to R and nitrate.

To explore the effect of adding some additional water molecules to the cluster, we considered the clusters $RNO_3(H_2O)_n$ (n=4, 5; R=Li, Na, K). The most stable configurations are shown in Fig. 4.1(c) and (d), and the corresponding VDOS for the water molecules are shown in Fig. 4.8(b) and (c) for the clusters $LiNO_3(H_2O)_n$ (n=4 and 5). We find that the OH stretching peaks in the HB region are also quite red-shifted. The red shift is particularly strong for the water molecules which are directly interacting with the Li and those which are simultaneously bound to the Li and to the nitrate O's (e.g. w3).

We also calculate the effects of other alkali metal cations, namely Na^+ and K^+. The calculated VDOS for water molecules in clusters $NaNO_3(H_2O)_3$ and $KNO_3(H_2O)_3$ are shown in Fig. 4.9 (b) and (c), respectively. As in the case of $LiNO_3(H_2O)_3$, the HB bands are also characterized by red-shifted peaks around 3200 cm^{-1}. In addition, the peaks in the OH-stretching region are also compatible with infrared predissociation (IRPD) spectra which have been recorded for the $[Li{\cdot}(H_2O)_{3-4}Ar]^+$ clusters [145–147] and for $[Na{\cdot}(H_2O)_{4-7}]^+$ and $[K{\cdot}(H_2O)_{4-7}]^+$ clusters, [148] although there no nitrate is present and only the effect of the cation was investigated.

To summarize, the vibrational spectra from the clusters clearly point to red-shifted peaks which are not recorded in the vibrational sum-frequency generation spectra at the water/vapor interface for the $LiNO_3$ solution. In other words, these clusters are not really representative of the solvation structures presents in the $LiNO_3$ solution. Therefore, these small clusters cannot be directly used to describe the topmost layer of the $LiNO_3$ solution, and we need to build more realistic models to capture the main features the interface. In particular, according to the cluster picture one would be tempted to rule out the possibility of a contact ion pair at the interface.

Chapter 5

VSFG Spectroscopy of Water/Vapor Interfaces

In Chapter 4, we investigated the VDOS for water clusters containing nitrate ions and alkali metal ions. We find that the small clusters cannot be directly used to model the interfaces of aqueous solutions, and we need to build more realistic ones to capture the main features of interfaces. In this chapter, we will analyze the structure and dynamics of salty solutions containing an alkali cation and a nitrate (iodide) ion and to provide a microscopic interpretation of recent experimental results. [128–130]

The goal of this chapter is to find the origin of the main characteristics of the VSFG spectra of the $LiNO_3$ solution, and provide a molecular picture to interpret the recorded spectra. In order to achieve this goal, we simulate water/vapor interface including Li^+ and NO_3^-, as shown in Fig. 5.1, and extract the vibrational spectroscopic properties of the water/vapor interface of $LiNO_3$ solution.

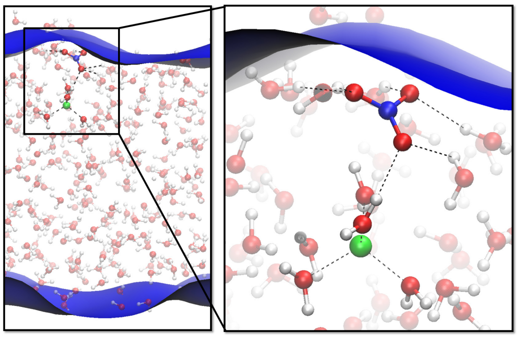

FIGURE 5.1: The water/vapor interfaces of $LiNO_3$ solution and pure water. The right panel shows that the Li^+ and the NO_3^- ions are separated by a water molecule at the salty interface.

We considered a model for water/vapor interface where a slab of 256 water molecules containing one Li^+ and one NO_3^- (denoted by $LiNO_3(H_2O)_{256}$) is included in a periodic simulation box of 19.70 × 19.70 × 40.00 $Å^3$ at 300 K. The slab is 20 Å thick and infinite in the x and y direction, while the separation between the periodic slabs in the z direction is 20 Å. The $LiNO_3$ was inserted at one of the two interfaces, with the NO_3^- residing in the topmost layer and the Li^+ residing somewhat deeper at about 5 Å from the surface. In this way we have a model with one *salty* interface and one neat interface which can be used as a reference. To provide the interpretation to the above experimental results, the following analysis tools are used: (1) VDOS; (2) calculation of the nonlinear susceptibility; (3) reconcile of the interface and cluster picture. In paragraph 5.1, the VSFG spectroscopy of the whole alkali nitrate interfaces of aqueous solutions is calculated, to find the connection between these two kind of models: the interface and cluster picture. Additionally, in order to study the effect of cations, the water/vapor interfaces of alkali-iodine solutions are also studied in paragraph 5.2.

5.1 VSFG Spectra of the Interface of $LiNO_3$ Aqueous Solutions

It has been often put forward the idea that in nitrate solution anion and cation are paired at the interface and form a double layer. Based on the relatively high propensity of NO_3^- for the interface [53, 149] we decided to start the simulations with the anion at the water surface and to investigate the possibility that $LiNO_3$ forms a stable water-separated ion pair at the interface. The idea that nitrate anions form water-separated pair where the Coulomb interaction is shielded was already suggested for divalent cation nitrate. [53] An equilibration time of about 10 ps was considered before the trajectory analysis, and subsequently 40 ps have been considered for production. The first result is that such model system is stable and the NO_3^- remains within the topmost water layer during all the simulation time. This result can be found in the probability distribution along z-axis of the simulation box, as shown in Fig. 5.2. This is in agreement with previous simulation results based on polarizable classical force field [150] and also with some DFTMD work on nitric acid, which was also found stable at the interface. [151] Moreover, the Li^+ remains relatively close to the surface, in a water sub-layer forming a water separated ion pair with the NO_3^- at the interface.

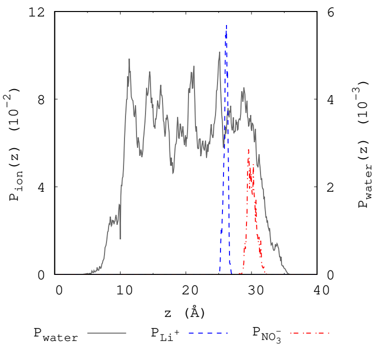

FIGURE 5.2: The probability distributions of ions and water molecules for $LiNO_3$ water interface along the normal direction, through the trajectory of 40 ps.

We have calculated the susceptibility for the two interfaces, namely the one containing the $LiNO_3$ pair(salty interface) and the neat one which does not include any ion. The calculated imaginary part is reported in panel (a) and the intensity in panel (b) of Fig. 5.3. The calculated intensity spectra show a depletion of the 3200 cm^{-1} region as in the experiments. The same feature is also shown in the imaginary part. Also the calculated spectra show that the free OH region is less intense in the salty interface with respect to the neat water interface.

To find the microscopic origin of the depression of the lower frequency region, we have also decomposed the salty water interface VDOS into the contributions coming from the different water molecules.

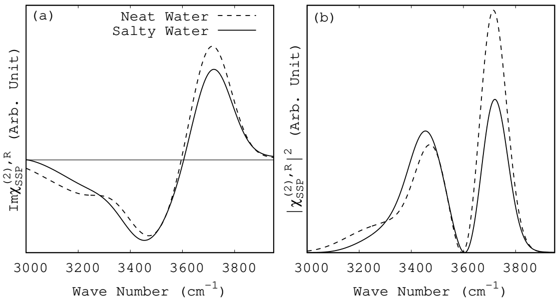

FIGURE 5.3: (a) The $\mathrm{Im}\chi^{(2),\mathrm{R}}_{SSP}$ and (b) the $|\chi^{(2),\mathrm{R}}_{SSP}|^2$ of water molecules at water/vapor interface of $LiNO_3$ solution. The simulation time: 40 ps; d=9 Å.

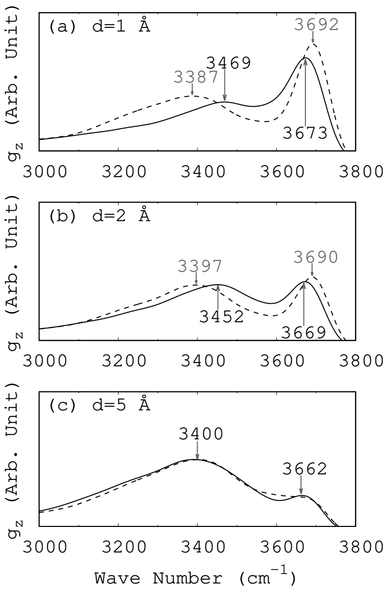

FIGURE 5.4: The VDOS $g_z(\nu)$ of water molecules in the water/vapor interface of $LiNO_3$ solution (solid line) and in vapor-pure water interface (dashed line). (a): $d = 1$ Å; (b): $d = 2$ Å; (c): $d = 5$ Å.

The VDOS $g_z(\nu)$ for the water molecules at the interface, which is calculated from the Fourier Transform (FT) of the auto-correlation function of velocity of the atoms in the z-axis projection, gives a rough value of the thickness of the interface d. Using 1, 2 and 5 Å thicknesses, we have defined three different interfacial regions. For the $LiNO_3$ solution, $g_z(\nu)$ of the salty and neat water interfaces in the slab is reported in Fig. 5.4. When d =1 Å, water molecules at the solution surface have lower free OH stretching frequency than that in pure water. This means that there are less water molecules with free OH stretch at the interface of $LiNO_3$ solution than at the interface of pure water. It compares very well with the experimental result of the surface propensity of nitrate anions in water solution. [128] Meanwhile, compared to the result of pure water, the H-bonded band of the VDOS for the salty interface has a blue shift of $\Delta\nu \approx 80$ cm^{-1}. As we increase the value of d, the difference between pure water and salt water VDOS is gradually reduced. For example, when $d = 2$ Å, the amount of blue shift $\Delta\nu$ is reduced to 55 cm^{-1}; when $d = 5$ Å, the amount of blue shift is almost zero. This indicates that the ions' (Li^+, Na^+, K^+ and NO_3^-) effects can be found only on the water molecules in the top ∼5-Å layer of the interface. As the thickness of the interfacial water layer included in $g_z(\nu)$ increases, the free OH signal is depressed and at the same time the H-bonded OH bands for the salty and neat water interfaces become more similar.

In order to explore the reason for the blue shift of the H-bonded OH stretch in the interface system, we also calculated the VDOS $g(\nu)$ for the 6 water molecules in the subsystems $NO_3^-(H_2O)_6$ (The structure of this cluster is shown in Fig. 5.1). Compared to the VDOS for H-bonded water molecules at the surface of pure liquid water, a blue shift of $\Delta\nu' \approx 80$ cm^{-1} on the vibrational modes of water molecules is found at the interface (Fig. 5.5). It indicates that a HB with nitrate acceptor is weaker than that with water acceptor. This feature agrees with experimental result obtained by Jubb et.al. [129] The OH stretching band at 3394 cm^{-1} (300 K) also agrees with that of liquid pure water (3400 cm^{-1}. [152]) Since the value of $\Delta\nu'$ is almost equal to the value of $\Delta\nu$ at $d = 1$ Å, we can conclude that the blue shift of the VDOS at the salty water interface is mainly caused by the H-bonds between the uppermost nitrate and water molecules at the salty interface.

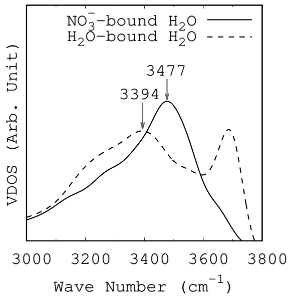

FIGURE 5.5: The VDOS for 6 water molecules bound to NO_3^- in vapor/$LiNO_3$ solution interface (salty water) and that for 15 water molecules at the top layer (d=1 Å) of the neat water.

First, there are two reasons to support the view that NO_3^- is located at the top layer of the surface. (1): The reduced intensity of the free OH peak can be explained by that NO_3^- is at the surface. The 3700 cm^{-1}-peak is the character of free OH stretch in water molecules with their dipole moment pointing to the vapor phase. [37, 153] NO_3^- binds to water molecules from the water surfaces which have less free OH, therefore reduce the intensity of the free OH peak. (2): Those water molecules directly H-bonded to the NO_3^- ion show an higher frequency band with respect to the neat water at the interface, which explain the increased intensity of the 3400 cm^{-1} band.

Second, the statement that Li^+ and NO_3^- are separated is confirmed by Ref. [154, 155], which show that the alkali metal cations are of *small* composite partition coefficients ($k_{p,K^+} = 0.00 \pm 0.03$, $k_{p,Na^+} = 0.05 \pm 0.17$, $k_{p,Li^+} = 0.14 \pm 0.18$), i.e., these cations are more surface-excluded than NO_3^- ($k_{p,NO_3^-} \approx 1.0$). How do we reconcile the interface picture and the cluster picture? In the small clusters (with 3, 4 and 5 water molecules) the contact ion pair is the most stable configuration, while at the interface the water separated configuration is the most stable. This suggests that a sufficiently large number of water molecules is required to stabilize a water separated ion pair where the NO_3^- anion still reside at the surface. To verify this idea we extracted a relatively large cluster with 30 water molecules from the full interface, centered around the Li^+ ion and we simulate it in the gas phase. For this medium size cluster we calculated the free energy difference between the water separated and the contact ion pair. The details of the calculation is given in Appendix C.1. The blue-moon ensemble method [156–158] is used to calculate the free energy as a function of a parameter: the distance r between alkali metal cation and the nitrogen of NO_3^- in $LiNO_3(H_2O)_{30}$. In Fig. 5.6, we find that there are two minima in the free energy at r = 2.9 Å (configuration A) and r = 4.3 Å (configuration B). Li^+ and NO_3^- are bonded in configuration A, but are water-separated in configuration B. The free energy difference $\Delta F_{AB} = F_A - F_B = 0.3$ kcal/mol. The energy barrier between C and A (B) is: $\Delta F_{CA} = 1.2$ kcal/mol ($\Delta F_{CB} = 1.5$ kcal/mol). Configuration B is more stable than A. For the water molecules in interface system, NO_3^- resides on the surface and Li^+ in the layer below, separated from NO_3^- by water molecules. Therefore, no obvious red-shift induced by alkali metal cation and nitrate is obtained in the VSFG spectrum. Our results show that as the number of waters increases, the first solvation shell around the Li^+ is stabilized and the water separated ion pair is equally stable as the contact ion.

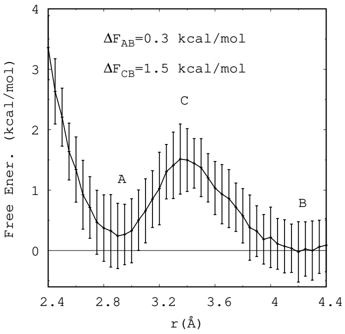

FIGURE 5.6: The free energy profile with respect to the distance r between Li^+ and the nitrogen in NO_3^- in the cluster $LiNO_3(H_2O)_{30}$. *A*: configuration A where r = 2.9 Å; *B*: configuration B where r = 4.3 Å; *C*: the transition states.

Finally, in the salty interface, one single water is constantly shared between the Li^+ and the NO_3^- and indeed this water shows a vibrational peak with a very pronounced red shift. This clearly reminds the water peak we already observed in the small clusters, however if the full interface is considered its signature do not emerge from the spectra, as it can be seen in Fig. 5.3.

From the three arguments above, our conclusion is thus that in the VSFG spectra we do only see the changes induced by the NO_3^- at the interface. This points to a clear 3400 cm^{-1} band in the vibrational spectra. The Li^+ resides in the sub-layer forming a water separated ion pair at the interface.

We have analyzed the behaviour of a salty water/vapor interface containing $LiNO_3$. Both the measured and calculated VSFG spectra show a reduced intensity of the lower frequency portion of the HB region, namely around 3200 cm^{-1}, when compared to the pure water/vapor interface. This reduction can be attributed to the H-bonds which are established between the NO_3^- and the surrounding water molecules at the interface. This effect is only related to the presence of NO_3^- at the water surface and is not affected by the presence of Li^+ ions. Indeed we have shown that although Li^+ can reside relative close to the water surface, also forming a water mediated ion pair with NO_3^-, its effect on the VSFG spectrum is not visible. The water which mediate the interaction between the NO_3^- and Li^+ would produce a red-shifted peak in small water cluster, but its influence is not visible neither in the calculated or the measured VSFG spectra. We have also shown that the very simple models, such as small clusters are not suitable to reproduce the experimental spectra and cannot provide a microscopic interpretation of the spectra. A realistic model of the interface is required to address the perturbation of the ion on the water surface.

5.2 VSFG Spectra of the Interface of Alkali Iodine Aqueous Solutions

Direct investigations of the dynamics of simple ions, such as I^- and Br^-, at interfaces, by the x-ray photoelectron spectroscopy [159] and MD simulations [50, 51] have shown that these ions could accumulate at the interface. In order to provide a molecular interpretation of the recorded spectra we perform here *ab initio* molecular dynamics simulation of salty solutions containing alkali cations and iodine.

A model for water/vapor interface is built, in which a slab of 118 water molecules containing two Li^+ cations and two I^- anions is included in a period simulation box of $15.60 \times 15.60 \times 31.00$ Å^3 at 330 K. This model corresponds to a 0.9 M solution. The slab is about 20 Å thick and infinite in the x and y direction, while the separation between the periodic slabs in the z direction is about 20 Å. In the initial configuration, the LiI was inserted at one of the two interfaces, with the I^- residing in the topmost layer and the Li^+ residing somewhat deeper at about 5 Å from the surface. Using the same method, we also constructed interface models of NaI solution and KI solution for DFT simulations. In all the cases the systems were equilibrated for 30 ps and then a production time of 60 ps was considered for the analysis.

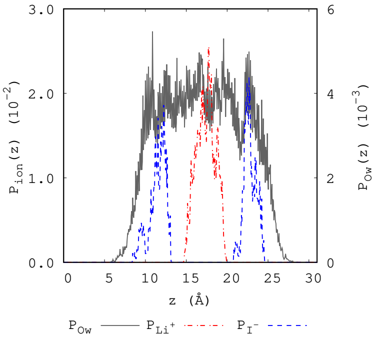

FIGURE 5.7: The probability distributions $P(z)$, along the normal direction, of Li^+, I^- and O in LiI solution-air interface, through the trajectory of 60 ps.

Structural Properties First, we have calculated the probability distributions of Li^+, I^- and O with respect to the normal direction of the LiI solution surface. The results are given by Fig. 5.7, where we see that I^- anions prefer to be located at the surface of the solution, while the Li^+ cations prefer to stay below the surface. This result is consistent with the calculations from Ishiyama and Morita [57, 60] on a similar system.

The effects of Li^+ and I^- on the organization of water molecules are shown in Li–water (Fig. 5.8(a)) and I–water RDFs (Fig. 5.8(b)), respectively. In Fig. 5.8, the first two peaks of $g_{\text{Li-Ow}}$ and $g_{\text{Li-Hw}}$ are located at 1.97 Å and 4.12 Å, and, 2.61 Å and 4.73 Å, respectively. Here we consider the *difference* δ_1 between the first peaks' positions of $g_{\text{X-O}}$ and $g_{\text{X-H}}$. Thus, one can determine the differences of the peaks' positions, which are shown in Table 5.1. The difference δ_1 between the first peaks, 0.67 Å, is shorter than the OH group length R_{OH} in a water molecule which is about 0.98 Å, i.e.,

$$\delta_1 < R_{\text{OH}}. \tag{5.1}$$

This relation reflects that all the water molecules around the Li^+ have their O atom facing Li^+. Similarly, we find from Fig. 5.8(b) that the distance δ_1 between the

TABLE 5.1: The peaks of $g_{\text{Li-O}}$ and $g_{\text{Li-H}}$ for 0.9 M LiI solution at 330 K. (unit:Å, the same below)

$g_{\text{Li-O}}$	$g_{\text{Li-H}}$	δ_1
1.97	2.64	0.67
4.12	4.73	0.61
6.13	6.93	0.80

TABLE 5.2: The peaks of $g_{\text{Na-O}}$ and $g_{\text{Na-H}}$ for 0.9 M NaI solution at 330 K.

$g_{\text{Na-O}}$	$g_{\text{Na-H}}$	δ_1
2.41	3.02	0.61
4.55	4.96	0.41
6.48	7.20	0.72

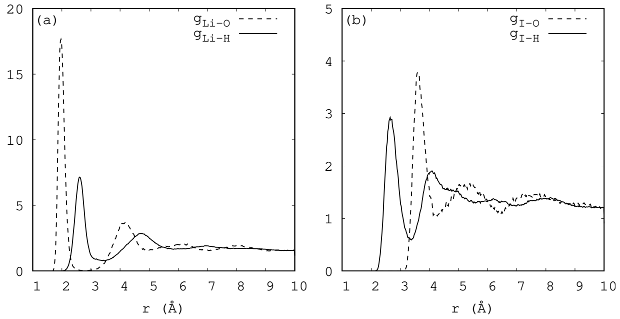

FIGURE 5.8: (a) The RDF $g_{\text{Li-O}}$ and $g_{\text{Li-H}}$ for LiI–water interface. The first two peaks of $g_{\text{Li-O}}$ and $g_{\text{Li-H}}$: 1.97 and 4.12 Å, and, 2.61 and 4.73 Å, respectively. (b)The RDF $g_{\text{I-O}}$ and $g_{\text{I-H}}$ for LiI-water interface. The first two peaks of $g_{\text{I-O}}$ and $g_{\text{I-H}}$: 3.62 and 5.28 Å; and, 2.69 and 4.11 Å, respectively.

first peaks of the two radial distribution functions is 0.93 Å, and it can be seen that δ_1 is slightly equal to R_{OH}, i.e.,

$$\delta_1 \approx R_{\text{OH}}. \tag{5.2}$$

This shows that for the water molecules around the I^-, only one H atom forms an I–H bond with the I^-. This also implies that I^- is essentially at the outermost layer of the solution interface. This is consistent with many of the previous results. [50, 51, 160–163]

For NaI and KI interfaces, the effects can be seen from Fig. 5.9 and 5.10. For Na^+ and K^+, the relation $\delta_1 < R_{\text{OH}}$ remains, i.e., $\delta_1 = 0.61$ Å for Na^+ and $\delta_1 = 0.56$ Å for K^+. For iodide ions, the relation $\delta_1 \approx R_{\text{OH}}$ still holds (See Fig. 5.9(a) and 5.10(a), and Table 5.2 and 5.3). For I^- in NaI interface, $\delta_1 = 0.96$ Å; and for I^- in KI interface, $\delta_1 = 0.94$ Å (See Fig. 5.9(b) and 5.10(b)). Therefore, these structural

TABLE 5.3: The peaks of $g_{\text{K-O}}$ and $g_{\text{K-H}}$ for 0.9 M KI solution at 330 K.

$g_{\text{K-O}}$	$g_{\text{K-H}}$	δ_1
2.84	3.40	0.56
4.71	5.51	0.80
6.78	7.49	0.71

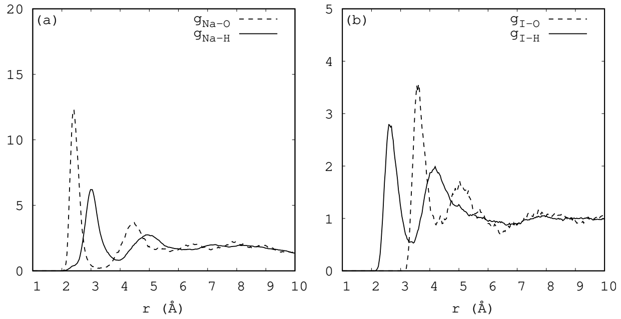

FIGURE 5.9: (a) The RDF $g_{\text{Na-O}}$ and $g_{\text{Na-H}}$ for NaI–water interface. The first two peaks of $g_{\text{Na-O}}$ and $g_{\text{Na-H}}$: 2.41 and 4.55 Å, and, 3.02 and 4.96 Å, respectively. (b)The RDF $g_{\text{I-O}}$ and $g_{\text{I-H}}$ for NaI-water interface. The first two peaks of $g_{\text{I-O}}$ and $g_{\text{I-H}}$: 3.59 and 5.04 Å; and, 2.63 and 4.15 Å, respectively.

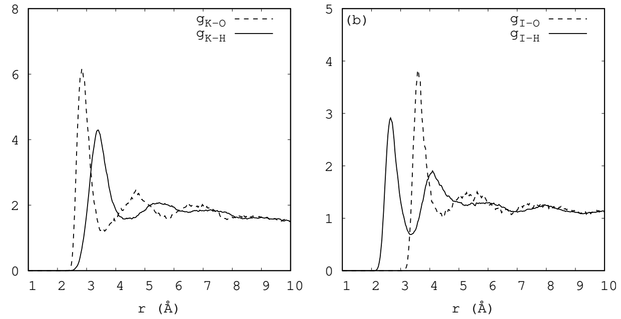

FIGURE 5.10: (a) The RDF $g_{\text{K-O}}$ and $g_{\text{K-H}}$ for KI–water interface. The first two peaks of $g_{\text{K-O}}$ and $g_{\text{K-H}}$: 2.84 and 4.71 Å, and, 3.40 and 5.51 Å, respectively. (b)The RDF $g_{\text{I-O}}$ and $g_{\text{I-H}}$ for KI-water interface. The first two peaks of $g_{\text{I-O}}$ and $g_{\text{I-H}}$: 3.59 and 5.43 Å; and, 2.65 and 4.10 Å, respectively.

properties are similar to that in LiI interface, except the larger solvation shells.

Vibrational Sum-Frequency Generation Spectra The SFG spectra for LiI, NaI and KI interfaces, as shown in Fig. 5.12, Fig. 5.11 and Fig. 5.13. In all the cases there is one free OH stretching band (3600–3800 cm^{-1}) and one bonded OH stretching band (3000–3600 cm^{-1}). For all the three cations the sign of Imχ is positive for the free OH peak while it is negative in the hydrogen bonded region. This result is consistent with the VSFG spectrum calculated in paragraph 5.1, i.e., (1) the anion–water H-bonds at water/vapor interfaces decrease the amount of free stretching OH bonds (2) the free stretching peak in the intensity of VSFG decrease and the H-bonded stretching peak is shifted at the interfaces of $LiNO_3$ (or alkali-iodine) solutions.

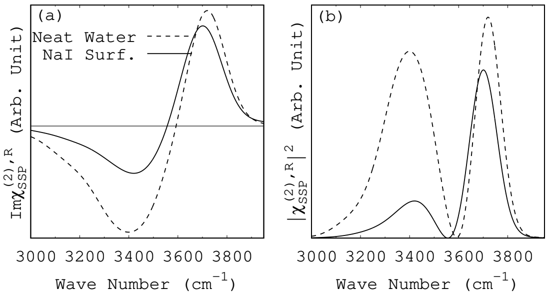

FIGURE 5.11: The (a) $\mathrm{Im}\chi^{(2),R}_{SSP}$ and (b) $|\chi^{(2),R}_{SSP}|^2$ of the water/vapor interface of 0.9 M NaI solution (solid line) and pure water/vapor (dashed line) interface. The data for pure water/vapor interface is calculated from the DFTMD simulation for the water interface with the same thickness (5 Å) at the same temperature (330 K). The same below.

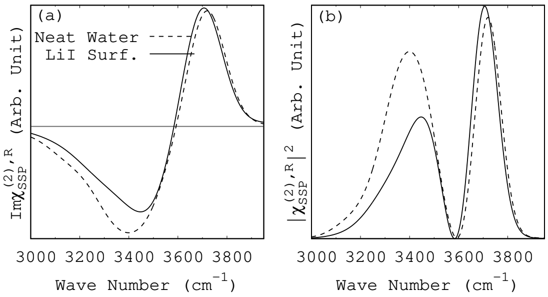

FIGURE 5.12: The (a) $\mathrm{Im}\chi^{(2),R}_{SSP}$ and (b) $|\chi^{(2),R}_{SSP}|^2$ of the water/vapor interface of 0.9 M LiI solution (solid line) and pure water/vapor interface (dashed line).

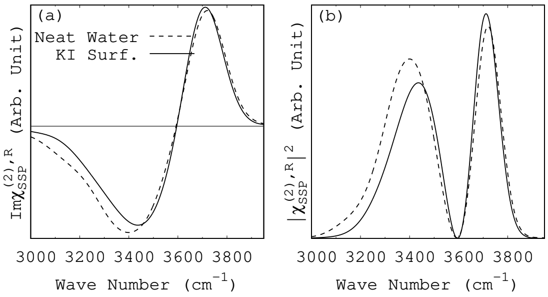

FIGURE 5.13: The (a) $\mathrm{Im}\chi^{(2),R}_{SSP}$ and (b) $|\chi^{(2),R}_{SSP}|^2$ of the water/vapor interface of 0.9 M KI solution (solid line) and pure water/vapor interface (dashed line).

Compared with pure water interface, the OH-bonded peak of NaI solution is blue-shifted, which is consistent with experimental results on NaI solutions. [26, 52, 129, 164] The H-bonded OH-stretching peak of LiI and KI solution are also blue-shifted. These results support the idea that I^- is a strong structure-breaking anion. Secondly, the bonded OH-stretching region of NaI solutions is narrower than that of pure water. This result has also been obtained for the interfaces of $LiNO_3$ solutions. The retained high frequencies of these bonded OH-stretching peaks indicate that these molecules at the interfaces of these solutions are participating in weak hydrogen bonding. The introduction of the I^- salts, caused a slight decrease in the strong H-bonding region at 3200 cm^{-1} and relatively an increase in the weak H-bonding region at 3400 cm^{-1}. This result is also consistent with experimental results in Ref. [129, 164].

Because of surface isotropy of the solutions, [165] the $\chi^{(2),\mathrm{R}}_{SSP}$ can be calculated either through $\chi^{(2),\mathrm{R}}_{XXZ}$, or $\chi^{(2),\mathrm{R}}_{YYZ}$. In our simulation, both of them give very similar results. Here we only report the comparison between $\mathrm{Im}\chi^{(2),\mathrm{R}}_{XXZ}$ and $\mathrm{Im}\chi^{(2),\mathrm{R}}_{YYZ}$ for 0.9 M KI solution in Fig. 5.14. It can be seen that indeed the spectra are very similar to each other. From the results of the nonlinear susceptibilities, we can conclude that these water molecules at the water/vapor interfaces of LiI, NaI, and KI solutions are participating in weaker hydrogen bond, compared with those at the pure water surface. The results of the simulations permits to interpret the features present in the experimental spectra, which can be explained as consequence of the double layer formed by the I$^-$ ions on the topmost water layer and the alkali in the sublayer (bulk in our relatively small simulation box).

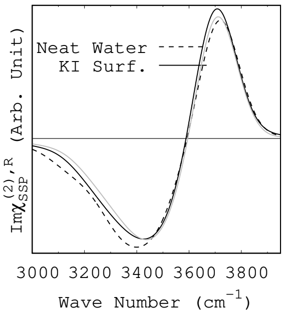

FIGURE 5.14: $\mathrm{Im}\chi^{(2),R}_{XXZ}$ (black solid) and $\mathrm{Im}\chi^{(2),R}_{YYZ}$ (grey solid) spectra are very close, because the interfaces have rotational symmetry about the z-axis.

Chapter 6

Hydrogen Bond Dynamics of Water/Vapor Interfaces

There are two types of bonds in water: the stronger covalent bonds (molecular σ bonds) within a single water molecule and the much weaker H-bonds between water molecules. H-bonds play a critical role in the behaviour of bulk water,[21, 166, 167] water near interfaces,[168] and aqueous solutions. [169] There are many methods to study the hydrogen bond (HB) dynamics in water, solutions or interfaces, such as molecular dynamics simulation,[168, 170–173] neutron scattering, Infrared (IR) spectroscopy,[174, 175] etc. In this chapter, we will introduce the general concepts and methods of HB Dynamics [166, 176, 177] used to analyze the structure and dynamic properties of bulk solutions and gas-liquid interfaces.

6.1 Definitions of Hydrogen Bond Population and Correlation Functions

Luzar and Chandler [176] have elucidated the HB dynamics of pure water, and subsequently such analysis has been also extended to explore the HB dynamics in complex situations, e.g., electrolytes, [178] protein and micellar surfaces. [179] There are temporal, geometric and energetic criteria to define HB. Here we use the geometric one. Two water molecules are H-bonded only if their interoxygen distance between of specific tagged pair of water molecules is less than $r_{\mathrm{OO}}^{\mathrm{c}}$ and the O-H$\cdots$O angle is less than ϕ^{c}. [143, 144, 180] The value $r_{\mathrm{OO}}^{\mathrm{c}}$ corresponds to the first-minimum position of the O–O RDF of water. [181] The choice for the cutoff angle ϕ^{c} for water-water molecules is obtained by studying the average number of H-bonds, as a function of ϕ^{c}. [182] We call this definition of HB the ADH criterion. In order to compare the impact of different HB definitions on HB dynamics, we will also use another definition of HB in our analysis. When the distance between the oxygen atoms of two water molecules is less than $r_{\mathrm{OO}}^{\mathrm{c}}$, and the oxygen-hydrogen-oxygen included angle is greater than a critical angle θ^{c}, then we say that there is a HB between the two molecules. We denote this definition as the AHD definition of H bonds.

The configuration criterion above allows us to define a variable $h[r(t)] = h(t)$, HB population. The $h(t)$ has a value 1 when the particular tagged pair of molecules are bonded, and 0 otherwise. We know that the instantaneous fluctuation or deviation in a dynamical variable $A(t)$ from its time-independent equilibrium average $\langle A \rangle$, is defined by [177]

$$\delta A = A(t) - \langle A \rangle.$$

For the $h(t)$, since the probability that a specific pair of molecules is bonded in a large system is extremely small, i.e., the time average of h is zero, or $\langle h \rangle = 0$, then

$$\delta h(t) = h(t).$$

Therefore, the $h(t)$ describe the instantaneous fluctuation $\delta h(t)$ of the HB population.

While the equilibrium average of the $\delta h(t)$ is zero, but we can obtain useful information by considering the equilibrium correlations between fluctuations at different times. The correlation between the $\delta h(t)$ and the $\delta h(0)$ can be written as

$$\langle \delta h(0) \delta h(t) \rangle = \langle h(0) h(t) \rangle - \langle h \rangle^2 = \langle h(0) h(t) \rangle,$$

where the averaging $\langle \cdots \rangle$ is to be performed over the ensemble of initial conditions (r^N, p^N).

In this paragraph, we will use three correlation functions to describe the HB dynamics of water/vapor interfaces of solutions, the HB population correlation function $C_{\mathrm{HB}}(t)$, the survival probability $S_{\mathrm{HB}}(t)$ and the reactive flux $k(t)$. [183]

Structure of HB Network One of the importrant characteristics of HB network is the average number of H-bonds per molecule. At room temperature and atmospheric pressure, this quantity is close to four or slightly higher. [184]

Furthermore, one can consider a more detailed distribution function. A molecule can form multiple H-bonds with other molecules at the same time. Among these H-bonds, the molecule has i times in the form of donors and j times in the form of acceptors, that is, the total number of H-bonds formed by the molecule at a certain time is $i + j$. Regarding the H-bonding of pure bulk water, people have obtained rich results with this analysis method and MD simulations. [184, 185]

HB Population Auto-Correlation Function We use the correlation function $C_{\mathrm{HB}}(t)$ to describe the structural relaxation of H-bonds:

$$C_{\mathrm{HB}}(t) = \langle h(0) h(t) \rangle / \langle h \rangle. \tag{6.1}$$

With the aid of the ergodic principle, the ensemble average $\langle \cdots \rangle$ is implemented by time average. The $\langle h \rangle$ is the probability that a pair of randomly chosen water molecules in the system is H-bonded in a certain form at any time t. Each water molecule has two H atoms and one O atom. Therefore, when a pair of water molecules a and b are bonded by a H-bond, the oxygen atom in each water molecule can act as both a donor and an acceptor. When water molecules a and b are used as donors, any one of its two H atoms can participate in the formation of H-bonds. Therefore, a pair of water molecules can form 4 different forms of H-bonds. In other words, if the role of H atoms between the pair of water molecules changes, but they still form H-bonds, we think that an old H-bond is broken and a new H-bond is formed. As examples, the dynamics of the interoxygen distance $r_{\mathrm{OO}}(t)$, the cosine of H$-$O$\cdots$O angle $\cos\phi(t)$ and the $h(t)$ for a HB in a water cluster is displayed in Fig. 6.1, respectively.

In a large system that consist of many water molecules, the probability that a specific pair of water molecules are H-bonded is extremely small. Therefore, the $C_{\mathrm{HB}}(t)$ also relaxes to zero, when t is large enough. The $C_{\mathrm{HB}}(t)$ measures correlation in $h(t)$ independent of any possible bond breaking events. This function is similar to one of the intermittent HB correlation functions, introduced by Rapaport,[183] and can be studied by a continuous function, probability densities. From the $C_{\mathrm{HB}}(t)$, the

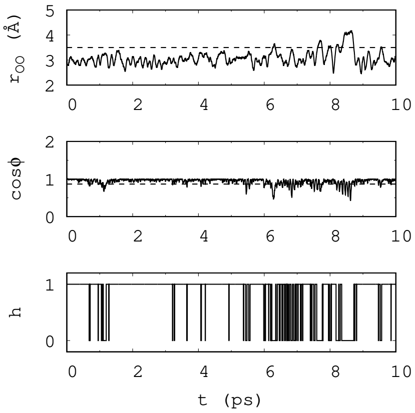

FIGURE 6.1: The dynamics of $r_{\mathrm{OO}}(t)$ (top), $\cos\phi(t)$ (middle), and $h(t)$ (bottom) for a HB in a water cluster. The dashed lines show the interoxygen distance boundary $r^{\mathrm{c}}_{\mathrm{OO}}$=3.5 Å (top) and criterion of cosine of H−O$\cdots$O angle $\cos\phi^{\mathrm{c}}$ with ϕ^{c}=30°, respectively.

HB relaxation time can also be computed.

$$\tau_{\mathrm{R}} = \frac{\int tC_{\mathrm{HB}}(t)\mathrm{d}t}{\int C_{\mathrm{HB}}(t)\mathrm{d}t}. \tag{6.2}$$

The $C_{\mathrm{HB}}(t)$ for the DFTMD simulated bulk water is shown in Fig. 6.2. Therefore, we can obtain the relaxation time from Eq. 6.2: $\tau_R = 14.01$ ps for ADH definition of H-bonds, and $\tau_R = 14.16$ ps for AHD definition where $r^{\mathrm{c}}_{\mathrm{OO}} = 3.5$ Å and $\theta^{\mathrm{c}} = 120°$ in the current thesis. Because the thermal motion can cause distortions of H-bonds from the perfectly tetrahedral configuration, water molecules show a librational motion on a time scale of $\sim$ 0.1 ps superimposed to rotational and diffusional motions ($>$ 1 ps), which causes a time variation of interaction parameters. A new HB population $h^{(d)}(t)$ was also defined to obviate the distortion of real HB dynamics due to the above geometric definition. [178, 181] The $h^{(d)}(t)$ is 1 when the interoxygen distance of a particular tagged pair of water molecules is less than $r^{\mathrm{c}}_{\mathrm{OO}} = 3.5$ Å at time t and 0 otherwise. The difference between the operators $h^{(d)}(t)$ and $h(t)$ is that those molecular pairs that meet the condition of $h^{(d)}(t) = 1$ may not meet the condition of $h(t) = 1$. That is, the H-bonds between the tagged molecular pairs that satisfy the condition $h^{(d)}(t) = 1$ may have been broken, but they may more easily form H-bonds

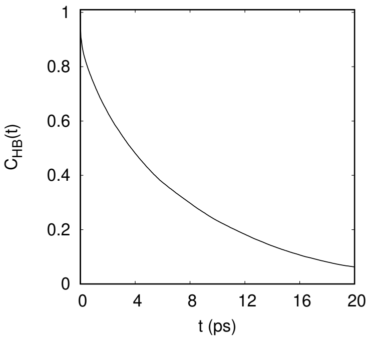

FIGURE 6.2: The time dependence of $C_{\mathrm{HB}}(t)$ ($c(t)$ for short)for the DFTMD simulated bulk water at 300 K with density $\rho = 1.00$ g/cm^3. Ref:[186]

again. The function

$$C_{\mathrm{HB}}^{(d)}(t) = \langle h(0)h^{(d)}(t)\rangle / \langle h\rangle \tag{6.3}$$

is the probability that the specific two water molecules are located in reformable region ($r_{\mathrm{OO}} < r_{\mathrm{OO}}^{\mathrm{c}}$) at time t, if they were H-bonded at time zero. The correlation function

$$n(t) = \langle h(0)[1 - h(t)]h^{(d)}(t)\rangle / \langle h\rangle \tag{6.4}$$

represents the probability at time t that a tagged pair of initially H-bonded water molecules are unbonded but remain separated by less than $r_{\mathrm{OO}}^{\mathrm{c}}$. In the above formula, $1 - h(t)$ describes the breaking of a HB at time t after its formation at time $t = 0$.

Survival Probability Another scheme to describe HB dynamics is the survival probability [178] for a newly generated HB. It is defined as

$$S_{\mathrm{HB}}(t) = \langle h(0)H(t)\rangle / \langle h\rangle, \tag{6.5}$$

where $H(t) = 1$ if the tagged pair of molecules, remains *continuously* H-bonded till time t and 0 otherwise. It describes the probability that an initially H-bonded molecular pair remains bonded at all times up to t. [187] The $S_{\mathrm{HB}}(t)$ for the DFTMD simulated bulk water is shown in Fig. 6.3.

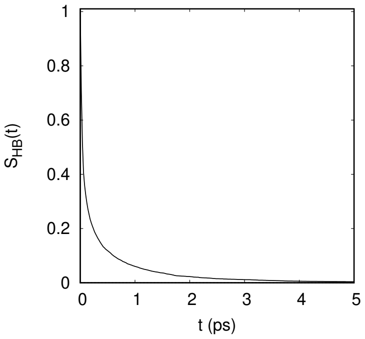

FIGURE 6.3: The time dependence of $S_{\mathrm{HB}}(t)$ (denoted by $s(t)$ for short) for the DFTMD simulated bulk water at 300 K with density $\rho = 1.00$ g/cm^3.

The average continuum HB lifetime $\langle\tau_{\mathrm{a}}\rangle$ is calculated by the integration of $S_{\mathrm{HB}}(t)$ over t (see Appendix E.1) :

$$\langle\tau_{\mathrm{a}}\rangle = \int_0^\infty dt S_{\mathrm{HB}}(t). \tag{6.6}$$

The time derivative of $S_{\mathrm{HB}}(t)$

$$P_a(t) = -\mathrm{d}S_{\mathrm{HB}}/\mathrm{d}t \tag{6.7}$$

represents the first passage time probability density of H bonds. $P_a(t)$ is also called probability distribution of HB lifetimes, [188–191] or histogram of HB lifetimes.[192, 193] It denotes the probability of the first HB breaking in time t after it has been detected at $t = 0$, i.e.,

$$S_{\mathrm{HB}}(t) = \int_t^\infty P_a(t')dt'. \tag{6.8}$$

Reactive Flux $k(t)$ Calculating the reactive flux HB correlation functions and determine the rate constant ($1/\tau_{\mathrm{HB}}$), is a more rigorous way to obtain the nature of H-bonds at water/vapor interfaces. [194] The rate of relaxation to equilibrium is characterized by the reactive flux correlation function,

$$k(t) = -\frac{\mathrm{d}C_{\mathrm{HB}}}{\mathrm{d}t}, \tag{6.9}$$

i.e., $\langle j(0)[1 - h(t)]\rangle/\langle h\rangle$, where $j(0) = -\mathrm{d}h/\mathrm{d}t|_{t=0}$ is the integrated flux departing the HB configuration space at time $t = 0$ (see Appendix E.1). The reactive flux $k(t)$ quantifies the rate that an initially present HB breaks at time t, independent of possible breaking and reforming events in the interval from 0 to t. Therefore, the $k(t)$ measures the effective decay rate of an initial set of H-bonds. [177, 195]

For bulk neat water, there exists a $\sim$ 0.2-ps transient period, during which the $k(t)$ quickly changes from its initial value. [195] However, at longer times, the $k(t)$ is independent of the HB definitions. In order to verify this point of view and also to verify the reliability of our simulation method, we performed a DFTMD simulation of the bulk water system with a total time of 60 ps, and used the two different HB definitions — ADH definition and AHD definition to calculate the $k(t)$. The calculation results in Fig. 6.5b show that when t is large enough, the difference in $k(t)$ caused by different HB definitions is relatively small. Therefore, the long time decay of the $k(t)$ reflects the general properties of H-bonds.

We assume that each HB acts independently of other H-bonds, [176, 194] and due to detailed balance condition, we can obtain

$$\tau_{\mathrm{HB}} = \frac{1 - \langle h\rangle}{k}, \tag{6.10}$$

where k is the rate constant of breaking a HB (forward rate constant). [196, 197] For an aqueous interface, the probability of exactly a tagged molecule pair forming a HB is very low, that is, $\langle h\rangle \ll 1$. Therefore, the k is related to the average HB lifetime by $\tau_{\mathrm{HB}} = 1/k$. We use k' to represent the backward rate constant, that is, the rate constant from the HB *on* state to the HB *off* state for a tagged pair of molecules. Therefore, the reaction time constant τ_{re} is

$$\tau_{\mathrm{re}} = \frac{1}{k + k'}. \tag{6.11}$$

Structural Properties of Pure Water The pure water system and the interface between pure water and vacuum, i.e., the water/vapor interface, are ideal model systems for testing our algorithms. For pure water systems, especially for bulk water, we can compare the results of the current method with the results of previous researchers.[176, 198] On this basis, we will show in the next paragraphs about the pure water interface, the aqueous solution containing ions, and the HB dynamics in the interface corresponding to the aqueous solution.

The oxygen-oxygen radial distribution functions $g_{\mathrm{OO}}(r)$ and $g_{\mathrm{OH}}(r)$ for the bulk water system are shown in Fig. 6.4a.

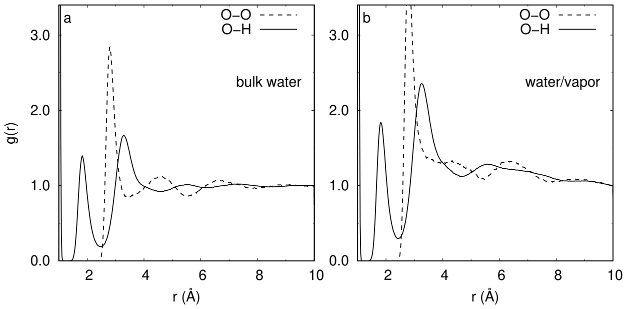

FIGURE 6.4: The partial RDFs of liquid water at ambient conditions. (a) Bulk water (box size: 15.64 × 15.64 × 15.64 Å^3; $T = 300$ K); (b) water/vapor interface (box size: 15.64 × 15.64 × 31.28 Å^3; $T = 300$ K).

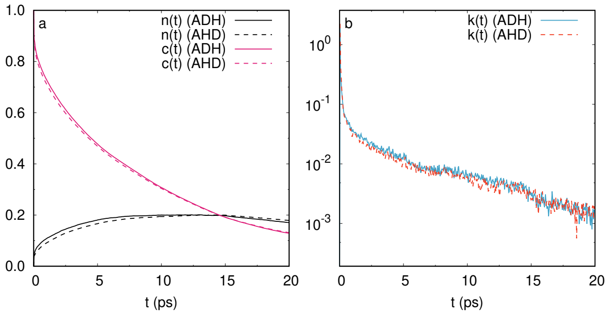

FIGURE 6.5: Time dependence of the correlation functions (a) $n(t)$, $c(t)$ and (b) the rate function $k(t)$ of water–water H-bonds for *bulk* water, calculated from the trajectory of a DFTMD simulation. The definition of $h(t)$ is based on specific H–O bond, instead of water-water pairs. The simulation was for bulk water at $T = 300$ K, and with a density of 1.00 g cm^{-3}. The length of the trajectory is 50 ps of physical time.

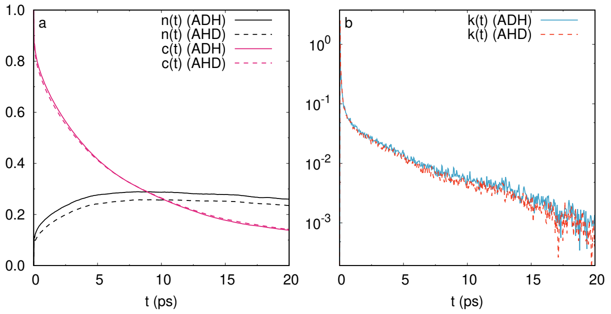

FIGURE 6.6: Time dependence of the correlation functions (a) $n(t)$, $c(t)$ and (b) the $k(t)$ of water–water H-bonds for water/vapor *interface* at 300 K, calculated from the trajectory of a DFTMD simulation. The definition of $h(t)$ is based on specific H–O bond, instead of water-water pairs. The length of the trajectory is 50 ps of physical time.

The correlation function $C_{\mathrm{HB}}(t)$ ($c(t)$ for short) from the trajectory of a DFTMD simulation with ADH (solid line) and AHD (dashed line) definition of H-bonds is shown in Fig. 6.5 (a). The length of the trajectory coincided with 60 ps of physical time. The simulation is for bulk water at the temperature 300 K and with a density 1.00 g/cm^3.

The reactive flux $k(t)$ we calculated here is very consistent with the result in [199].

For the water/vapor interface of neat water, we reported the result of the correlation fucntion $c(t)$, $n(t)$ in Fig. 6.6a and the reactive flux $k(t)$ in Fig. 6.6b.

In both cases, the $k(t)$ quickly changes from its initial value on a time scale of less than 0.2 ps. This value can be roughly seen from Fig. 6.7, which redraws the $k(t)$ in Fig. 6.5 and Fig. 6.6 in double logarithmic coordinates and compares them.

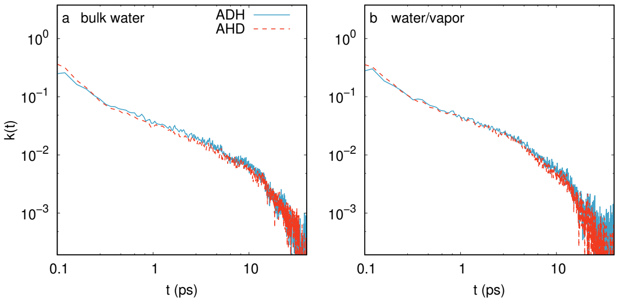

FIGURE 6.7: Time dependence of the correlation functions $k(t)$ of water–water H-bonds for (a) bulk water and (b) water/vapor interface at 300 K.

6.2 Distribution of Hydrogen Bond Lifetimes

The HB liefetime is a significant feature of the HB dynamics in liquids. The peculiar properties of water are a direct consequence of water's H-bond lifetime distribution.[181, 188, 200] For example, understanding of HB dynamics is essential when investigating proton transfer reactions in protein environments.[201] The statistical properties of lifetime of H-bonds can be described by a variety of distribution functions.[183, 192, 202, 203] Below we discuss the three probability distribution functions of HB lifetime, so that we can study the dynamic characteristics of H-bonds in liquids and interfaces.

Probability Distribution of HB Lifetimes in a Configuration Suppose that there are n_{tot} H-bonds in a system at time t, and we can distinguish a part of H-bonds from these H-bonds. The lifetime of this part of H-bonds is in a certain range $[\tau, \tau + d\tau]$. We can assume that their number of those bonds is n_τ. One can easily find that $n_{tot} > n_\tau$. If we observe this part of H-bonds in the next time period $[t, t + \tau]$, then they will be broken once during $[t, t + \tau]$. That is to say, within $[t, t + \tau]$, we will detect the breaking of all H-bonds with lifetime τ (see Fig. 6.8). Therefore, in a very short period of time $d\tau$, the probability of detecting these H-bonds is $(1/\tau)d\tau$. Since the probability for the HB to have the lifetime $\in [\tau, \tau + d\tau]$ is $P_t(\tau)$. Therefore, the relation between $P_a(t)$ and $P_t(t)$ is

$$P_a(t) = \int_t^\infty P_t(\tau) \frac{d\tau}{\tau}, \tag{6.12}$$

i.e., the probability of the HB breaking for the first time in the time t after detection at the initial moment depends on the number of those H-bonds whose lifetime exceeds the given time t. [191]

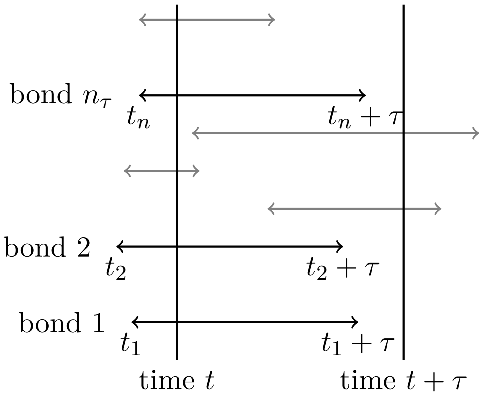

FIGURE 6.8: The H-bonds with lifetime τ in a certain configuration. At time t, we assume that there are totally n_{tot} H-bonds can be detected, and n_τ H-bonds are of lifetime τ, therefore, the fraction of H-bonds that have the lifetime τ in the configuration at time t is $P_{tc}(\tau) = n_\tau/n_{tot}$. Let τ take all the values in the interval $[0, \infty]$, we can get the HB lifetime distribution $P_{tc}(t)$.

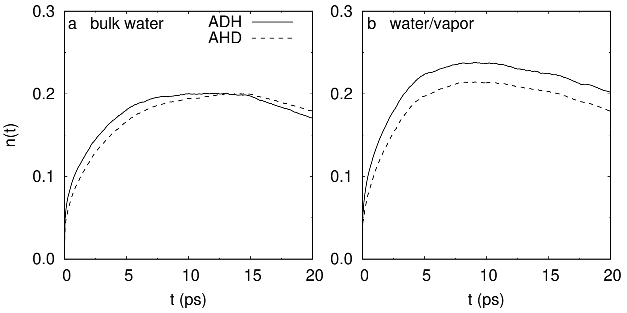

FIGURE 6.9: The time dependence of the population functions $n(t)$ for (a) bulk water and (b) water/vapor interface, as computed from the ADH (solid line) and AHD (dashed line) criterion of H-bonds with the expression $n(t) = \int_0^t dt' k_{in}(t')$.

k and k': Least Squares Fit The probability at time t that a pair of water molecules bonded by H-bonds at the initial moment does not be bonded but the distance between their oxygen atoms is still less than R^c_{OO} is

$$n(t) = \int_0^t dt' k_{in}(t'), \tag{6.13}$$

where $k_{in}(t) = -\langle \dot{h}(0)[1 - h(t)]h^d(t)\rangle / \langle h \rangle$ is the restricted rate function. Fig. 6.9a and Fig. 6.9b show the function $n(t)$ in Eq. 6.13 for bulk water and water/vapor interface, respectively. In each figure, we have drawn the $n(t)$ function corresponding to the two different HB definitions. It can be found that the overall trend of n(t) does not depend on the choice of HB definition. i.e., as t increases, $n(t)$ increases rapidly from 0, and it reaches a maximum value at $t \approx 10$ ps, and then gradually decreases. Comparing the two figures 6.9a and 6.9b, we find that the maximum value of $n(t)$ in the water/vapor interface is slightly higher than that in bulk water. This feature does not depend on the definitions of the HB we choose.

Khaliullin and Kühne have studied the H-bonding kinetics of pure water using AIMD simulations. [186] Based on the concepts of $h(t)$, $h^{(d)}(t)$, $n(t)$ and $k(t)$, they have used the simulation data obtained by the AIMD simulation method to obtain the ratio k/k' in the bulk water, and then the lifetime and relaxation time of the HB. Here, we also use the AIMD simulation method to study the HB dynamics at the interface of aqueous solutions. We can obtain the optimal solution range of k and k' from the relationship between the reactive flux and the HB population correlation function $c(t)$ and $n(t)$, and the two rate constants k and k', i.e.,

$$k(t) = kc(t) - k'n(t). \tag{6.14}$$

We can find the optimal value of the rate constants, k and k', by a least squares fit of the calculated data $k(t)$, $c(t)$ and $n(t)$ beyond the transition phase. The functions $c(t)$ can be regarded as a P-dimensional column vector composed by $(c(1), c(2), \cdots, c(P))^T$, and denoted as $\mathbf{c}$, with $c(i)$ representing the value of the correlation $c(t)$ at $t = i$. Similarly, the functions $n(t)$ and $k(t)$ can also be viewed as P-dimensional column vectors and can be denotd as $\mathbf{n}$ and $\mathbf{k}$, respectively. Therefore, the rate constants k and k' can be determined from the matrix $\mathbf{A} = \begin{bmatrix}\mathbf{c} & \mathbf{n}\end{bmatrix}$, i.e.,

$$\begin{bmatrix} k \\ -k' \end{bmatrix} = (\mathbf{A}^T\mathbf{A})^{-1}\mathbf{A}^T\mathbf{k}. \tag{6.15}$$

For bulk water and the water/vapor interface, the optimal k and k' are reported in Table 6.1 and 6.2.

TABLE 6.1: The k and k' for the bulk water and the water/vapor interface. We carried on the short time region 0.2 ps $< t <$ 2 ps. The unit for k (k') is ps^{-1}, and that for τ_{HB} ($= 1/k$) is ps.

Criterion	k (bulk)	k' (bulk)	τ_{HB} (bulk)	k (interf.)	k' (interf.)	τ_{HB} (interf.)
ADH	0.335	0.859	2.990	0.359	0.673	2.788
ADH(from k_{in})	0.296	0.988	3.380	0.323	0.765	3.101
AHD	0.333	1.041	2.999	0.352	0.785	2.841
AHD(from k_{in})	0.288	1.149	3.470	0.314	0.887	3.184

TABLE 6.2: The k and k' for the bulk water and the water/vapor interface. We carried on the long time region 2 ps $< t <$ 12 ps. The unit for k (k') is ps^{-1}, and that for τ_{HB} ($= 1/k$) is ps.

Criterion	k (bulk)	k' (bulk)	τ_{HB} (bulk)	k (interf.)	k' (interf.)	τ_{HB} (interf.)
ADH	0.115	0.031	8.687	0.159	0.058	6.279
ADH(from k_{in})	0.115	0.039	8.718	0.157	0.068	6.372
AHD	0.107	0.042	9.345	0.157	0.076	6.363
AHD(from k_{in})	0.105	0.047	9.496	0.155	0.088	6.472

To obtain the forward and backward rate constants (k and k'), here we performed the fitting in different time region $0.2 < t < 2$ ps and $2 < t < 12$ ps, respectively. We note that in the larger time region, i.e., $2 < t < 12$ ps, the value of HB lifetime τ_{HB} is larger than that in shorter time region, $0.2 < t < 2$ ps, no matter for the bulk water or for the interface. A larger τ_{re} value means that the distance between a water molecule and another water molecule stays within $r^c_{\mathrm{OO}} = 3.5$ Å for a longer time. For the long time region, these values of the k are comparable in magnitude to that obtained by Ref. [186]

$LiNO_3$ Solution For a given molecular configuration, $\{\mathbf{r}_i(t)\}$, Eq. 6.19 can be solved through interpolation on a spatial grid.[204] Fig. 6.10 illustrates the obtained instantaneous interfaces for one configuration of a slab of $LiNO_3$ solution at 300 K. We have taken $\{\mathbf{r}_i(t)\}$ to refer to the positions of all atoms except hydrogen atoms in the system, and because the bulk correlation length of liquid water is about one molecular diameter, we have used ξ =2.4 Å; further, we have used $\rho_0 = 0.016$ Å $^{-3}$, which is approximately one-half the bulk density of water.

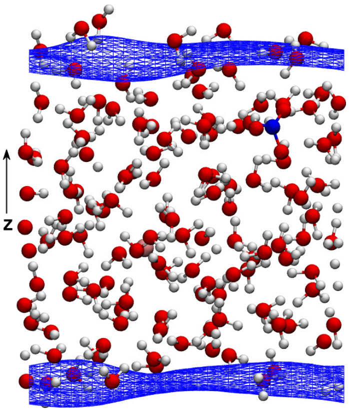

FIGURE 6.10: A slab of $LiNO_3$ solution with the instantaneous interface **s** represented as a blue mesh on the upper and lower phase boundary. The initial position of each ion in the solution is random. The slab is periodically replicated in the horizontal directions.

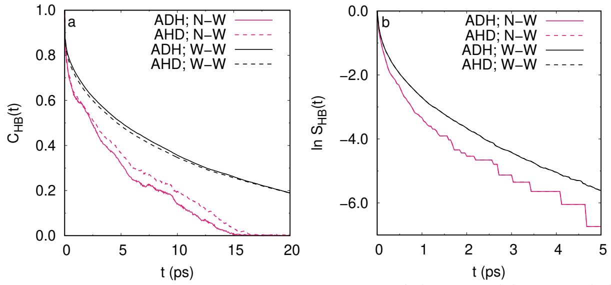

FIGURE 6.11: The time dependence of (a) $C_{\mathrm{HB}}(t)$ and (b) $\ln S_{\mathrm{HB}}(t)$ of all water–water and nitrate–water H-bonds at 300 K for the slab of $LiNO_3$ solution, as computed from the ADH (solid line) and AHD (dashed line) criterion of H-bonds. The definition of the correlation function is based on the specific HB configuration between molecules.

The results of the correlation functions $C_{\mathrm{HB}}(t)$ and $S_{\mathrm{HB}}(t)$ for both nitrate–water (N–W) and water–water (W–W) H-bonds are shown in Fig. 6.11a and 6.11b, respectively. For both HB definitions, it is found that the decay of the $C_{\mathrm{HB}}(t)$ and $S_{\mathrm{HB}}(t)$ for nitrate–water H-bonds is much faster than that for water–water H-bonds. From the relation 6.6, the faster relaxation of $S_{\mathrm{HB}}(t)$ implies that the nitrate–water H-bonds have shorter lifetime than the water–water H-bonds in the bulk phase. This result is obtained from a DFTMD simulation of a bulk phase of $LiNO_3$ solution at 300 K. The simulated system consisted of 127 water molecules and a Li^+–NO_3^- ion pair in a periodic cubic box of length $L = 15.79$Å, which corresponds to a density of 0.997 g cm^{-3}. The calculation results obtained from the simulations are in good agreement with numerous experimental results and simulation results. [170] It means that nitrate has structure-breaking ability, or compared with W–W interaction, N–W HB interaction is rather weak.

6.3 Water-water Pair Based Hydrogen Bond Dynamics

The method described in this paragraph is used more in the literature. The basis is the population operator $h(t)$ of the HB formed between two water molecules. We use the correlation function $C_{\mathrm{HB}}(t)$ to describe the relaxation of H-bonds between two water molecules: [176, 178, 205]

$$C_{\mathrm{HB}}(t) = \langle h(0)h(t)\rangle/\langle h\rangle. \tag{6.16}$$

Similarly, with the aid of the ergodic principle, the ensemble average $\langle\cdots\rangle$ is implemented by time average. The $\langle h\rangle$ is the probability that a pair of randomly chosen water molecules in the system is H-bonded at any time t.

The function $C_{\mathrm{HB}}(t)$ is interpreted as the probability that the HB between a certain pair of water molecules is intact at time t, if the pair of water molecules are H-bonded at time zero. In a large system that consist of many water molecules, the probability that a specific pair of water molecules are H-bonded is extremely small. Therefore, the $C_{\mathrm{HB}}(t)$ relaxes to zero, when t is large enough. The $C_{\mathrm{HB}}(t)$ measures correlation in $h(t)$ independent of any possible bond breaking events. It is one of the intermittent HB correlation functions, introduced by Rapaport, [183] and can be studied by a continuous function, probability densities.

Fig. 6.12 shows the correlation function $C_{\mathrm{HB}}(t)$ for bulk water over time. The result is calculated by DFTMD simulation, and the temperature is 300 K. Comparing Fig. 6.2 and Fig. 6.12, we find that although the trend of change of C_{HB} is very similar: as time increases, it gradually decays from 1; but from a quantitative point of view, the latter decays more slowly. This difference comes from our definition of the HB population operator h, and does not depend on the HB criterion. For example, from Fig. 6.12, we can see that the above conclusions are correct regardless of ADH or AHD criteria. It can be seen that our different definitions of the HB population operator will lead to different correlation functions related to it. To see the direct comparison of the $C_{\mathrm{HB}}(t)$ in the two cases, refer to the Appendix .

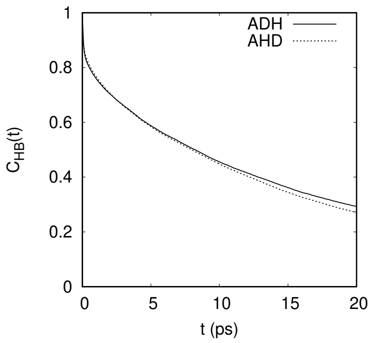

FIGURE 6.12: The correlation functions $C_{\mathrm{HB}}(t)$ for bulk water, based on water-water pair HB population operator $h(t)$, as computed from the ADH (solid line) and AHD (dashed line) criterion of H-bonds.

Instantaneous Interfaces As Willard and Chandler mentioned, due to molecular motions, interfacial configurations change with time, and the identity of molecules that lie at the interface also change with time, generally useful procedures for identifying interfaces must accommodate these motions. [204] To determine the instantaneous interface of the water/vapor system, we here adopted their proposed method based on spatial density. The instantaneous coarse-grained density at space-time point $\mathbf{r}, t$

can be expressed as polynmial

$$\bar{\rho}(\mathbf{r}, t) = \sum_i \phi(|\mathbf{r} - \mathbf{r}_i(t)|; \xi) \tag{6.17}$$

where $\mathbf{r}_i(t)$ is the position of the ith particle at time t and the sum is over all such particles, and

$$\phi(\mathbf{r}; \xi) = (2\pi\xi^2)^{-3/2} \exp(-r^2/2\xi^2) \tag{6.18}$$

is a normalized Gaussian functions for a 3-dimensional system, where r is the magnitude of $\mathbf{r}$, and ξ is the coarse-graining length. Equation 6.18 is introduced to improve the accurancy of the interface, such that we can extend the domain and make it a single unicom, i.e., no cavity exists in the domain. With the parameter ξ set, the interfaces can be defined to be the 2-dimensional manifold $\mathbf{r} = \mathbf{s}$ such that

$$\bar{\rho}(\mathbf{s}; t) = \rho_c \tag{6.19}$$

where ρ_c is a reference density. This instantaneous interface is a function of time as molecular configurations changes with time, that is $\mathbf{s}(t) = \mathbf{s}(\{\mathbf{r}_i(t)\})$.

Instantaneous Layering of the water/vapor interface After the instantaneous surface is defined, we can define an interface layer for any non-uniform fluid system. Specifically, for the simulated water/vapor interface system in the cuboid simulation box, we can get another two-dimensional manifold $\mathbf{s}_0(t)$ by moving the instantaneous surface $\mathbf{s}(t)$ determined above along the system's normal coordinate to a certain distance d, which is another surface. We use these two surfaces as the two boundaries of the interface we will study. In other words, at any time point t, the volume between the two surfaces $\mathbf{s}(t)$ and $\mathbf{s}_0(t)$ is defined as the instantaneous interface. Here, we use d to denote the thickness of the instantaneous interface. As long as we change the value of d, we can get interfaces with different thicknesses. Different values of d give us different layering strategies for the interface system.

Below we will combine the instantaneous interface and Luzar-Chandler's HB population operator [176] to select the H-bonds in the interface. The dynamics of these H-bonds will vary with the thickness d of the interface. By investigating the characteristics of HB dynamics in these interfaces, we can obtain the dynamical characteristics of various solution interfaces. As we will see later, this method can be extended to HB dynamics in various environments, such as H-bonds around certain ions, in bulk water, etc., so that we can more easily select H-bonds in a certain environment. These different environments have a common feature: because the molecular configuration changes over time, the usual method first selects these molecules or molecular pairs, and then determines the H-bonds in this special environment based on a HB criterion, and finally calculate the HB lifetimes or autocorrelation functions of the HB population operators. And here we are combining the general Luzar-Chandler HB population operator with the environment in which the HB is formed, that is, the space constraint satisfied by the configuration of the molecular pair. This combination can easily select those molecules and their H-bonds that meet arbitrary constraints when the molecular configuration changes.

Interfacial Hydrogen Bond Once we have determined the instantaneous surface $\mathbf{s}(t) = \mathbf{s}(\{\mathbf{r}_i(t)\})$, we can define interface H-bonds. We need the parameter d to define the thickness of the instantaneous interface. Now we can write the interface

HB population operator $h^s[\mathbf{r}(t)]$ as follows: It has a value 1 when the particular tagged molecular pair are bonded *and* both molecules are inside the instantaneous interface, and zero otherwise.

Similar to the correlation function $C_{\mathrm{HB}}(t)$ in Eq. 6.16, which describes the fluctuation of the general H-bonds, we define the correlation function $C^s_{\mathrm{HB}}(t)$ that describes the fluctuation of the interface H-bonds:

$$C^s_{\mathrm{HB}}(t) = \langle h^s(0)h^s(t)\rangle / \langle h^s\rangle. \tag{6.20}$$

Based on the function $C^s_{\mathrm{HB}}(t)$, we can define a similar correlation functions $k^s(t)$, $n^s_{\mathrm{HB}}(t)$, $S^s_{\mathrm{HB}}(t)$. Therefore, using these new correlation functions, we can study the dynamics of interface H-bonding.

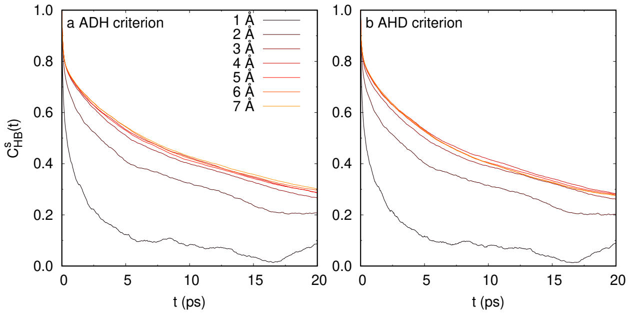

FIGURE 6.13: The correlation functions $C^s_{HB}(t)$ for the instantaneous interfacial H-bonds, based on water-water pair HB population operator $h^s(t)$, as computed from the (a) ADH and (b) AHD criterions of H-bonds.

$C^s_{\mathrm{HB}}(t)$ as function of d For the pure water interface, we used two geometric criteria for defining H-bonds to calculate the correlation function $C^s_{HB}(t)$. The calculation results are shown in Fig. 6.13. We find that the greater the thickness of the interface is selected, the slower the relaxation of the interface H-bonds. When the thickness of the interface is greater than a certain thickness d^c (~ 5 Å), the relaxation of H-bonds at the interface hardly changes.

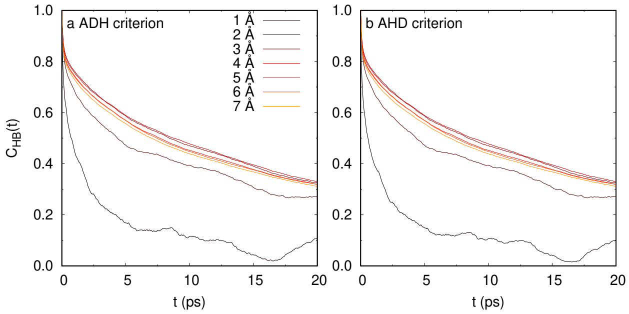

FIGURE 6.14: The correlation functions $C_{\mathrm{HB}}(t)$ for the instantaneous interfacial H-bonds, based on water-water pair HB population operator $h(t)$, as computed from the (a) ADH and (b) AHD criterions of H-bonds. These results are based on selecting the water molecules in the interface and then averaging the HB dynamics of these water molecules. Sampling is performed every 4 ps.

For comparison, let us look at the HB dynamics of water molecules in the interface obtained by selecting molecules located in instantaneous interface. (See Appendix

E.2) The characteristic of this algorithm is to first select the molecules in the interface at each moment and make a statistical average of the calculated correlation functions. Specifically, in order to determine which water molecules are located in the interface, we sample at regular intervals, and then calculate the correlation function $C_{\mathrm{HB}}(t)$ for the water molecules located in the interface and do a statistical average. As the thickness d of the instantaneous interface changes, the auto-correlation function of H-bonds in the interface we get will also change. Figure 6.14 shows how the function $C_{\mathrm{HB}}(t)$ changes with the thickness d of the interface. The sub-figure (a) and (b) use HB definition criterion ADH, and AHD, respectively. Comparing Fig. 6.13 and Fig. 6.14, we see that when we use the method of selecting molecules in the interface, the dependence of the correlation function $C_{\mathrm{HB}}(t)$ ($C^{s}_{\mathrm{HB}}(t)$) on the interface thickness is very consistent with the results obtained by the above-mentioned method. Moreover, regardless of the AHD definition or the ADH definition of the HB, this conclusion is valid. Since we want to study the HB dynamics in the interface, not just the correlation functions $C_{\mathrm{HB}}(t)$ or $C^{s}_{\mathrm{HB}}(t)$ in the interface, we will further examine the correlation functions $C_{\mathrm{HB}}(t)$ ($C^{s}_{\mathrm{HB}}(t)$), $n(t)$, $k(t)$, and the rate constants k, k' determined by these correlation functions.

Rate Constants k and k' Figure 6.15 compares the rate constants (k and k') and the lifetime τ_{HB} obtained by the two different methods mentioned above, i.e., IHB and molecule selection methods. We see that, whether it is k, k' or τ_{HB}, their changing *trend* with the thickness d of the interface is only slightly affected by the calculation method we use. In other words, no matter which method is used, the changes of k and k' with respect to d is the same. To illustrate this point more clearly, we compare the k, k' and τ_{HB} obtained under the two methods.

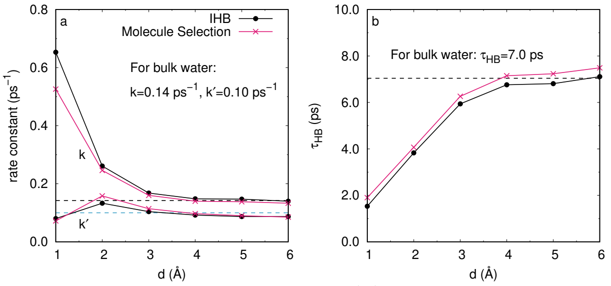

FIGURE 6.15: The dependence of (a) the rate constants k and k' and (b) the lifetime τ_{HB} on the interface thickness, obtained by the Instantaneous interface Hydrogen Bond (IHB) and by selecting the water molecules in the interface, respectively. The corresponding k, k' and τ_{HB} in the bulk water are also drawn with dashed lines as a reference. In sub-figure (a), the k of bulk water is represented by a *black dashed* line, and its k' is represented by a *blue dashed* line; in sub-figure (b), the τ_{HB} of bulk water is represented by a *black dashed* line. The constants are calculated based on the ADH criterion of H-bonds and the least square fits are carried on the time region 0.2 ps $< t <$ 12 ps.

Moreover, we can see from Fig. 6.15 that when the thickness is large enough ($d_0 \sim 3$ Å), these two constants agree well quantitatively. This very good result shows that the two extreme statistical methods (see Appendix E.2) used to calculate the HB dynamics of the interface did not produce much difference for the time scale (10^2 ps) and the scale (10^2 Å) of the simulation box we currently use.

We also found that when we look at the molecules in the interface whose thickness is less than d_0, the values of the rate constants depend on the method we use. That is, the k obtained by using the IHB method is relatively larger than the molecule selection method, and k' is relatively smaller. At the same time, since $\tau_{\mathrm{HB}} = 1/k$, this directly leads to a relatively shorter HB lifetime using the IHB method. This is related to our definition of IHB, and it is the same as our expectations: The definition of interface H-bonds makes the HB break rate on the interface artificially increased. At the same time, we know that the molecule selection method retains the original rate constant of H-bonds, but it may include the contribution of bulk water molecules to the rate constant. Therefore, the molecule selection method will underestimate the k.

In Fig. 6.15, the k, k' and τ_{HB} for the *bulk* water are also drawn with dashed lines as a reference. Comparing the above-mentioned physical quantities in the pure water interface and bulk water, we found that when the interface thickness $d > d_0$, no matter which statistical method is used, the value of the reaction rate constants of the interface water we get is *greater* than that in the bulk water. Therefore, since the HB lifetime can be calculated by $\tau_{\mathrm{HB}} = 1/k$, the value of τ_{HB} in interface water is smaller than that in bulk water.

From Fig. 6.15, we also find that as the interface thickness d increases, the values of k and k' also tend to the values of rates in the bulk water at the same condition. These results are all obtained by the least squares method in the same interval (0.2–12 ps). This verifies that the IHB method can get as good results as the method of molecule selection when $d > d_0$. At the same time, because the IHB is easier to operate, this method can calculate the HB dynamics and thus HB lifetime on the interface when the $d > d_0$ (in this case, $d_0 \sim 3$ Å or the size of 2–3 water molecules). We also noticed that the selection of water molecules and the statistical averaging depend on our sampling density on the trajectory of the simulated system, and the new method does not require such sampling. Therefore, the IHB method is more efficient than the traditional method.

The more realistic HB dynamical properties of interface molecules are between the results of the above two methods. Therefore, it is possible to approximate the true appearance of the HB dynamics of the interface molecules, by both the IHB method and the molecule selection method if the thickness of the interface is selected large enough.

In summary, if we study the dynamics of H-bonds in a very thin interface, we can use the method of molecular selection, because the H-bonds obtained in this way are not artificially broken, and if the interface is thick enough (see Fig. 6.15a), then we can use the IHB method, because it can automatically define which H-bonds come from the interface without the need to select the water molecules in the interface layer.

Table 6.3: The k and k' for the interfacial hydrogen dynamics of the water/vapor interface (by the method of IHB and of ADH criteria). We carried on the longer time region 0.2 ps $< t <$ 12 ps. The unit for k (k') is ps^{-1}, and for τ_{HB} ($= 1/k$) is ps. The thickness d (Å) denotes the thickness of the interface, which is obtained from the instantaneous surface. The parameter values and units are the same below.

Thickness	k	k'	$\tau_{\mathrm{HB}}(= 1/k)$
1.0	0.653	0.080	1.53
2.0	0.261	0.133	3.83
3.0	0.168	0.104	5.94
4.0	0.148	0.092	6.76
5.0	0.147	0.087	6.81
6.0	0.139	0.087	7.17

Table 6.4: The k and k' for the interfacial hydrogen dynamics of the water/vapor interface (by the method of IHB and of AHD criteria).

Thickness	k	k'	$\tau_{\mathrm{HB}}(= 1/k)$
1.0	0.661	0.080	1.51
2.0	0.265	0.133	3.77
3.0	0.172	0.102	5.82
4.0	0.148	0.090	6.74
5.0	0.149	0.084	6.72
6.0	0.144	0.078	6.93

Table 6.5: The k and k' for the interfacial hydrogen dynamics of the water/vapor interface (by the method of molecule selection and of ADH criteria).

Thickness	k	k'	$\tau_{\mathrm{HB}}(= 1/k)$
1.0	0.526	0.072	1.90
2.0	0.246	0.158	4.07
3.0	0.160	0.114	6.26
4.0	0.140	0.097	7.15
5.0	0.138	0.090	7.24
6.0	0.133	0.085	7.49

Table 6.6: The k and k' for the interfacial hydrogen dynamics of the water/vapor interface (by the method of molecule selection and of AHD criteria).

Thickness	k	k'	$\tau_{\mathrm{HB}}(= 1/k)$
1.0	0.610	0.083	1.64
2.0	0.235	0.142	4.62
3.0	0.138	0.102	7.22
4.0	0.141	0.098	7.07
5.0	0.120	0.078	8.40
6.0	0.119	0.071	8.39

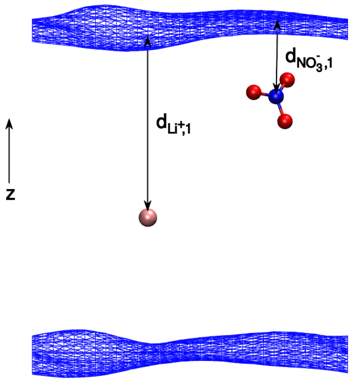

FIGURE 6.16: The distances between ions and the instantaneous surfaces (blue meshes) for a slab of aqueous $LiNO_3$ solution.

Interface of Lithium Nitrate Solutions For the molecular dynamics trajectory of a solution interface, we can now get instantaneous surface. For any molecule or ion α in such a solution interface system, we can get its distance from the instantaneous surface. We assume that the z-axis is the normal direction, then the distances between the particle and the instantaneou surfaces are:

$$d_{\alpha,1}(t) = z_{\alpha,1}^{surf}(t) - z_\alpha(t), d_{\alpha,2}(t) = z_\alpha(t) - z_{\alpha,2}^{surf}(t), \tag{6.21}$$

where $z_\alpha(t)$ is the coordinate of the particle α in the normal direction at time t, $z_{\alpha,i}^{surf}(t)$ is the z coordinate of the surface position corresponding to particle α at time t, and the subscripts $i = 1$ and 2 respectively identify the lower and upper instantaneous surfaces. As an example, Fig. 6.16 shows the distances, $d_{\mathrm{Li}^+,1}$ and $d_{\mathrm{NO}_3^-,1}$, between ions and one of the instantaneous surfaces at a certain moment.

Figure 6.17 shows the time dependence of the distance between the anion (cation) and the instantanous surface in the $LiNO_3$ solution at 300 K. We found that when the system reaches an equilibrium state, the lithium ions are stably within a few angstroms below the interface, while the nitrate ion are more willing to be on the surface. When the system is in equilibrium ($t > 10$ ps), the distance $d_{\mathrm{NO}_3^-,1}$ is around 0, which indicates that nitrate ions are on the instantanous interface. Therefore, the results calculated using the instantaneous interface are consistent with the results of the SFG spectra of the $LiNO_3$ solution. (See Fig. 5.3 and Fig. 5.4.)

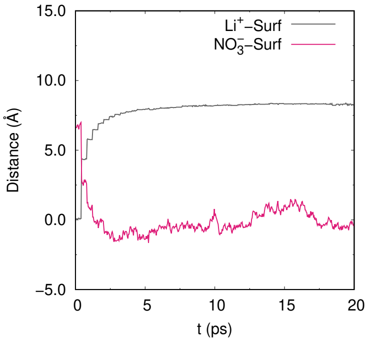

FIGURE 6.17: Time dependence of the cation–surface and nitrate–surface distances at 300 K.

I⁻–Water Hydrogen Bonds in Aqueous Solutions Hydrogen bonds between water molecules and other species also play decisive role in chemical and biological systems. For the research of this type of H-bond, some results obtained by molecular simulations have been published. For example, the HB dynamics of surfactant–water and water–water H-bonds at the air/water interface has been analyzed by Chanda and Bandyopadhyay with atomistic molecular dynamics.[171] Similar analyse for nitrate–water is also done by Yadav, Choudhary and Chandra by first-principles MD simulations.[206] In the case of water–water H-bonds, the critical distance of $r^c_{\mathrm{OO}} = 3.5$ Å are the position of the first minimum of the oxygen–oxygen RDF. For the anion–oxygen H-bonds, we can use the similar criteria. The cutoff values for X–oxygen distance are obtained from the positions of the first minimum of the X–oxygen RDF, i.e., $R^c_{\mathrm{XO}} = 4.1, 3.7$ Å, for X = I^- and nitrate O. We have still used 30° for the anglar cutoff.[187] The function C_{HB} of I^-–water and water–water H-bonds describes the structural relaxation of these H- bonds. The results of the $C_{\mathrm{HB}}(t)$ are shown in Fig. 6.19.

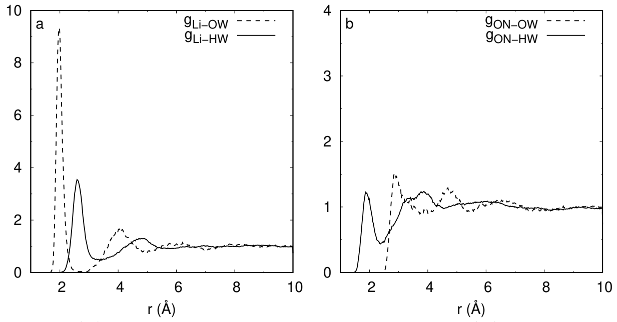

FIGURE 6.18: (a)Li–water O, Li–water H RDFs; (b) Nitrate O–water O, nitrate O-water H RDFs for $\mathrm{LiNO_3}$ solutions at 300 K.

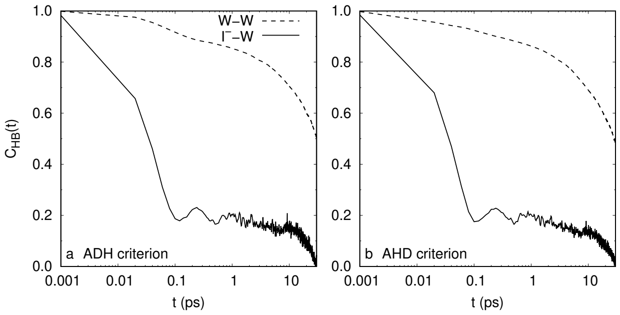

FIGURE 6.19: Time dependence of the intermittent correlation functions $C_{\mathrm{HB}}(t)$ of I^-–water (I^-–W) and water–water H-bonds at 300 K. A base-10 log scale is used for the x-axis.

The results of the continuous correlation functions for both definitions (ADH and AHD criterions) for the H-bonds are shown in Fig. 6.20 for I^-–water H-bonds. The results of water–water H-bonds are also included for comparison in both Fig. 6.20 a and b.

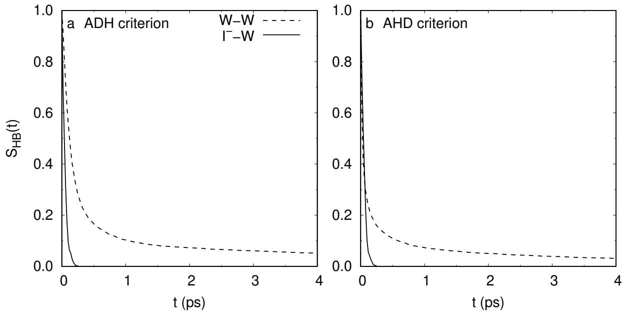

FIGURE 6.20: Time dependence of the continuous correlation functions $S_{\mathrm{HB}}(t)$ of I^-–water (I^-–W) and water–water H-bonds at 300 K.

For both definitions for the H-bonds, it is found that the I^-–water H-bonds show faster dynamics than water–water H-bonds. (consistent to the previous MD results.) Therefore, the time scales of the relaxation of these H-bonds can be obtained for both definitions. In Table 6.7, we have included the average lifetimes $\langle \tau_a \rangle$ for both water–water and I^-–water H-bonds. We performing the fitting in the time region 0.2 ps $< t <$ 12 ps to calculate the forward and backward rate constants for HB breaking.

TABLE 6.7: The Dynamical properties of anion–water and water–water H-bonds at 300 K. Data are from DFTMD for the aqueous solutions. The values are expressed in ps.

Quantity	Criterion	W–W	I^-–W	NO_3^-–W
$\langle \tau_a \rangle$	ADH	190.3	0.10	4.35
$\langle \tau_a \rangle$	AHD	186.8	0.11	7.91
$1/k$	ADH	9.82	2.80	4.15
$1/k$	AHD	8.97	2.40	6.02

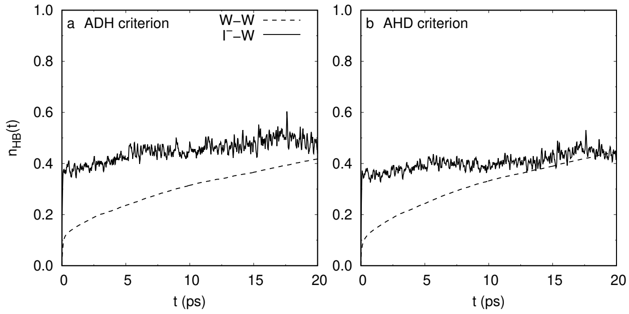

FIGURE 6.21: Time dependence of the correlation functions $n_{\mathrm{HB}}(t)$ of I^-–water (I^-–W) and water–water H-bonds at 300 K.

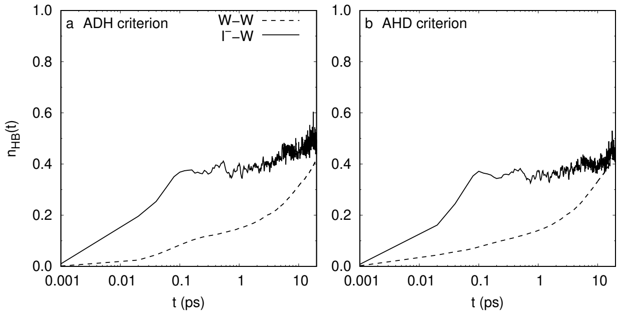

FIGURE 6.22: Time dependence of the correlation functions $n_{\mathrm{HB}}(t)$ of I^-–water (I^-–W) and water–water H-bonds at 300 K. A base-10 log scale is used for the x-axis.

Experiments on HB Dynamics An important structural characteristic of the H-bonded network is the average number of H-bonds per molecule, $\langle h_{i,j} \rangle$. [168] For bulk water systems, we find that in the DFTMD simulations the average number of H-bonds in the bulk phase is ~ 4.35 which is slightly (higher) than the usual estimate of 3.4 (interface system) for SPC/E water.

Chapter 7

Summary

Using DFTMD simulations, we have analyzed the interfacial structure and dynamics of electrolyte solutions containing alkali nitrates. In particular we have presented a detailed analysis of the HB structure at the interface and we have calculated the interface vibrational spectra in order to provide a molecular interpretation of available experimental data.

As a first system we have analyzed the behaviour of a salty water/vapor interface containing $LiNO_3$. Both the measured and calculated SFG spectra shows a reduced intensity of the lower frequency portion region, when compared to the pure water/-vapor interface. This reduction is attributed to the H-bonds established between the NO_3^- and the surrounding water molecules at the interface. This effects is only related to the presence of NO_3^- at the water surface and is not affected by the presence of alkali metal ions. Indeed we have shown that although the Li^+ can reside relative close to the water surface, also forming a water mediated ion pair with NO_3^-, its effect on the SFG spectrum is not visible. The water molecule which mediate the interaction between the NO_3^- and the Li^+ would produce a red-shifted peak in small water cluster, but its influence is not visible neither in the SFG spectra. To verify this conclusion, the free energy of different configurations was also calculated for larger water clusters in CP2K by the Blue-Moon method. The results still give consistent results: Li^+–NO_3^- ion pairs separated by a water molecule have lower free energy than the configuration in which Li^+ is in direct contact with NO_3^-.

We have also shown that the use of simple models, such as small cluster is not suitable to reproduce the experimental spectra and cannot provide a microscopic interpretation of the spectra. Realistic models of the interface are required to address the perturbation of the ion on the water surface. The elucidated mechanism is possibly more general to anions which have high propensity for the water surface, as for example other molecular ions.

The difference between the HB dynamics of H-bonds outside the first shell of the Li^+ and that of nitrate-water H-bonds at interfaces is not visible from the values of the HB relaxation time. They reflect the difference between HB dynamics in bulk water and that at the water/vapor interfaces. For the water/vapor interface of alkaline iodine solutions, we find that the cations does not alter the H-bonding network outside the first hydration shell of cations. It is concluded that no long-range structural-changing effects for alkali metal cations.

From the results of nonlinear susceptibilities, which shows bonded OH-stretching peaks with higher frequencies, we conclude that the water molecules at the water/-vapor interfaces of LiI, NaI, and KI solutions are participating in weaker H-bonds, compared with those at the pure water surface. This conclusion is based on the DFTMD simulations, and the origin of the characteristics may come from a unique distribution of I^- ions and alkali metal cations, which form a double layer [165] over the thickness on the order of 5–10 Å (see Appendix D).

For the bulk system, starting from the data obtained from the DFTMD simulation, based on the HB population operator, we calculated the correlation functions $C(t)$, $n(t)$ and $k(t)$ related to it, and obtained the reaction rate constants with the HB formation and breakage in the system, and then obtained the information of the HB lifetime. In order to analyze the HB dynamics on the interface, we propose a statistical method which is based on the instantanous interface HB population operator for the instantaneous interface. Compared with traditional statistical methods, it is easier to implement and more efficient, because it does not need to consider which molecules are within the instantaneous interface, so there is no need to select the molecules on the interface and calculate the statistical average of physical quantities. Except for the case where the interface thickness is less than the size of 2 to 3 water molecules, this method can efficiently analyze the HB dynamics and HB lifetime distribution of the instantaneous interface. We took pure water interface and $LiNO_3$ solution as examples, and applied the above method to analyze the HB kinetics and HB lifetime on the interface. This set of methods can be easily applied to general interface systems or solutions. As we did in paragraph 6.2 and 6.3, we studied the population operators of nitrate ion–water hydrogen bond and iodide ion–water hydrogen bond and their correlation functions. In general solutions, water–water H-bonds can be extended to ion–water H-bonds, and then similar analysis can be done to study the HB dynamics.

Appendix A

Calculation of Nonlinear Optical Susceptibilities

Definitions and Relations 1. Definition of double product of a m-order tensor A and a n-order tensor B is a tensor with order $m+n-2$.

$$A : B = A_{ij}B_{lm}\delta_{jl}\delta_{im}. \tag{A.1}$$

2. The components of product of AB is defined by

$$(AB)_{ijlm} = A_{ij}B_{lm}. \tag{A.2}$$

3. For vectors $\mathbf{a}$, $\mathbf{b}$, $\mathbf{c}$ and $\mathbf{d}$, $\mathbf{ab} : \mathbf{cd} = (\mathbf{a}\cdot\mathbf{d})(\mathbf{b}\cdot\mathbf{c})$.
Proof:

$$\begin{aligned}\mathbf{ab} : \mathbf{cd} &= (\mathbf{ab})_{ij}(\mathbf{cd})_{lm}\delta_{jl}\delta_{im} \\ &= (\mathbf{ab})_{ij}(\mathbf{cd})_{ji} \\ &= (a_ib_j)(c_jd_i) \\ &= (\mathbf{b}\cdot\mathbf{c})(\mathbf{a}\cdot\mathbf{d})\end{aligned} \tag{A.3}$$

Proof of Eq. 2.41 Since

$$i\int_0^\infty dte^{-it(a-ib)} = \frac{1}{a-bi}, \tag{A.4}$$

set $a = (\omega_{v'} - \omega_v) - \omega$, and $b = \gamma_{v'v}$, then we have

$$\int_0^\infty dte^{-it((\omega_{v'}-\omega_v)-\omega-i\gamma_{v'v})} = \frac{-i}{(\omega_{v'}-\omega_v)-\omega-i\gamma_{v'v}},$$

which is Eq. 2.41.

Derivation of Eq. 2.45 Now we give the derivation of the expression of $\chi^{(2),\mathrm{R}}$

$$\chi^{(2),\mathrm{R}}_{\eta\xi\kappa} = \frac{-i}{k_{\mathrm{B}}T\omega}\int_0^\infty dte^{i\omega t}\left\langle \dot{A}_{\eta\xi}(t)\dot{M}_\kappa(0)\right\rangle \tag{A.5}$$

Derivation: The resonant term $\chi^{(2),R}_{\eta\xi\kappa}$ is given by [28]

$$\chi^{(2),\mathrm{R}}_{\eta\xi\kappa} = \frac{i\omega}{k_{\mathrm{B}}T}\int_0^\infty dte^{i\omega t}\left\langle A_{\eta\xi}(t)M_\kappa(0)\right\rangle, \tag{A.6}$$

Molecular Dipole Moment and Dipole Polarizibility Derivatives The polarizability tensor $\boldsymbol{\alpha}$ is defined by the relation

$$\delta\boldsymbol{\mu} = \boldsymbol{\alpha}\mathscr{E} \tag{A.7}$$

where $\delta\boldsymbol{\mu}$ is the electric dipole moment (a vector) induced in the molecule by the electric field $\mathscr{E}$, with the components $\mathscr{E}_x$,$\mathscr{E}_y$ and $\mathscr{E}_z$. Now we describe the main algorithm to implement the parametrization of the molecular dipole moment derivative $\frac{\partial\mu_k}{\partial r}$ and dipole polarizibility derivative $\frac{\partial\alpha_{\eta\xi}}{\partial r}$. This result can be used in the velocity ACF-based method for calculating the VSFG spectroscopy intensity.

Given a DFT MD trajectory of total length $\sim 10^2$ ps for bulk water, sampled with a frequency ~ 1 ps^{-1}. For the j-th water molecule in the n-th snapshot of the trajectory, we denote the two OH bonds as $\mathrm{H}^{n,j,\epsilon=1}$ and $\mathrm{H}^{n,j,\epsilon=-1}$. We will calculate statistical average over all time steps and all OH bonds, therefore, we just denote the corresponding OH bonds by $\epsilon = 1$ and $\epsilon = -1$, respectively. The H atoms in a water molecule are denoted by $\mathrm{H}^{\epsilon=1}$ and $\mathrm{H}^{\epsilon=-1}$, and the O atom by O^0.

We used three different frameworks: the lab framework $(x^{\mathrm{l}}, y^{\mathrm{l}}, z^{\mathrm{l}})$, the molecular framework $(x^{\mathrm{m}}, y^{\mathrm{m}}, z^{\mathrm{m}})$ and the bond framework $(x^{\mathrm{b}}, y^{\mathrm{b}}, z^{\mathrm{b}})$ (see Fig. 2.2). In the lab framework, the z^{l}-axis is perpendicular to the interface. The molecular frame will be used to decompose the signal into normal modes of water monomers. For the j-th molecule, the z^{m} axis is along the bisector of the H-O-H angle, the x^{m} axis is in the molecular plane, and the y^{m} axis is out of the molecular plane. In the bond framework, $z^{\mathrm{b},\epsilon}$ axis is along the bond ϵ of a molecule, $z^{\mathrm{b},\epsilon}$ is in the molecular plane and $y^{\mathrm{b},\epsilon}$ is out of the molecular plane.

There are two direction cosine matrices between the bond frameworks and molecular framework, we name them as $\mathbf{D}^{\mathrm{b},\epsilon=-1}$ and $\mathbf{D}^{\mathrm{b},\epsilon=1}$, [117] or $\mathbf{D}^{\mathrm{b},-1}$ and $\mathbf{D}^{\mathrm{b},1}$ for short. Then the direction matrix $\mathbf{D}^{\mathrm{b},\epsilon}$ can be represented by direction cosines between $\mathbf{x}^{\mathrm{b},\epsilon}$ and $\mathbf{x}^{m}$, where $\epsilon = \pm 1$ and θ denotes the H-O-H angle in the j-th water molecule for the n-step:

$$\hat{x}_1^{\mathrm{b},\epsilon} = \epsilon\cos\frac{\theta}{2}\hat{x}_1^m + \sin\frac{\theta}{2}\hat{x}_3^m \tag{A.8a}$$

$$\hat{x}_2^{\mathrm{b},\epsilon} = \epsilon\hat{x}_2^m \tag{A.8b}$$

$$\hat{x}_3^{\mathrm{b},\epsilon} = -\epsilon\sin\frac{\theta}{2}\hat{x}_1^m + \cos\frac{\theta}{2}\hat{x}_3^m \tag{A.8c}$$

i.e.,

$$\mathbf{D}^{\mathrm{b},\epsilon} = \begin{pmatrix} \epsilon\cos\frac{\theta}{2} & 0 & \sin\frac{\theta}{2} \\ 0 & \epsilon & 0 \\ -\epsilon\sin\frac{\theta}{2} & 0 & \cos\frac{\theta}{2} \end{pmatrix}. \tag{A.9}$$

The molecular framework is given by the direction cosine matrix $\mathbf{D}^{\mathrm{m,l}}$ (or $\mathbf{D}^{\mathrm{m}}$) between molecular framework and the lab framework

$$\hat{\mathbf{x}}^m = \mathbf{D}^{\mathrm{m}}\hat{\mathbf{x}}^l. \tag{A.10a}$$

The dipole moment of each OH bond with different length is requird to determine the dipole moment derivative. Therefore, we elongate (reduce) one bond ϵ by $\Delta r = 0.05$ Å ($\Delta r = -0.05$ Å), and keep other bonds in the total system still, then we obtain a updated coordinate. Then the MLWF centers for the system can be calculated from the updated coordinate, using force and energy calculation at the DFT level. From the Wannier centers of the j-th water molecule, we can calculate the dipole moment for the elongated (reduced) bond ϵ. In the bond frame, $|\mu^b| = |\mu^b_z|$. Therefore, we can calculate the $k = z$ component of the dipole moment for ϵ in water molecule j from the MLWF centers. [207] The MLWF centers are computed and the partial dipole moment for a given molecular species I is defined as [126]

$$\mu^I = \sum_{i \in I} (Z_i \mathbf{R}_i - 2 \sum_{n \in i} \mathbf{r}^w_n). \tag{A.11}$$

In particular, here it is expressed as

$$\mu^{\mathrm{b},r+\Delta r,\epsilon} = \frac{1}{2} Z_{\mathrm{O}} \mathbf{R}^0 + Z_{\mathrm{H}} \mathbf{R}^{\epsilon} - 2r^{w,\epsilon} - 2r^{w,0}, \tag{A.12}$$

where $\epsilon = \pm 1$. In the ϵ frame, the $k = z$ component dipole moment derivative with respect to bond length [208] for the single OH bond ϵ in water molecule j is

$$\frac{\partial \mu^{\mathrm{b},\epsilon}}{\partial r} = (\mu^{\mathrm{b},r+\Delta r,\epsilon} - \mu^{\mathrm{b},r,\epsilon})/\Delta r. \tag{A.13}$$

Since the components of the dipole moment in the molecular framework are given by the transformation:

$$\begin{pmatrix} (\frac{\partial \mu^{\mathrm{m}}}{\partial r})_1 \\ (\frac{\partial \mu^{\mathrm{m}}}{\partial r})_2 \\ (\frac{\partial \mu^{\mathrm{m}}}{\partial r})_3 \end{pmatrix} = \mathbf{D}^{\mathrm{b},\epsilon} \begin{pmatrix} 0 \\ 0 \\ \frac{\partial \mu^{\mathrm{b},\epsilon}}{\partial r} \end{pmatrix}, \tag{A.14a}$$

then, to calculate the individual polarizability for a OH bond from Wannier centers, calculations involving finite electric fields (of 0.0001 au intensity) were performed independently along x, y, and z directions at each sampled time step. [127] For the electric field $\mathscr{E} \in \{\mathscr{E}_x, \mathscr{E}_y, \mathscr{E}_z\}$, like in the case of no external electric field, the MLWF centers are calculated. For a finite Δr, the dipole moment is given by

$$\mu^{b,r+\Delta r,\epsilon,\mathscr{E}} = Z_H \mathbf{R}^{\epsilon,\mathscr{E}} + \frac{1}{2} Z^0 \mathbf{R}^{0,\mathscr{E}} - 2\mathbf{r}^{\mathrm{w},\epsilon,\mathscr{E}} - 2\mathbf{r}^{\mathrm{w},0,\mathscr{E}}. \tag{A.15}$$

From the relation (obtained from Eq. A.7)

$$0 = \alpha_{11}^{b,r+\Delta r} \mathscr{E}_1 + \alpha_{12}^{b,r+\Delta r} \mathscr{E}_2 + \alpha_{13}^{b,r+\Delta r} \mathscr{E}_3 \tag{A.16a}$$

$$0 = \alpha_{21}^{b,r+\Delta r} \mathscr{E}_1 + \alpha_{22}^{b,r+\Delta r} \mathscr{E}_2 + \alpha_{23}^{b,r+\Delta r} \mathscr{E}_3 \tag{A.16b}$$

$$\delta \mu_3^{b,r+\Delta r} = \alpha_{31}^{b,r+\Delta r} \mathscr{E}_1 + \alpha_{32}^{b,r+\Delta r} \mathscr{E}_2 + \alpha_{33}^{b,r+\Delta r} \mathscr{E}_3. \tag{A.16c}$$

where

$$\delta \mu_3^{b,r+\Delta r} = \mu_3^{b,\epsilon,r+\Delta r,\mathscr{E}} - \mu_3^{b,\epsilon,r+\Delta r}. \tag{A.17}$$

and the expressions of the electric filed $\mathscr{E}^{\mathrm{b}}$ in a OH framework for the 3 cases of external eletric field which is along x, y and z axis in the lab framework, respectively, we obtain 9 equations. For

$$\mathscr{E}^{\mathrm{l}} = (\mathscr{E}_0, 0, 0)^T$$

where $\mathscr{E}_0 = 0.0001$ au, we can obtain the intensity of the external electric filed in the molecular framework

$$\mathscr{E}_1^{\mathrm{m}} = \mathbf{D}_{12}^{\mathrm{m}}\mathscr{E}_2^{\mathrm{l}} \tag{A.18a}$$

$$\mathscr{E}_2^{\mathrm{m}} = \mathbf{D}_{22}^{\mathrm{m}}\mathscr{E}_2^{\mathrm{l}} \tag{A.18b}$$

$$\mathscr{E}_3^{\mathrm{m}} = \mathbf{D}_{32}^{\mathrm{m}}\mathscr{E}_2^{\mathrm{l}}, \tag{A.18c}$$

where $\mathbf{D}_{pq}^{\mathrm{m}}$ is the pq-component of $\mathbf{D}^{\mathrm{m}}$. In OH bond framework,

$$\mathscr{E}^{\mathrm{b}} = \mathbf{D}^{\mathrm{b}}\mathscr{E}^{\mathrm{m}}. \tag{A.19}$$

Similarly, we obtain similar (but different) expansions of the intensity of the electric field for the other two cases: when $\mathscr{E}^{\mathrm{l}} = (0, \mathscr{E}_0, 0)^{\mathrm{T}}$ and when $\mathscr{E}^{\mathrm{l}} = (0, 0, \mathscr{E}_0)^{\mathrm{T}}$, respectively. Here, $\mathscr{E}_x$ is the electric field along x-axis in the lab frame. Then the dipole polarizability for the bond ϵ is as follows:

$$\frac{\partial\alpha_{31}^{b,\epsilon}}{\partial r} = (\alpha_{31}^{b,\epsilon,r+\Delta r} - \alpha_{31}^{b,\epsilon,r})/\Delta r \tag{A.20a}$$

$$\frac{\partial\alpha_{32}^{b,\epsilon}}{\partial r} = (\alpha_{32}^{b,\epsilon,r+\Delta r} - \alpha_{32}^{b,\epsilon,r})/\Delta r \tag{A.20b}$$

$$\frac{\partial\alpha_{33}^{b,\epsilon}}{\partial r} = (\alpha_{33}^{b,\epsilon,r+\Delta r} - \alpha_{33}^{b,\epsilon,r})/\Delta r. \tag{A.20c}$$

Therefore, the average for $(\frac{\partial\mu^{\mathrm{b},\epsilon}}{\partial r})_\kappa$ and $(\frac{\partial\alpha^{\mathrm{b},\epsilon}}{\partial r})_{\eta\xi}$ (The subscripts $\kappa, \eta, \xi = x^m, y^m, z^m$, or $1, 2, 3$) over all OH bonds gives the molecular dipole and polarizability derivatives.

Appendix B

Structural Characterization of Water Clusters

The structural parameters of the considered water clusters are shown here. Table B.5 gives the average HB lengths r_a (with standard deviations)in $[NO_3{\cdot}(H_2O)_3]^-$. Table B.2 (B.3) reports the selected distances characterizing $[NO_3{\cdot}(H_2O)_3]^-$ ($RNO_3(H_2O)_3$), and Table B.4 the selected parameters for RNO_3 $(H_2O)_3$ (R=Li, Na, K). The unit for length and angle are Å and degree (°), respectively.

Table B.1: The HB lengths r_a in $[NO_3{\cdot}(H_2O)_3]^-$ at 300 K.

HB bound to	r_a
w1	2.40±0.52; 3.02±0.72
w2	2.56±0.48; 3.20±0.41
w3	2.29±0.47; 3.11±0.72

Table B.2: The parameters of water molecules and HBs in $[NO_3{\cdot}(H_2O)_3]^-$ at 300 K.

water	R_{OH}	∠HOH	r_{OH}
w1	0.98±0.02	101±4	2.40±0.52, 3.02±0.72
w2	0.98±0.02	101±5	2.56±0.48, 3.20±0.41
w3	0.98±0.02	101±4	2.29±0.47, 3.11±0.72

Table B.3: The structural parameters of $RNO_3(H_2O)_3$ from geometry optimization.

Parameters	$LiNO_3(H_2O)_3$	$NaNO_3(H_2O)_3$	$KNO_3(H_2O)_3$
r_{HB1}	1.67	1.71	1.82
r_{HB2}	1.91	1.78	1.92
r_{HB3}	1.82	1.69	1.94
$r_{R\text{-}O(w1)}$	1.91	2.31	2.70
$r_{R\text{-}O(w2)}$	1.90	2.26	2.70
$r_{R\text{-}O(NO_3^-)}$	1.84	2.29	2.69
∠HOH(w1)	109	106	107
∠HOH(w2)	106	105	105
∠HOH(w3)	108	107	106

Table B.5: The lengths of H-bonds in $[NO_3{\cdot}(H_2O)_3]^-$. The indices of H atoms: H6, H7 in w1; H9, H10 in w2 and H12, H13 in w3.

HBs	$r_a \pm \delta$ (100 K)(Å)	$r_a \pm \delta$ (300 K) (Å)
H6-O2	2.75±0.62	2.40±0.52
H7-O4	2.79±0.58	3.02±0.72
H9-O3	2.89±0.60	2.56±0.48
H10-O4	2.74±0.49	3.20±0.41
H12-O3	2.46±0.45	2.29±0.47
H13-O2	2.75±0.59	3.11±0.72

Table B.4: The parameters of $RNO_3(H_2O)_3$ at 300 K, obtained from the averaging during a DFTMD trajectory. For $RNO_3(H_2O)_3$, R_{OH} and R'_{OH} denote the lengths of O-H bonds in which H atoms is H-bonded and is free, respectively.

Parameters	$LiNO_3(H_2O)_3$	$NaNO_3(H_2O)_3$	$KNO_3(H_2O)_3$
r_{HB1}	1.83 ± 0.14	1.78 ± 0.09	1.82 ± 0.13
r_{HB2}	2.00 ± 0.25	1.91 ± 0.24	1.80 ± 0.12
r_{HB3}	1.79 ± 0.16	1.76 ± 0.11	1.89 ± 0.18
R_{OH}(w1)	0.97 ± 0.01	0.98 ± 0.04	0.97 ± 0.03
R'_{OH}(w1)	1.00 ± 0.02	1.00 ± 0.02	1.00 ± 0.03
R_{OH}(w2)	0.97 ± 0.01	0.98 ± 0.02	0.97 ± 0.02
R'_{OH}(w2)	0.99 ± 0.01	1.00 ± 0.02	1.00 ± 0.03
R_{OH}(w3)	0.97 ± 0.01	0.97 ± 0.02	0.97 ± 0.03
R'_{OH}(w3)	1.00 ± 0.02	1.00 ± 0.02	1.00 ± 0.03
$r_{\text{R-O(w1)}}$	1.95 ± 0.09	2.34 ± 0.08	2.76 ± 0.11
$r_{\text{R-O(w3)}}$	1.92 ± 0.07	2.32 ± 0.11	2.74 ± 0.13
$r_{\text{R-O}(NO_3^-)}$	1.91 ± 0.08	2.31 ± 0.09	2.74 ± 0.12
∠HOH (w1)	107 ± 4	106 ± 4	105 ± 5
∠HOH (w2)	106 ± 6	105 ± 4	106 ± 4
∠HOH (w3)	108 ± 5	106 ± 3	106 ± 3

Structural and Vibrational Properties of $[NO_3{\cdot}(H_2O)_3]^-$ To find the possible source of the different vibrational features of water molecules in the cluster $[NO_3{\cdot}(H_2O)_3]^-$, we considered the structural properties and VDOS for water molecules in this cluster.

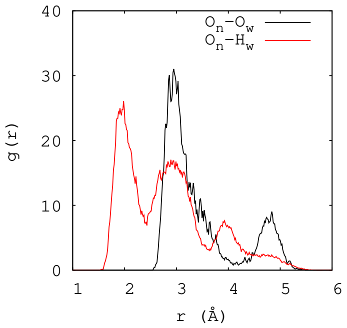

Figure B.1: The nitrate O (O_n)–water O (O_w) and nitrate O–water H (H_w) RDFs for $[NO_3{\cdot}(H_2O)_3]^-$. The peaks for the former are 1.93, 2.95 and 3.95 Å, and for the later are 2.95 and 4.80 Å.

When $T = 300$ K, the difference r_a between different hydrogen atoms in one water molecule is $\Delta r_a = 0.69$ Å, while $\Delta r_a = 0.13$ Å for $T = 100$ K. It shows that the vibrational peaks for the three water molecules are much closer than that at the higher temperature 300 K.

The calculated VDOS for water molecules in the cluster at a lower temperature 100 K is given in Fig. B.2. At the lower temperature, the three water molecules are more symmetric distributed bound to the central nitrate. Therefore, the difference between H-bonds in the symmetric isomer of $[NO_3{\cdot}(H_2O)_3]^-$ is likely a finite temperature effect, which can be verified by the calculation of the VDOS for water molecules.

Both differences $\Delta\nu$ and Δd decrease as the temperature decrease, Therefore, the different vibrational features are temperature-dependent effect.

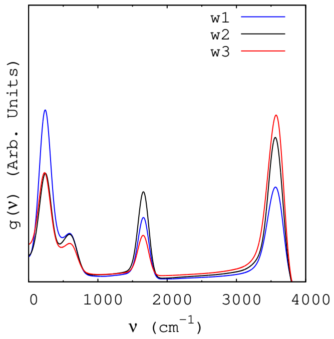

Figure B.2: The VDOS $g(\nu)$ for water molecules in the cluster $[NO_3{\cdot}(H_2O)_3]^-$ at 100 K shows that the vibrational peaks for the three water molecules are very close to each other ($\Delta\nu < 10$ cm^{-1})for both vibrational and bending modes.

In addition, the VDOS for H atoms and water molecules in $[NO_3{\cdot}(H_2O)_3]^-$ (Fig. B.3) shows that H's contribution dominates that of the water molecule.

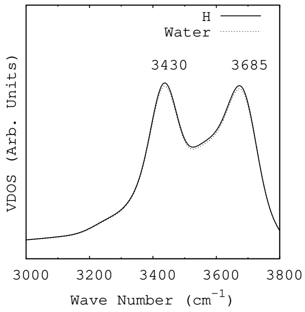

Figure B.3: The comparison between the VDOS for H and of a whole water molecule, for a water molecule (w1, Fig. 4.1a), in $[NO_3{\cdot}(H_2O)_3]^-$ at 300 K.

Appendix C

Propensities of Ions

C.1 Free Energy of the Water Separated and the Contact Ion Pair

From the blue-moon ensemble method[209, 210], we can obtain the constraint force (unit: a.u.force) acting on the atoms. If the distance between the ion pair (unit: Å) is chosen as the reaction coordinate, the formula for calculating the free energy (unit: kcal/mol) is given as follows. The relative free energy is given by

$$F = \sum_{i}^{N} f_i \Delta r,$$

where i denote a point on the one-dimensional reaction coordinate, N is the number of the sampling points of the reaction coordinates, and f_i denotes the average force on atoms over the trajectory when i is fixed. Now we estimate the error of the free energy δF from the summation approximation. It reads

$$\delta F = \frac{1}{N} \sum_{i}^{N} \delta f_i \Delta r. \tag{C.1}$$

Usually, $\delta f_i \approx \delta f$, thus

$$\delta F = \frac{1}{N} \delta f \sum_{i}^{N} \Delta r. \tag{C.2}$$

Particularly, if $\Delta r = 0.2$ Å, $\delta f = 0.0075$ a.u.force, we get

$$\delta F \approx 1.78 \text{ kcal/mol}.$$

C.2 Surface Tension Increment

The surface tension increment $d\gamma/dm_2$ is derived as follows. At constant T and constant p, the Gibbs-Duhem equation is: [135]

$$A d\gamma + n_1^{\sigma} d\mu_1 + n_+^{\sigma} d\mu_+ + n_-^{\sigma} d\mu_- = 0, \tag{C.3}$$

where water is component 1, and the chemical potential for the ionic species $i (i = +, -)$ is defined as

$$\mu_i = \mu_i^0 + RT \ln a_i + z_i F \phi, \tag{C.4}$$

where F is Farady constant, ϕ is the electrical potential of this region (surface or bulk), and z_i is the valence of species i, with ionic activity $a_i = f_i m_i$ in that region, where f_i is the activity coefficient, and m_i is the surface or bulk molality of the ion.

Differentiate Eq. C.3 with respect to m_2, then the surface tension increment is

$$\frac{d\gamma}{dm_2} = -\frac{1}{m_1^*}\frac{n_1^\sigma}{A}[(m_+^\sigma - m_+^b)\frac{d\mu_+}{dm_2} + (m_-^\sigma - m_-^b)\frac{d\mu_-}{dm_2}], \tag{C.5}$$

where m_1^* is the solvent molality.

For species i, distribution coefficient $K_{p,i}$, is defined as

$$K_{p,i} = \frac{m_i^\sigma}{m_i^b} \approx \frac{m_i^\sigma}{\nu_i m_2}. \tag{C.6}$$

$$\frac{d\mu_\pm}{dm_2} = \frac{RT}{m_2}(1+\epsilon_\pm^b) + z_\pm F\frac{d\phi^b}{dm_2} \approx \frac{RT}{m_2}(1+\epsilon_\pm^b), \tag{C.7}$$

where $\epsilon_\pm^b = d(\ln f_\pm^b)/d(\ln m_2)$.

The ion partition coefficients $K_{p,2}$ is defined:

$$\nu K_{p,2} = \nu_+ K_{p,+} + \nu_- K_{p,-}, \tag{C.8}$$

where ν_i is ions' stoichiometry.

In general, from Eq. C.5, Eq. C.6 and Eq. C.7, for solutions at sufficient low electrolyte concentrations, the surface tension increment is

$$\begin{aligned}\frac{d\gamma}{dm_2} &= -\frac{1}{m_1^*}\frac{n_1^\sigma}{A}\sum_{i=\pm}(m_i^\sigma - m_i^b)\frac{d\mu_i}{dm_2} \\ &= -\frac{RT\nu}{m_1^*}\frac{n_1^\sigma}{A}\sum_{i=\pm}\frac{\nu_i(K_{p,i}-1)(1+\epsilon_i^b)}{\nu} \\ &= -\frac{RT\nu}{m_1^*}\frac{n_1^\sigma}{A}[(K_{p,2}-1) + \sum_{i=\pm}\frac{(K_{p,i}-1)\nu_i\epsilon_i^b}{\nu}]\end{aligned} \tag{C.9}$$

Under the condition $\epsilon_\pm^b << 1$ or $\epsilon_+^b \approx \epsilon_-^b$ the surface tension increment is

$$\frac{d\gamma}{dm_2} = -\frac{RT\nu}{m_1^*}\frac{n_1^\sigma}{A}(1+\epsilon_i^b)^0[\frac{\nu_+ K_{p,+} + \nu_- K_{p,-}}{\nu} - 1]. \tag{C.10}$$

The approximations in Eq. C.10 regarding the self-interaction nonideality terms ϵ for the salt component, for the single ions, and as a geometric mean of the single ion terms, are given in Ref.[135]. Typically the mean ionic version of ϵ is of order ~ 0.1, so smaller in magnitude than 1. (Thomas Record) Here, *nonideality* means the activity coefficient f_i is not much smaller than 1.

C.3 Gibbs surface excess

Gibbs isotherm The Gibbs adsorption isotherm for multicomponent systems is an equation used to relate the changes in concentration of a component in contact with a surface with changes in the surface tension. For a binary system containing two components, the Gibbs adsorption equation (*adsorption isotherm*) in terms of surface excess is:

$$-\mathrm{d}\gamma = \Gamma_1 \mathrm{d}\mu_1 + \Gamma_2 \mathrm{d}\mu_2 \tag{C.11}$$

where γ is the surface tension, Γ_i is the surface excess of component i, μ_i is the chemical potential of component i.

Remark 1: For a general chemical equilibrium

$$\alpha A + \beta B \cdots \rightleftharpoons \rho R + \sigma S \cdots \tag{C.12}$$

the thermodynamic equilibrium constant can be defined such that, at equilibrium,

$$K^{\ominus} = \frac{\{R\}^{\rho}\{S\}^{\sigma}\cdots}{\{A\}^{\alpha}\{B\}^{\beta}\cdots} \tag{C.13}$$

where curly brackets denote the thermodynamic activities of the chemical species and $\{R\}^i = \{R\}\cdot\{R\}\cdot\cdots$. This expression can be derived by considering the Gibbs free energy change for the reaction. If deviations from ideal behavior are neglected, the activities may be replaced by concentrations, [A](or m_{A}), and a concentration quotient

$$K_{\mathrm{c}} = \frac{[R]^{\rho}[S]^{\sigma}\cdots}{[A]^{\alpha}[B]^{\beta}\cdots}. \tag{C.14}$$

But K_{c} is a little different quantity which describe the *distribution* of products and reactants in a chemical reaction, neglecting distribution of different products or different reactants.

Remark 2: The thermodynamic activities of a chemical species is a more general concept than the concept of concentration:

$$a_i = f_i m_i. \tag{C.15}$$

Remark 3: Notice that $f(x) = \ln x$ is a monotonically increasing function, thus $\epsilon_i^b = \mathrm{d}\ln f_i^b/\mathrm{d}\ln m_2$ describe the same thing as $\mathrm{d}f_i^b/\mathrm{d}m_2$, i.e., the dependence of the activity coefficient on the concentration for the chemical species i. However, using $\ln f_i^b$ and $\ln m_2$ is more convenient.

Different influences at the interface may cause changes in the composition of the near-surface layer. Substances may either accumulate near the surface or, conversely, move into the bulk. The movement of the molecules characterizes the phenomena of adsorption. Adsorption influences changes in surface tension and colloid stability. Adsorption layers at the surface of a liquid dispersion medium may affect the interactions of the dispersed particles in the media and consequently these layers may play crucial role in colloid stability The adsorption of molecules of liquid phase at an interface occurs when this liquid phase is in contact with other immiscible phases that may be gas, liquid, or solid.

Surface tension describes how difficult it is to extend the area of a surface (by stretching or distorting it). If surface tension is high, there is a large free energy required to increase the surface area, so the surface will tend to contract and hold together like a rubber sheet. There are various factors affecting surface tension, one of which is that the composition of the surface may be different from the bulk. For example, if water is mixed with a tiny amount of surfactants (eg., hand soap, or $C_{17}H_{35}COONa$), the bulk water may be 99% water molecules and 1% soap molecules, but the topmost surface of the water may be 50% water molecules and 50% soap molecules.($C_{17}H_{35}COONa$ is floating on the surface.) In this case, the soap has a large and positive surface excess. In other examples, the surface excess may be negative. For example, if water is mixed with an inorganic salt like sodium chloride, the surface of the water is on average less salty and more pure than the bulk average.

Consider again the example of water with a bit of soap. Since the water surface needs to have higher concentration of soap than the bulk, whenever the water's surface area is increased, it is necessary to remove soap molecules from the bulk and add them to the new surface. If the concentration of soap is increased a bit, the soap molecules are more readily available (they have higher chemical potential), so it is easier to pull them from the bulk in order to create the new surface. Since it is easier to create new surface, the surface tension is lowered. The general principle is: When the surface excess of a component is *positive*, *increasing* the chemical potential of that component *reduces* the surface tension:

$$\frac{\mathrm{d}\gamma}{\mathrm{d}\mu_i} < 0, (\Gamma_i > 0). \tag{C.16}$$

Next consider the example of water with salt. The water surface is less salty than bulk, so whenever the water's surface area is increased, it is necessary to remove ions from the new surface and push them into bulk. If the concentration of salt is increased a bit (raising the salt's chemical potential), it becomes harder to push away the ions. Since it is now harder to create the new surface, the surface tension is higher. The general principle is: When the surface excess of a component is negative, increasing the chemical potential of that component increases the surface tension

$$\frac{\mathrm{d}\gamma}{\mathrm{d}\mu_i} > 0, (\Gamma_i < 0). \tag{C.17}$$

The Gibbs isotherm equation gives the exact quantitative relationship for these trends.

In the presence of two phases (α and β, the surface (surface phase) is located in between the phase α and phase β. Experimentally, it is difficult to determine the exact structure of an inhomogeneous surface phase that is in contact with a bulk liquid phase containing more than one solute. Inhomogeneity of the surface phase is a result of variation of mole ratios. A model proposed by Josiah W. Gibbs proposed that the surface phase as an idealized model that had zero thickness. In reality, although the bulk regions of α and β phases are constant, the concentrations of components in the interfacial region will gradually vary from the bulk concentration of α to the bulk concentration of β over the distance x. This is in contrast to the idealized Gibbs model where the distance x takes on the value of zero.

Definition of surface excess In the idealized model, the chemical components of the α and β bulk phases remain unchanged except when approaching the dividing surface. The total moles of any component (examples include water, ethylene glycol, etc.) remains constant in the bulk phases but varies in the surface phase for the real system model.

In the real system, however, the total moles of a component varies depending on the arbitrary placement of the dividing surface. The quantitative measure of adsorption of the i-th component is captured by the surface excess quantity. The surface excess represents the difference between the total moles of the i-th component in a system and the moles of the i-th component in a particular phase (either α and β) and is represented by:

$$\Gamma_i = \frac{{n_i}^{\mathrm{TOTAL}} - {n_i}^{\alpha} - {n_i}^{\beta}}{A}, \tag{C.18}$$

where Γ_i is the surface excess of the i-th component, n are the moles, α and β are the phases, and A is the area of the dividing surface. Γ represents excess of solute per unit area of the surface over what would be present if the bulk concentration prevailed all the way to the surface, it can be positive, negative or zero. It has units of mol/m^2.

The chemical potential of species i in solution depends on the activity a using the following equation:[211]

$$\mu_i = {\mu_i}^o + RT \ln a_i, \tag{C.19}$$

where μ_i is the chemical potential of the i-th component, μ_i^o is the chemical potential of the i-th component at a reference state, $R = 8.3144\text{J/mol}\cdot\text{K}$ is the gas constant, T is the temperature, and a_i is the activity of the i-th component. Differentiation of the chemical potential equation results in:

$$\mathrm{d}\mu_i = RT\frac{\mathrm{d}a_i}{a_i} = RT\mathrm{d}\ln f m_i \tag{C.20}$$

where f is the activity coefficient of component i, and m_i is the concentration of species i in the bulk phase.

If the solutions in the α and β phases are dilute (rich in one particular component i) then activity coefficient of the component i approaches unity and the Gibbs isotherm becomes:

$$\Gamma_i = -\frac{1}{RT}\left(\frac{\partial\gamma}{\partial \ln m_i}\right)_{T,p}. \tag{C.21}$$

In the derivation of the equation it is assumed that the solution is ideal, (so $\mu = \mu^o + RT\ln m$) and surface concentration of the solvent is zero, so it is only valid under these assumptions.

a_i changes too fast, so we borrow $\ln a_i$ to describe a solution system. In an ideal solution, we just borrow $\ln m$ to describe the system, since $\mu = \mu^o + RT\ln m$. But in the nonideal case, $\mu = \mu^o + RT\ln f_i m_i$, more "symmetry-breaking" exists, thus we have to use a more sophisticated quantity $\ln f_i m_i$ to do so.

measurement The most direct way of measuring an activity of a species is to measure its partial vapor pressure in equilibrium with a number of solutions of different strength. For some solutes this is not practical, say sucrose or salt (NaCl) do not have a measurable vapor pressure at ordinary temperatures. However, in such cases it is possible to measure the vapor pressure of the solvent instead. Using the Gibbs-Duhem relation it is possible to translate the change in solvent vapor pressures with concentration into activities for the solute.

Another way to determine the activity of a species is through the manipulation of colligative properties, specifically freezing point depression. Using freezing point depression techniques, it is possible to calculate the activity of a weak acid from the relation, $m' = m(1 + a)$, where m' is the total molal equilibrium concentration of solute determined by any colligative property measurement (in this case ΔT_{fus}, b is the nominal molality obtained from titration and a is the activity of the species.

There are also electrochemical methods that allow the determination of activity and its coefficient. The value of the mean ionic activity coefficient of ions in solution can also be estimated with the Debye-Duekel equation, the Davies equation or the Pitzer equations.

Appendix D

Thickness of the Interface of the Aqueous Solutions

To determine the thickness of the water/vapor interface of alkali solutions, we chose several different thickness values of slab of the interface and calculate the corresponding susceptibility for these slabs, respectively. Take the water/vapor interface of $LiNO_3$ solution as an example. We chose seven different thickness values—from 2 to 8 Å, and calculate VSFG intensities $I_{SSP} \propto |\chi^{(2),\mathrm{R}}_{SSP}|^2$ for the water/vapor interface with a thickness of each of these values. The result is given in Fig. D.1 a and b. It shows that $|\chi^{(2),\mathrm{R}}_{SSP}|^2$ converges as the thickness increases to 8 Å.

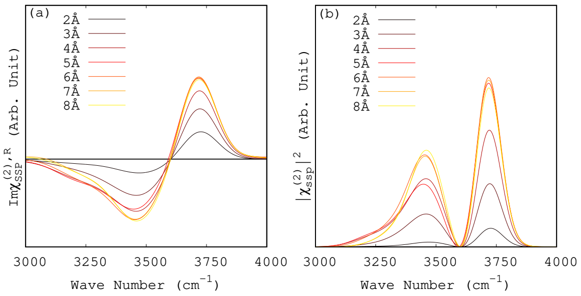

Figure D.1: The calculated $|\chi^{(2),\mathrm{R}}_{SSP}|^2$, of water molecules at the aqueous/vapor interfaces with different thickness. This calculation is done for a model for the water/vapor interface where a slab of 117 water molecules containing one Li^+ and one NO_3^- is included in a period simulation box of 15.60 Å ×15.60 Å ×31.00 Å at 300 K.

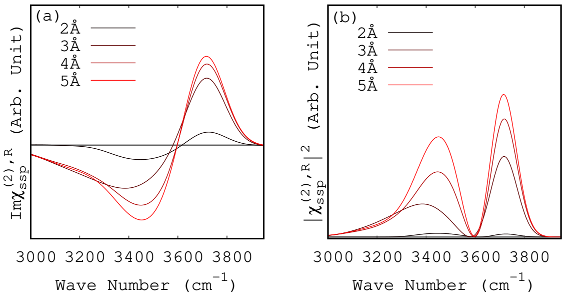

Figure D.2: The calculated $|\chi^{(2),R}_{SSP}|^2$, of water molecules at water/-vapor interfaces with different thickness. This calculation is done for a model for water/vapor interface where a slab of 118 water molecules containing one Li^+ and one I^- is included in a period simulation box of 15.60 Å × 15.60 Å × 31.00 Å.

Because of the limitation of the box scale, we chose 4 different thickness values—$d = 2, 3, 4, 5$ Å, for checking. The VSFG intensities $I_{SSP} \propto |\chi^{(2),R}_{SSP}|^2$ for the water/vapor interface of the LiI solution are given in Fig. D.2 a and b. The results show that $|\chi^{(2),R}_{SSP}|^2$ increases as the thickness increase from 2 Å to 5 Å.

The thickness of the water/vapor interface of solutions can also be seen from the calculated RDF. For example, the RDFs of interface of the NaI solution is shown in Fig. D.3. It indicates that the thickness of the water/vapor interface is ∼ 8 Å.

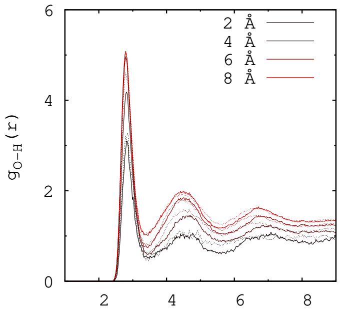

FIGURE D.3: The RDF $g_{\mathrm{OH}}(r)$ in the NaI solution/vapor interface. The simulation system includes one Na$^+$ ion, one I$^-$ ion, and 124 water molecules in 15.60 Å × 15.60 Å × 31.00 Å simulation box. The solid and dashed lines are corresponding to one of the two interfaces in our simulation, respectively. The simulation time is 22.5 ps.

Furthermore, we also estimated the thickness of a water/vapor interface by calculating the HB dynamics for it. Fig. D.4 shows the dependence of the logarithm of survival probability on the thickness of the water/vapor interface of the LiI solution. We see that when $d = 8$ Å the $\ln S_{\mathrm{HB}}$ of the interface does not change as the thickness increases, indicating the thickness of the interface.

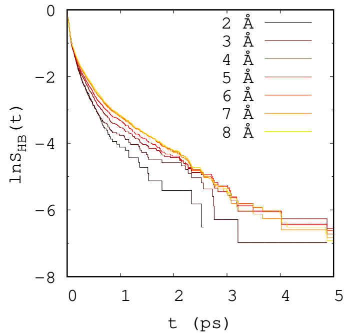

FIGURE D.4: The logarithms of the function $S_{\mathrm{HB}}(t)$ for water-water H-bonds at interfaces with different thickness in 0.9 M LiI solution.

In addition, the survival probability $S_{\mathrm{HB}}(t)$ is dependent on the temporal resolution t_t, which is the time interval between two adjacent states in time used to calculate the survival probability. As an example, the t_t dependence of the τ_{HB} of the three alkali-iodine solution interfaces in our AIMD simulations is reported in Fig. D.5. It shows that, if we take the t_t as small as possible, the number of times that H-bonds break and form again in this period of time (t_t) will be reduced. Thus, we can obtain the continuum HB lifetime independent of the t_t. As shown in Fig. D.5, the value of τ_{HB} corresponding to the intersections of the $\tau_{\mathrm{HB}}(t_t)$ functions and the line $t_t = 5$ fs approximately give the continuum HB lifetimes.

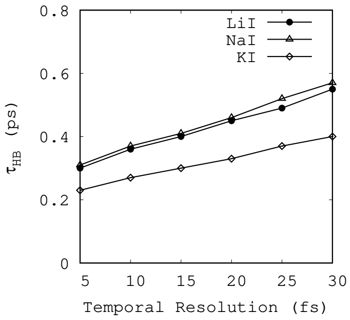

FIGURE D.5: The resolution dependence of the continuum lifetime τ_{HB} of water–water H-bonds at interfaces of different 0.9 M alkali-iodine solutions at 330 K, calculated for six temporal resolutions (t_t). [212–214] For $t_t = 5$ fs, the calculated continuum HB lifetime is 0.30 ps, 0.31 ps and 0.23 ps, for the interface of LiI, NaI and KI solution, respectively.

Appendix E

HB Lifetime Distributions and Instantaneous Interfaces

E.1 Relations between HB Lifetime Distributions

Different HB lifetime Distributions From the probability $P_{tc}(t)$ of the total HB lifetime in a configuration, and the probability P_a of the first HB breaking in time t after it have been detected at the moment t, one can introduce the average time $\langle\tau_{tc}\rangle$ and $\langle\tau_a\rangle$:

$$\langle\tau_{tc}\rangle = \int_0^\infty tP_{tc}(t)dt, \tag{E.1}$$

$$\langle\tau_a\rangle = \int_0^\infty tP_a(t)dt. \tag{E.2}$$

Since $P_{\mathrm{a}}(t) = \int_t^\infty P_{\mathrm{tc}}(\tau)\frac{d\tau}{\tau}$, i.e.,

$$P_{tc}(t) = -t\frac{dP_a(t)}{dt},$$

integrating by parts, we obtain

$$\begin{aligned}\langle\tau_{tc}\rangle &= -\int_0^\infty t^2\frac{dP_a(t)}{dt}dt\\ &= -\int_0^\infty t^2 dP_a(t) = -[-2\langle\tau_a\rangle + 0]\\ &= 2\langle\tau_a\rangle,\end{aligned}$$

in which we used $\int_0^\infty d(t^2P_a) = 0$. Therefore, there is a relationship between $\langle\tau_{tc}\rangle$ and $\langle\tau_a\rangle$:

$$\langle\tau_{tc}\rangle = 2\langle\tau_a\rangle. \tag{E.3}$$

We denote the probability of the total HB lifetime along a trajectory as $P_{\mathrm{tt}}(t)$, then the average HB lifetime over the trajectory is

$$\langle\tau_{\mathrm{tt}}\rangle = \int_0^\infty tP_{\mathrm{tt}}(t)dt. \tag{E.4}$$

Because $\int_0^\infty P_{\mathrm{tc}}(t)dt = \frac{1}{\langle\tau_{tt}\rangle}\int_0^\infty tP_{\mathrm{tt}}(t)dt = 1$, we get

$$P_{\mathrm{tt}}(t) = \langle\tau_{\mathrm{tt}}\rangle\, P_{\mathrm{tc}}(t)/t. \tag{E.5}$$

The difference between the two distribution functions, $P_{\mathrm{tt}}(t)$ and $P_{\mathrm{tc}}(t)$, can be described as follows. The $P_{\mathrm{tt}}(t)$ represents the percentage of pairs of molecules that had a continuous H-bonds during time t, while the $P_{\mathrm{tc}}(t)$ the percentage of the number of H-bonds with a given lifetime t to the number of all H-bonds in any configuration. [191]

Since $P_{\mathrm{a}}(t) = \int_t^\infty P_{\mathrm{tc}}(\tau)\frac{d\tau}{\tau}$, we can obtain

$$\begin{aligned} P_{\mathrm{a}}(t) &= \int_t^\infty \frac{P_{tt}}{\langle \tau_{tt} \rangle} \frac{\tau}{\tau} d\tau \\ &= \int_t^\infty \frac{P_{tt}}{\langle \tau_{tt} \rangle} d\tau. \end{aligned}$$

Let $t = 0$, we obtain

$$P_{\mathrm{a}}(0) = 1/\left\langle t_{\mathrm{tt}} \right\rangle = 1/\left\langle t_{\mathrm{HB}} \right\rangle. \tag{E.6}$$

From Eq. E.1 and the relation between $S_{\mathrm{HB}}(t)$ and $P_{\mathrm{a}}(t)$

$$S_{\mathrm{HB}}(t) = \int_t^\infty P_{\mathrm{a}}(\tau) d\tau, \tag{E.7}$$

we can obtain

$$\begin{aligned} &\int_0^\infty \int_t^\infty P_a(t) d\tau dt = \int_0^\infty \int_0^\tau P_a(\tau) dt d\tau \\ &= \int_0^\infty \tau P_a(\tau) d\tau \\ &= \langle \tau_{\mathrm{a}} \rangle, \end{aligned}$$

i.e.,

$$\int_0^\infty S_{\mathrm{HB}}(t) dt = \langle \tau_{\mathrm{a}} \rangle. \tag{E.8}$$

Calculation of HB lifetime distributions In this paragraph, we describe the method to calculate the above lifetime distributions $P_{tc}(\tau)$, $P_a(\tau)$, and $P_{tt}(\tau)$.

First, we describe the method of calculating $P_{tc}(\tau)$. Theoretically speaking, in order to calculate $P_{tc}(\tau)$, our detection time t must meet the following conditions: $t - t_0 > \tau_{hb}^{\max}$, where t_0 is the initial time and $\tau_{hb}^{\max}$ is the maximum lifetime value of the H-bonds in the system. However, the value of τ_{hb} cannot be known in advance. In order to reduce the error, the method we can adopt is to set an empirical value as large as possible for $\tau_{hb}^{\max}$ if conditions permit. Since the value of $\tau_{hb}^{\max}$ is limited, in principle the lifetime value of the HB can always be greater than $\tau_{hb}^{\max}$. Therefore, the average value of the HB lifetime distribution calculated in this approximate way will move to a shorter lifetime than the average value of the true HB lifetime distribution:

$$\int_0^\infty \tau P_{\mathrm{tc}}^{\mathrm{approx}}(\tau) d\tau < \left\langle \tau_{\mathrm{tc}} \right\rangle. \tag{E.9}$$

Among the hydrogen bonds detected at time t, if there are some H-bonds that have existed at the beginning t_0 and remain in existence until time t, then we can approximately express the lifetime of these H-bonds as $\delta t^{(j)} = t^{(j)} - t_0$, where $j = 1, \cdots, m$ is the labels of the m H-bonds and $t^{(j)}$ is the moment when the j-th HB is broken. If we use $\tau^{(j)}, j = 1, \cdots, m$ to represent the true lifetimes of these m H-bonds, then we can find that $\tau^{(j)} - \delta t^{(j)} > 0$. Since we cannot judge the true lifetime of these m hydrogen bonds, we can use $\delta t^{(j)}$ to approximate the lifetime of these m

H-bonds, that is

$$\tau^{(j)} = \delta t^{(j)}. \tag{E.10}$$

For those H-bonds that did not exist at the beginning, the method of calculating their lifetime is very straightforward, the lifetime $\tau^{(j)}$ is equal to the time $t^{(j)}$ when the HB is broken minus the moment $t_0^{(j)}$ of its formation:

$$\tau^{(j)} = t^{(j)} - t_0^{(j)}, \tag{E.11}$$

where the superscript $j = 1, \cdots, m'$, identifies m' H-bonds detected at time t, and formed after t_0 and broken at $t^{(j)}$.

Specifically, for the AIMD simulation results we obtained, we also approximate P_{tc} as follows: We select evenly distributed n time points $t = t_1, ..., t_n$, from the trajectory obtained by the simulation, and count the HB lifetimes at each time point t_i. The distribution function $P_{tc}(\tau)$ can be obtained by the average of the lifetime distribution detected at a certain time t_i, $i = 1, \cdots, n$, where $t_i - t_{i-1} = \tau_{hb}^{\max}$.

If only from the perspective of simulation data, we have another way to obtain $P_{tc}(\tau)$: Count the lifetimes of H-bonds that are formed after the initial time t_0 and are broken before the end time t_f. Although the distribution obtained in this method cannot be verified experimentally, it is the true distribution of HB bonds in simulated systems.

Calculation of the Reactive Flux For dynamical variables $x_i(t)$ and $x_k(t)$, their correlation functions have the following relationship:[215]

$$\langle x_i(t') x_k(t) \rangle = -\langle x_i(t) x_k(t') \rangle, \tag{E.12}$$

or

$$\phi_{ik}(t) = -\phi_{ki}(t).$$

Let $x_i = h$, $x_k = \dot{h}$, then, we obtain

$$\langle h(0) \dot{h}(t) \rangle = -\langle \dot{h}(0) h(t) \rangle. \tag{E.13}$$

From the definition of the reactive flux $k(t) = -dc/dt$, we obtain

$$k(t) = -\langle h(0) \dot{h}(t) \rangle / \langle h \rangle. \tag{E.14}$$

Then from Eq. E.13, we get

$$k(t) = \langle \dot{h}(0) h(t) \rangle / \langle h \rangle.$$

Since $\langle \dot{h}(0) \rangle = 0$, $k(t)$ can be calculated by

$$k(t) = -\langle \dot{h}(0) [1 - h(t)] \rangle / \langle h \rangle. \tag{E.15}$$

Relaxation Time of Hydrogen Bonds in Bulk Water In addition to the simulation in the main text of this thesis, we also use different methods for the bulk water system with the same temperature, volume and number of molecules. The number of water molecules in the system is 128, the temperature is still $T = 300$ K, and the box is a cube with a side length of 15.6404 Å. In this simulation, we relax the value of the target accuracy for the SCF convergence to 10^{-6}. Other settings, such as exchange correlation functional, correction of dispersion force, etc. are the same as the text. For the dynamic trajectory of such a system, we also calculated the self-correlation function $c(t)$ of the HB population operator, and the functions $k(t)$ and $n(t)$ derived from it. Table E.1 and E.2 shows the rate constant k, k' and the relaxation time τ_{HB} obtained by the least squares fit method. It can be seen from the tables that the accuracy of the calculation of k, k' are accurate to at least two decimal places.

TABLE E.1: The k and k' for the bulk water. We carried on the short time region 0.2 ps $< t <$ 2 ps. The unit for k (k') is ps^{-1}, and that for τ_{HB} ($= 1/k$) is ps. The $h(t)$ is bond-based.

Criterion	k (bulk)	k' (bulk)	τ_{HB} (bulk)
ADH	0.3346	0.9374	2.9884
ADH(from k_{in})	0.2988	1.0290	3.3467
AHD	0.3224	1.0059	3.1014
AHD(from k_{in})	0.2884	1.1210	3.4679

TABLE E.2: The k and k' for the bulk water. We carried on the long time region 2 ps $< t <$ 12 ps. The unit for k (k') is ps^{-1}, and that for τ_{HB} ($= 1/k$) is ps. The $h(t)$ is bond-based.

Criterion	k (bulk)	k' (bulk)	τ_{HB} (bulk)
ADH	0.1032	0.0237	9.6901
ADH(from k_{in})	0.1028	0.0275	9.7283
AHD	0.1036	0.0339	9.6558
AHD(from k_{in})	0.1031	0.0401	9.7016

Different Definitions of the $h(t)$ The correlation functions $C_{HB}(t)$ of water molecules in bulk water is shown in Fig. E.1. It shows that there are big differences in the correlation function $C_{HB}(t)$ of the two definitions of $h(t)$, because hydrogen exchange is considered in the O–H pair-based definition of $h(t)$, but not in the water–water pair-based definition.

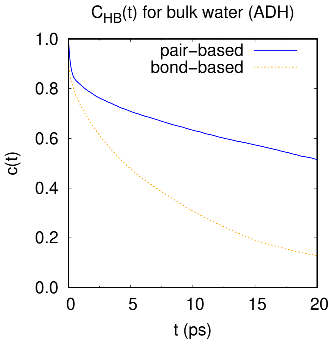

FIGURE E.1: The correlation functions $C_{HB}(t)$ of water molecules in bulk water. Here $h(t)$ is based on two different definitions, one is based on a pair of water molecules (solid line), and the other is based on O–H pairs between water molecules (dashed line).

E.2 Dynamics of Interfacial Hydrogen Bonds

Instantaneous Surfaces Let us consider the interfacial system of pure water. At a certain time t, the instantaneous surface $\mathbf{s}^0(x(t), y(t))$ can be determined by calculating the coarse-graining density field: we can specify that the coarse-grained density is the reference density $\rho_{\text{ref}} = 0.016$ Å^{-3}, and those grid points constitute the surface $\mathbf{s}^0(x, y)$ of pure water. In our simulated pure water system, there are two such surfaces. The code for calculating the instantaneous surfaces of interfacial systems can be found on `https://github.com/hg08/interface`.

Griding and Layering Wee assume that the normal is along the z-axis direction. First, we need to discretize the coordinates of the xy plane. We divide the edges along the x-axis direction and the edges along the y-axis direction of the simulated box into N parts uniformly, and the xy plane can be approximated by $N \times N$ discrete points. Then $N \times N$ ordinates of the surface $\mathbf{s}^0(x(t_0), y(t_0))$ at the initial time t_0 can be represented as components of an $N \times N$-vector $\mathbf{z}^0(t_0)$. The surface $\mathbf{s}^0(x(t_0), y(t_0))$ is also the upper boundary of the interface. Secondly, we define a layering strategy, or define the thickness d of the interface layer. In this way, we then determine the lower boundary $\mathbf{s}^1(x(t_0), y(t_0))$ of the interface. It can be expressed as a $N \times N$-vector $\mathbf{z}^1(t_0) = \mathbf{z}^0(t_0) - \mathbf{d}$, and $\mathbf{d}$ is a $N \times N$-dimensional constant vector in which all the entries are d. The superscripts 0 and 1 respectively identify the upper and lower boundaries of the interface. Similarly, the other interface can also be determined.

So far, our interfaces are still static, because we only considered the initial moment. But the interfaces defined here can be defined for different moments naturally. Therefore, according to the same method, for the molecular motion trajectory of an interface system, we can obtain the dynamically changing interface layer, i.e., $\mathbf{z}^1(t) = \mathbf{z}^0(t) - \mathbf{d}$. When the interfaces are determined, we can answer the question: For an atom with coordinates (x, y, z) at any time t, whether it is in the interface? To answer this question, we need to map the atom's coordinates (x, y) to an ordered integer pair (i, j), $i, j \in \{0, \cdots, N\}$, where $i = \text{int}(x/\Delta x), j = \text{int}(y/\Delta y)$, $\Delta x = a/N$, and $\Delta y = b/N$.

At a certain time t, the ordinate z of an atom can be approximately represented as a function defined on point (i, j), $z = z(i, j)$. Then we compare $z(i, j)$ and $z^l_{i,j}$, $l = 0, 1$ to determine if the atom is in the interface. That is, if $z^0_{i,j}(t) < z(i, j) < z^1_{ij}(t)$, then we know that at time t, the atom at (x, y, z) is located in the interface.

Selcetion of Water Molecules from Instantaneous Interface The first method to extract the interfacial molecules is as follows. 1) Determine the instananeous surface of a system; 2) Define a interface system with a fixed thickness below the instantaneous surface; 3) Select the atoms which are near the instananeous surface; 4) Calculate the HB dynamics for molecules in interface at different time t. Given the thickness of layer d, at any time t_0, t_1, t_2, $\cdots$, t_n, the set of molecules in the interface can be determined. Since the molecules are always in motion, generally, the set $S^0(t_i)$ of the molecules in the interface at time t_i and the set $S^0(t_j)$ of the molecules in the interface at a different time t_j is different. Therefore, to calculate the HB dynamics of molecules in the interface, we need to calculate the correlation functions of the HB population $h(t)$ of the molecules in the interface at different times, and average the correlation functions obtained at all times.

Interfacial Hydrogen Bond Population Operator $h^s(t)$ The second method to extract the interfacial molecules is as follows. 1) Determine the instananeous surface of a system; 2) Define a interface system with a fixed thickness below the instantaneous surface; 3) Define the interfacial hydrogen bond population operator $h^s(t)$. 4) Calculate the autocorrelation function of $h^s(t)$ and then the related observations.

If we want to calculate only the dynamic characteristics of molecules located in the interface, the above statistical method will have a error in select correct molecules in interface. In chapter 6, we had combined the recognition technology of the instantaneous liquid interfaces [204] with the definition of H-bonds [166, 199] to define H-bonds that depend on the environment. With this method, we can have more understanding of the differences and commonalities in the kinetics of the breaking and reconstruction of the hydrogen bonds of the water molecules in the interface system. At the same time, we can compare the HB dynamcis in the interface of different thicknesses with the HB dynamics in bulk water to obtain the thickness of the interface from the perspective of HB dynamics. In addition, for the interface system of different solutions, we can also use the layering technique to study the HB dynamics, so that we can understand the particularity of the interface of various solutions relative to pure water.

In fact, none of the above-mentioned two methods for obtaining the HB dynamics of the interface water molecules can give the true interface HB dynamics completely and accurately. But they respectively give an extreme case of interface HB dynamics. In the first method, the formation and breaking of intermolecular H-bonds can be truly described, but the selection of interface water molecules is not accurate enough. Since the configuration of the molecule will change over time, the contribution of the H-bonds in the bulk phase will be included. In the second method, we are very accurate in choosing the interface water molecules and the H-bonds in the interface, but we may artificially destroy some H-bonds in the interface that were not broken. To a certain extent, the HB dynamics obtained by the second method is *accelerated*. Therefore, the comparison of the results obtained by these two methods may give a true picture of the interface HB dynamics.

The code for calculating the HB dynamics for instantaneous interfaces can be found on `https://github.com/hg08/hb_in_interface`.

Bibliography

[1] S. Yamamoto et al. “In Situ X-ray Photoelectron Spectroscopy Studies of Water on Metals and Oxides at Ambient Conditions”. In: *J. Phys.: Condens. Matter* 20.18 (2008), p. 184025. DOI: https://doi.org/10.1088/0953-8984/20/18/184025. URL: https://iopscience.iop.org/article/10.1088/0953-8984/20/18/184025/meta.

[2] M. Salmeron et al. “Water Growth on Metals and Oxides: Binding, Dissociation and Role of Hydroxyl Groups”. In: *Faraday Discuss.* 141 (0 2009), pp. 221–229. DOI: 10.1039/B806516K. URL: http://dx.doi.org/10.1039/B806516K.

[3] J. Balajka et al. “High-Affinity Adsorption Leads to Molecularly Ordered Interfaces on TiO_2 in Air and Solution”. In: *Science* 361 (2018), pp. 786–789. DOI: 10.1126/science.aat6752. URL: https://science.sciencemag.org/content/361/6404/786.

[4] D. J. Tobias. “A Workshop on MD Simulations”. In: *NATO Sci. Ser., Ser. A* 305 (1999), pp. 293–310.

[5] A. V. Benderskii and K. B. Eisenthal. “Effect of Organic Surfactant on Femtosecond Solvation Dynamics at the Air-water Interface”. In: *J. Phys. Chem. B* 104 (2000), pp. 11723–11728. DOI: 10.1021/jp0025429. URL: https://pubs.acs.org/doi/abs/10.1021/jp0025429.

[6] A. V. Benderskii and K. B. Eisenthal. “Dynamical Time Scales of Aqueous Solvation at Negatively Charged Lipid/Water Interfaces”. In: *J. Phys. Chem. A* 106 (2002), pp. 7482–7490. DOI: 10.1021/jp0120155. URL: https://pubs.acs.org/doi/abs/10.1021/jp0120155.

[7] P. Ball. “Water as an Active Constituent in Cell Biology”. In: *Chem. Rev.* 108 (2008), pp. 74–108. DOI: 10.1021/cr068037a. URL: https://pubs.acs.org/doi/abs/10.1021/cr068037a.

[8] I.-F. W. Kuo and C. J. Mundy. “An Ab Initio Molecular Dynamics Study of the Aqueous Liquid-Vapor Interface”. In: *Science* 303 (2004), p. 658. DOI: 10.1126/science.1092787. URL: https://science.sciencemag.org/content/303/5658/658.

[9] L. Y. Zhang et al. “Protein Hydration Dynamics and Molecular Mechanism of Coupled Water-Protein Fluctuations”. In: *J. Am. Chem. Soc.* 131 (2009), pp. 10677–10691. DOI: 10.1021/ja902918p. URL: https://pubs.acs.org/doi/pdf/10.1021/ja902918p.

[10] P. Lo Nostro and B. W. Ninham. “ Hofmeister Phenomena: An Update on Ion Specificity in Biology”. In: *Chem. Rev.* 112 (2012), p. 2286.

[11] G. L. Richmond. “Molecular Bonding and Interactions at Aqueous Surfaces as Probed by Vibrational Sum Frequency Spectroscopy”. In: *Chem. Rev.* 102 (2002), pp. 2693–2724. DOI: 10.1021/cr0006876. URL: https://doi.org/10.1021/cr0006876.

[12] H. Liu and B. E. Logan. “Electricity Generation Using an Air-Cathode Single Chamber Microbial Fuel Cell in the Presence and Absence of a Proton Exchange Membrane”. In: *Environ. Sci. Technol.* 38 (2004), p. 4040. DOI: `10.1021/es0499344`. URL: `https://pubs.acs.org/doi/abs/10.1021/es0499344`.

[13] R. Asahi et al. “Visible-Light Photocatalysis in Nitrogen-Doped Titanium Oxides”. In: *Science* 293 (2001), pp. 269–271. DOI: `10.1126/science.1061051`. URL: `https://science.sciencemag.org/content/293/5528/269.abstract`.

[14] C. Tian et al. “Interfacial Structures of Acidic and Basic Aqueous Solutions”. In: *J. Am. Chem. Soc.* 130.39 (2008), pp. 13033–13039. DOI: `10.1021/ja8021297`. eprint: `http://dx.doi.org/10.1021/ja8021297`. URL: `http://dx.doi.org/10.1021/ja8021297`.

[15] J. G. Irwin and M. L. Williams. “Acid Rain: Chemistry and Transport”. In: *EnViron. Pollut.* 50 (1988), pp. 29–59. DOI: `https://doi.org/10.1016/0269-7491(88)90184-4`. URL: `https://www.sciencedirect.com/science/article/pii/0269749188901844`.

[16] J. H. Hu et al. “Reactive Uptake of Cl_2(g) and Br_2(g) by Aqueous Surfaces as a Function of Br^- and I^- Ion Concentration: The Effect of Chemical Reaction at the Interface”. In: *J. Phys. Chem.* 99 (1995), pp. 8768–8776. DOI: `10.1021/j100021a050`. URL: `https://pubs.acs.org/doi/abs/10.1021/j100021a050`.

[17] D. F. Liu et al. “Vibrational Spectroscopy of Aqueous Sodium Halide Solutions and Air-Liquid Interfaces: Observation of Increased Interfacial Depth”. In: *J. Phys. Chem. B* 108 (2004), pp. 2252–2260. DOI: `10.1021/jp036169r`. URL: `https://pubs.acs.org/doi/abs/10.1021/jp036169r`.

[18] D. Clifford and D. J. Donaldson. “ Direct Experimental Evidence for a Heterogeneous Reaction of Ozone with Bromide at the Air-Aqueous Interface”. In: *J. Phys. Chem. A* 111(39) (2007), pp. 9809–9814. DOI: `10.1021/jp074315d`. URL: `https://pubs.acs.org/doi/abs/10.1021/jp074315d`.

[19] A. Manna and A. Kumar. “ Why Does Water Accelerate Organic Reactions under Heterogeneous Condition?” In: *J. Phys. Chem. A* 117(12) (2013), pp. 2446–2454. DOI: `https://doi.org/10.1021/jp4002934`. URL: `https://pubs.acs.org/doi/abs/10.1021/jp4002934`.

[20] E. A. Pillar, R. C. Camm, and M. I. Guzman. “Catechol Oxidation by Ozone and Hydroxyl Radicals at the Air-Water Interface”. In: *Environ. Sci. Technol. Lett.* 48.20 (2014), pp. 14352–14360. DOI: `10.1021/es504094x`. URL: `https://doi.org/10.1021/es504094x`.

[21] D. Eisenberg and W. Kauzmann. *The Structure and Properties of Water*. Oxford University press, Oxford, 1969. ISBN: ISBN: 9780198570264.

[22] R. J. Speedy and C. A. Angell. “Isothermal Compressibility of Supercooled Water and Evidence for a Thermodynamic Singularity at -45 °C”. In: *J. Chem. Phys.* 65.3 (1976), pp. 851–858. DOI: `10.1063/1.433153`. eprint: `https://doi.org/10.1063/1.433153`. URL: `https://doi.org/10.1063/1.433153`.

[23] A. Nilsson and L. G. M. Pettersson. “Perspective on the Structure of Liquid Water”. In: *Chem. Phys.* 389.1 (2011), pp. 1 –34. ISSN: 0301-0104. DOI: `https://doi.org/10.1016/j.chemphys.2011.07.021`. URL: `http://www.sciencedirect.com/science/article/pii/S0301010411003247`.

[24] P. Ball. *Life's Matrix: A Biography of Water*. Berkeley and Los Angeles, California: University of California Press, 2001.

[25] L. G. M. Pettersson and A. Nilsson. "The Structure of Water: from Ambient to Deeply Supercooled". In: *Journal of Non-Crystalline Solids* 407 (2015). 7th IDMRCS: Relaxation in Complex Systems, pp. 399 –417. ISSN: 0022-3093. DOI: `https://doi.org/10.1016/j.jnoncrysol.2014.08.026`. URL: `http://www.sciencedirect.com/science/article/pii/S0022309314004104`.

[26] E. A. Raymond and G. L. Richmond. "Probing the Molecular Structure and Bonding of the Surface of Aqueous Salt Solutions". In: *J. Phys. Chem. B* 108 (2004), p. 5051. DOI: `10.1021/jp037725k`. URL: `https://pubs.acs.org/doi/10.1021/jp037725k`.

[27] S. E. McLain and A. K. Soper. "Structural Studies on the Hydration of l-Glutamic Acid in Solution". In: *J. Phys. Chem. B* 110 (2006), pp. 21251–21258. DOI: `10.1021/jp062383e`. URL: `https://pubs.acs.org/doi/abs/10.1021/jp062383e`.

[28] A. Morita and T. Ishiyama. "Recent Progress in Theoretical Analysis of Vibrational Sum Frequency Generation Spectroscopy". In: *Phys. Chem. Chem. Phys.* 10 (38 2008), pp. 5801–5816. DOI: `10.1039/b808110g`. URL: `http://dx.doi.org/10.1039/B808110G`.

[29] H.-F. Wang et al. "Quantitative Sum-Frequency Generation Vibrational Spectroscopy of Molecular Surfaces and Interfaces: Lineshape, Polarization, and Orientation". In: *Annual Review of Physical Chemistry* 66.1 (2015), pp. 189–216. DOI: `10.1146/annurev-physchem-040214-121322`.

[30] Y.-C. Wen et al. "Unveiling Microscopic Structures of Charged Water Interfaces by Surface-Specific Vibrational Spectroscopy". In: *Phys. Rev. Lett.* 116.1 (2016), p. 016101. DOI: `10.1103/physrevlett.116.016101`.

[31] T. Ishiyama and A. Morita. "Computational Analysis of Vibrational Sum Frequency Generation Spectroscopy". In: *Annual Review of Physical Chemistry* 68.1 (2017), pp. 355–377. DOI: `10.1146/annurev-physchem-052516-044806`.

[32] C. Peñalber-Johnstone et al. "Sum Frequency Generation Spectroscopy of Tetraalkylphosphonium Ionic Liquids at the Air-Liquid Interface". In: *J. Chem. Phys.* 148.19 (2018), p. 193841. DOI: `10.1063/1.5009674`. eprint: `https://doi.org/10.1063/1.5009674`. URL: `https://doi.org/10.1063/1.5009674`.

[33] F. Vidal and A. Tadjeddine. "Sum-Frequency Generation Spectroscopy of Interfaces". In: *Rep. Prog. Phys.* 68 (2005), pp. 1095–1127. DOI: `10.1088/0034-4885/68/5/r03`. URL: `https://www.onacademic.com/detail/journal_1000035594033610_0ae5.html`.

[34] Xing Wei et al. "Sum-Frequency Spectroscopic Studies of Ice Interfaces". In: *Phys. Rev. B* 66 (8 2002), p. 085401. DOI: `10.1103/PhysRevB.66.085401`. URL: `https://link.aps.org/doi/10.1103/PhysRevB.66.085401`.

[35] P. Guyot-Sionnest, J. H. Hunt, and Y. R. Shen. "Sum-Frequency Vibrational Spectroscopy of a Langmuir Film: Study of Molecular Orientation of a Two-Dimensional System". In: *Phys. Rev. Lett.* 59 (14 1987), pp. 1597–1600. DOI: `10.1103/PhysRevLett.59.1597`. URL: `https://link.aps.org/doi/10.1103/PhysRevLett.59.1597`.

[36] R. Superfine, J. H. Huang, and Y. R. Shen. "Nonlinear Optical Studies of the Pure Liquid/Vapor Interface: Vibrational Spectra and Polar Ordering". In: *Phys. Rev. Lett.* 66 (1991), pp. 1066–1069. DOI: 10.1103/PhysRevLett.66.1066. URL: https://ui.adsabs.harvard.edu/abs/1991PhRvL..66.1066S.

[37] Q. Du et al. "Vibrational Spectroscopy of Water at the Vapor/Water Interface". In: *Phys. Rev. Lett.* 70 (15 1993), pp. 2313–2316. DOI: 10.1103/PhysRevLett.70.2313. URL: https://link.aps.org/doi/10.1103/PhysRevLett.70.2313.

[38] Q. Du, E. Freysz, and Y. R. Shen. "Vibrational Spectra of Water Molecules at Quartz/Water Interfaces". In: *Phys. Rev. Lett.* 72 (2 1994), pp. 238–241. DOI: 10.1103/PhysRevLett.72.238. URL: http://link.aps.org/doi/10.1103/PhysRevLett.72.238.

[39] S. Gopalakrishnan et al. "Vibrational Spectroscopic Studies of Aqueous Interfaces: Salts, Acids, Bases, and Nanodrops". In: *Chem. Rev.* 106 (2006), pp. 1155–1175. DOI: 10.1021/cr040361n. URL: http://www.ncbi.nlm.nih.gov/pubmed/16608176.

[40] Y. R. Shen and V. Ostroverkhov. "Sum-Frequency Vibrational Spectroscopy on Water Interfaces: Polar Orientation of Water Molecules at Interfaces". In: *Chem. Rev.* 106 (2006), pp. 1140–1154. DOI: 10.1021/cr040377d. URL: https://www.ncbi.nlm.nih.gov/pubmed/16608175.

[41] M Che and J. C. Védrine (Ed.) *Characterization of Solid Materials and Heterogeneous Catalysts: From Structure to Surface Reactivity.* Vol. 1. Wiley-VCH, 2012, pp. 1075–1117.

[42] Peer Fischer et al. "Three-Wave Mixing in Chiral Liquids". In: *Phys. Rev. Lett.* 85 (20 2000), pp. 4253–4256. DOI: 10.1103/PhysRevLett.85.4253. URL: https://link.aps.org/doi/10.1103/PhysRevLett.85.4253.

[43] A. L. Harris et al. "Monolayer Vibrational Spectroscopy by Infrared-Visible Sum Generation at Metal and Semiconductor Surfaces". In: *Chem Phys. Lett.* 141 (1987), pp. 350–356. DOI: 10.1016/0009-2614(87)85037-6. URL: https://www.sciencedirect.com/science/article/abs/pii/0009261487850376.

[44] R. Superfine et al. "Surface vibrational spectroscopy of molecular adsorbates on metals and semiconductors by infrared-visible sum-frequency generation". In: *Surf. Sci.* 200 (1988), pp. L445–L450. DOI: 10.1016/0039-6028(88)90422-0. URL: https://www.sciencedirect.com/science/article/pii/0039602888904220.

[45] B. Rotenberg. "Water in Clay Nanopores". In: *MRS Bulletin* 39.12 (2014), pp. 1074–1081. DOI: 10.1557/mrs.2014.251. URL: https://doi.org/10.1557/mrs.2014.251.

[46] P. Jungwirth and D. J. Tobias. "Specific Ion Effects at the Air/Water Interface". In: *Chem. Rev.* 106 (2006), pp. 1259–1281. DOI: 10.1021/cr0403741. URL: https://pubs.acs.org/doi/abs/10.1021/cr0403741.

[47] Y. J. Zhang and P. S. Cremer. "Chemistry of Hofmeister Anions and Osmolytes". In: *Annu. Rev. Phys. Chem.* 61 (2010). DOI: 10.1146/annurev.physchem.59.032607.093635. URL: https://www.annualreviews.org/doi/abs/10.1146/annurev.physchem.59.032607.093635.

[48] D. Tobias and J. C. Hemminger. "Getting specific about specific ion effects". In: *Science* 319 (2008), pp. 1197–1198. DOI: 10.1126/science.1152799. URL: https://www.jstor.org/stable/20053465.

[49] D. F. Parsons et al. “Hofmeister Effects: Interplay of Hydration, Nonelectrostatic Potentials, and Ion Size”. In: *Phys. Chem. Chem. Phys.* 13 (27 2011), pp. 12352–12367. DOI: `10.1039/C1CP20538B`. URL: `http://dx.doi.org/10.1039/C1CP20538B`.

[50] P. Jungwirth and D. J. Tobias. “Molecular Structure of Salt Solutions: A New View of the Interface with Implications for Heterogeneous Atmospheric Chemistry”. In: *J. Phys. Chem. B* 105 (2001), pp. 10468–10472. DOI: `10.1021/jp012750g`. URL: `https://pubs.acs.org/doi/abs/10.1021/jp012750g`.

[51] P. Jungwirth and D. J. Tobias. “Ions at Air/Water Interface”. In: *J. Phys. Chem. B* 106 (2002), pp. 6361–6373. DOI: `10.1021/jp020242g`. URL: `https://pubs.acs.org/doi/abs/10.1021/jp020242g`.

[52] C. Tian et al. “Surface Propensities of Atmospherically Relevant Ions in Salt Solutions Revealed by Phase-Sensitive Sum Frequency Vibrational Spectroscopy”. In: *J. Phys. Chem. Lett.* 2 (2011), p. 1946. DOI: `10.1021/jz200791c`. URL: `https://pubs.acs.org/doi/abs/10.1021/jz200791c`.

[53] M. Xu et al. “Nitrate Anions and Ion Pairing at the Air-Aqueous Interface”. In: *J. Phys. Chem. C* 113 (2009), pp. 2082–2087. DOI: `10.1021/jp805376x`. URL: `https://pubs.acs.org/doi/abs/10.1021/jp805376x`.

[54] A. M. Jubb, W. Hua, and H. C. Allen. “Organization of Water and Atmospherically Relevant Ions and Solutes: Vibrational Sum Frequency Spectroscopy at the Vapor/Liquid and Liquid/Solid Interfaces”. In: *Accounts of Chemical Research* 45.1 (2012), pp. 110–119. DOI: `10.1021/ar200152v`. URL: `https://pubs.acs.org/doi/abs/10.1021/ar200152v`.

[55] K. Mizoguchi, T. Ujike, and Y. Tominaga. “Dynamics Structure of Water in NaCl Aqueous Solution”. In: *The Journal of Chemical Physics* 109.5 (1998), pp. 1867–1872. DOI: `10.1063/1.476763`. eprint: `https://doi.org/10.1063/1.476763`. URL: `https://doi.org/10.1063/1.476763`.

[56] C. M. Johnson and S. Baldelli. “Vibrational Sum Frequency Spectroscopy Studies of the Influence of Solutes and Phospholipids at Vapor/Water Interfaces Relevant to Biological and Environmental systems”. In: *Chem. Rev.* 114 (2014), pp. 8416–8446. DOI: `https://doi.org/10.1021/cr4004902`. URL: `https://pubs.acs.org/doi/abs/10.1021/cr4004902`.

[57] T. Ishiyama, T. Imamura, and A. Morita. “Theoretical Studies of Structures and Vibrational Sum Frequency Generation Spectra at Aqueous Interfaces”. In: *Chem. Rev.* 114 (2014), pp. 8447–8470. DOI: `10.1021/cr4004133`. URL: `https://pubs.acs.org/doi/abs/10.1021/cr4004133`.

[58] L. X. Dang. “Solvation of the Hydronium Ion at the Water Liquid/Vapor Interface”. In: *J. Chem. Phys.* 119 (2003), p. 6351. DOI: `https://doi.org/10.1063/1.1599274`. URL: `https://aip.scitation.org/doi/abs/10.1063/1.1599274`.

[59] M. K. Petersen et al. “The Hydrated Proton at the Water Liquid/Vapor Interface”. In: *J. Phys. Chem. B* 108 (2004), pp. 14804–14806. DOI: `10.1021/jp046716o`. URL: `https://pubs.acs.org/doi/abs/10.1021/jp046716o`.

[60] T. Ishiyama and A. Morita. “Molecular Dynamics Analysis of Interfacial Structures and Sum Frequency Generation Spectra of Aqueous Hydrogen Halide Solutions”. In: *J. Phys. Chem. A* 111.38 (2007), pp. 9277–9285. DOI: `10.1021/jp072997z`. eprint: `http://dx.doi.org/10.1021/jp072997z`. URL: `http://dx.doi.org/10.1021/jp072997z`.

[61] M. Mucha et al. "Unified Molecular Picture of the Surfaces of Aqueous Acid, Base, and Salt Solutions". In: *J. Phys. Chem. B* 109 (2005), pp. 7617–7623. DOI: 10.1021/jp0445730. URL: https://pubs.acs.org/doi/abs/10.1021/jp0445730.

[62] Ivan S. Ufimtsev, Nathan Luehr, and Todd J. Martinez. "Charge Transfer and Polarization in Solvated Proteins from Ab Initio Molecular Dynamics". In: *J. Phys. Chem. Lett.* 2.14 (2011), pp. 1789–1793. DOI: https://doi.org/10.1021/jz200697c. URL: https://pubs.acs.org/doi/abs/10.1021/jz200697c.

[63] Stefan Grimme. "Accurate Description of Van der Waals Complexes by Density Functional Theory Including Empirical Corrections". In: *Journal of Computational Chemistry* 25.12 (2004), pp. 1463–1473. ISSN: 01928651. DOI: 10.1002/jcc.20078. URL: https://onlinelibrary.wiley.com/doi/abs/10.1002/jcc.20078.

[64] S. Grimme. "Semiempirical GGA-Type Density Functional Constructed with a Long-Range Dispersion Correction". In: *J. Comput. Chem.* 27 (2006), pp. 1787–1799. DOI: 10.1002/jcc.20495. URL: https://onlinelibrary.wiley.com/doi/abs/10.1002/jcc.20495.

[65] Stefan Grimme et al. "Density Functional Theory with Dispersion Corrections for Supramolecular Structures, Aggregates, and Complexes of (Bio)Organic Molecules". In: *Org. Biomol. Chem.* 5 (5 2007), pp. 741–758. DOI: 10.1039/B615319B. URL: http://dx.doi.org/10.1039/B615319B.

[66] S. Grimme et al. "A Consistent and Accurate Ab Initio Parametrization of Density Functional Dispersion Correction (DFT-D) for the 94 Elements H-Pu". In: *J. Chem. Phys.* 132 (2010), p. 154104. DOI: 10.1063/1.3382344. URL: https://aip.scitation.org/doi/abs/10.1063/1.3382344.

[67] Marcel D. Baer et al. "Re-examining the Properties of the Aqueous Vapor-Liquid Interface using Dispersion Corrected Density Functional Theory". In: *J. Chem. Phys.* 135 (2011), p. 124712. DOI: 10.1063/1.3633239. URL: https://aip.scitation.org/doi/abs/10.1063/1.3633239.

[68] Teresa Fornaro et al. "Dispersion Corrected DFT Approaches for Anharmonic Vibrational Frequency Calculations: Nucleobases and Their Dimers". In: *Phys. Chem. Chem. Phys.* 16 (21 2014), pp. 10112–10128. DOI: 10.1039/C3CP54724H. URL: http://dx.doi.org/10.1039/C3CP54724H.

[69] F. H. Stillinger. "Water Revisited". In: *Science* 209 (1980), p. 451. DOI: 10.1126/science.209.4455.451. URL: https://science.sciencemag.org/content/209/4455/451.abstract.

[70] M. E. Tuckerman. *Statistical Mechanics: Theory and Molecular Simulation.* Oxford University Express, 2010.

[71] S. W. Rick, S. J. Stuart, and B. J. Berne. "Dynamical Fluctuating Force Fields: Application to Liquid Water". In: *J. Chem. Phys.* 101(7) (1994), p. 6141. DOI: 10.1063/1.468398. URL: arXiv:chem-ph/9406002.

[72] S. W. Rick and S. J. Stuart. "Potentials and Algorithms for Incorporating Polarizability in Computer Simulations". In: *Rev. Comput. Chem.* 18 (2002), pp. 89–146. DOI: 10.1002/0471433519.ch3. URL: https://onlinelibrary.wiley.com/doi/abs/10.1002/0471433519.ch3.

[73] G. Lamoureux, A. D. MacKerell, Jr., and B. Roux. “A Simple Polarizable Model of Water Based on Classical Drude Oscillators”. In: *J. Chem. Phys.* 119 (2003), p. 5185. DOI: `10.1063/1.1598191`. URL: `https://aip.scitation.org/doi/abs/10.1063/1.1598191`.

[74] M. E. Tuckerman. “Ab Initio Molecular Dynamics: Basic Concepts, Current Trends and Novel Applications”. In: *J. Phys.: Condens. Matter* 14 (2002), R1297–R1355. DOI: `10.1088/0953-8984/14/50/202`. URL: `https://ui.adsabs.harvard.edu/abs/2002JPCM...14R1297T`.

[75] A. Warshel and R. M. Weiss. “An Empirical Valence Bond Approach for Comparing Reactions in Solutions and in Enzymes”. In: *J. Am. Chem. Soc.* 102 (1980), pp. 6218–6226. DOI: `10.1021/ja00540a008`. URL: `http://pubs.acs.org/doi/10.1021/ja00540a008`.

[76] D. K. Remler and P. A. Madden. “Molecular Dynamics Without Effective Potentials via the Car-Parrinello Approach”. In: *Mol. Phys.* 70 (1990), pp. 921–966. DOI: `10.1080/00268979000101451`. URL: `https://doi.org/10.1080/00268979000101451`.

[77] M. C. Payne et al. “Iterative Minimization Techniques for Ab Initio Total-Energy Calculations: Molecular Dynamics and Conjugate Gradients”. In: *Rev. Mod. Phys.* 64 (4 1992), pp. 1045–1097. DOI: `10.1103/RevModPhys.64.1045`. URL: `https://link.aps.org/doi/10.1103/RevModPhys.64.1045`.

[78] M. P. Allen and D. J. Tildesley (Ed.) *Computer Simulation in Chemical Physics, chapter 8, First-Principles Molecular Dynamics.* NATO ASI Series C, 1993, p. 261. URL: `https://link.springer.com/chapter/10.1007/978-94-011-1679-4_8`.

[79] M. E. Tuckerman et al. “Ab Initio Molecular Dynamics Simulations”. In: *J. Phys. Chem.* 100 (1996), pp. 12878–12887. DOI: `10.1021/jp960480+`. URL: `https://pubs.acs.org/doi/abs/10.1021/jp960480+`.

[80] M. Parrinello. “From Silicon to RNA: The Coming of Age of Ab Initio Molecular Dynamics”. In: *Solid State Commun.* 102 (1997), pp. 107–120. DOI: `10.1016/S0038-1098(96)00723-5`. URL: `https://www.sciencedirect.com/science/article/abs/pii/S0038109896007235`.

[81] Marx D. and J. Hutter. “Ab Initio Molecular Dynamics: Theory and Implementation”. In: *Modern Methods and Algorithms of Quantum Chemistry (NIC Series) ed J Grotendorst (Forschungszentrum Juelich)* 1 (2000). URL: `https://juser.fz-juelich.de/record/44687/files/NIC-Band-1.pdf#page=311`.

[82] R. Car. “Introduction to Density-Functional Theory and Ab-Initio Molecular Dynamics”. In: *Quant. Struct. Act. Rel.* 21 (2002), pp. 97–104. URL: `https://onlinelibrary.wiley.com/doi/abs/10.1002/1521-3838(200207)21:2%3C97::AID-QSAR97%3E3.0.CO;2-6`.

[83] R. P. Feynman and A. R. Hibbs. *Quantum Mechanics and Path Integrals.* New York: McGraw-Hill, 1965.

[84] R. P. Feynman. *Statistical Mechanics: A Set of Lectures.* Benjamin, 1972.

[85] D. Marx and M. Parrinello. “Ab Initio Path Integral Molecular Dynamics: Basic Ideas”. In: *J. Chem. Phys.* 104 (1996), p. 4077. DOI: `10.1063/1.471221`. URL: `https://aip.scitation.org/doi/abs/10.1063/1.471221`.

[86] M. Tuckerman et al. "Efficient and General Algorithms for Path Integral Car-Parrinello Molecular Dynamics". In: *J. Chem. Phys.* 104 (1996), pp. 5579–5588. DOI: 10.1063/1.471771. URL: https://doi.org/10.1063/1.471771.

[87] Marx D., Tuckerman M. E., and Martyna G. J. "Quantum Dynamics via Adiabatic Ab Initio Centroid Molecular Dynamics". In: *Comput. Phys. Commun.* 118 (1999), p. 166. DOI: 10.1016/S0010-4655(99)00208-8. URL: https://www.sciencedirect.com/science/article/pii/S0010465599002088.

[88] J. VandeVondele et al. "QUICKSTEP: Fast and Accurate Density Functional Calculations using a Mixed Gaussian and Plane Waves Approach". In: *Computer Physics Commutations* 167 (2004), pp. 103–128. DOI: 10.1016/j.cpc.2004.12.014. URL: https://www.sciencedirect.com/science/article/pii/S0010465505000615.

[89] P. Hohenberg and W. Kohn. "Inhomogeneous Electron Gas". In: *Phys. Rev.* 136 (3B 1964), B864–B871. DOI: 10.1103/PhysRev.136.B864. URL: https://link.aps.org/doi/10.1103/PhysRev.136.B864.

[90] W. Kohn and L. J. Sham. "Quantum Density Oscillations in an Inhomogeneous Electron Gas". In: *Phys. Rev.* 137 (6A 1965), A1697–A1705. DOI: 10.1103/PhysRev.137.A1697. URL: https://link.aps.org/doi/10.1103/PhysRev.137.A1697.

[91] M. Levy. "Universal Variational Functionals of Electron Densities, First-Order Density Matrices, and Natural Spin-Orbitals and Solution of the v-Representability Problem". In: *Proc. Natl. Acad. Sci. USA.* 76 (1979), pp. 6062–6065. DOI: https://doi.org/10.1073/pnas.76.12.6062. URL: https://www.pnas.org/content/76/12/6062.short.

[92] Kieron Burke. *ABC of Density Functional Theory.* Department of Chemistry, University of California, Irvine, 2007.

[93] J. P. Perdew, K. Burke, and M. Ernzerhof. "Generalized Gradient Approximation Made Simple". In: *Phys. Rev. Lett.* 77 (18 1996), pp. 3865–3868. DOI: 10.1103/PhysRevLett.77.3865. URL: http://link.aps.org/doi/10.1103/PhysRevLett.77.3865.

[94] J. Kohanoff. *Electronic Structrue Calculations for Solids and Materials: Theory and Computational Methods.* Cambridge University Press, 2006.

[95] X. Wu et al. "Towards extending the applicability of density functional theory to weakly bound systems". In: *J. Chem. Phys.* 115 (2001), pp. 8748–8757. DOI: 10.1063/1.1412004. URL: https://doi.org/10.1063/1.1412004.

[96] Q. Wu and W. Yang. "Empirical Correction to Density Functional Theory for Van der Waals Interactions". In: *J. Chem. Phys.* 116 (2002), pp. 515–524. DOI: 10.1063/1.1424928. URL: https://aip.scitation.org/doi/abs/10.1063/1.1424928.

[97] U. Zimmerli, M. Parrinello, and P. Koumoutsakos. "Dispersion Corrections to Density Functionals for Water Aromatic Interactions". In: *J. Chem. Phys.* 120 (2004), p. 2693. DOI: 10.1063/1.1637034. URL: https://aip.scitation.org/doi/abs/10.1063/1.1637034.

[98] J. Klimeš and A. Michaelides. "Perspective: Advances and Challenges in Treating van der Waals Dispersion Forces in Density Functional Theory". In: *J. Chem. Phys.* 137.1 (2012), pp. 120901–120912. DOI: 10.1063/1.4754130. URL: https://aip.scitation.org/doi/full/10.1063/1.4754130.

[99] P Pulay. “Ab Initio Calculation of Force Constants and Equilibrium Geometries in Polyatomic Molecules: I. Theory”. In: *Mol. Phys.* 17.2 (1969), pp. 197–204. DOI: `10.1080/00268976900100941`. URL: `https://doi.org/10.1080/00268976900100941`.

[100] R. Car and M. Parrinello. “Unified Approach for Molecular Dynamics and Density Functional Theory”. In: *Phys. Rev. Lett.* 55 (22 1985), pp. 2471–2474. DOI: `10.1103/PhysRevLett.55.2471`. URL: `https://link.aps.org/doi/10.1103/PhysRevLett.55.2471`.

[101] J. VandeVondele et al. “Quickstep: Fast and Accurate Density Functional Calculations Using a Mixed Gaussian and Plane Waves Approach”. In: *Comp. Phys. Comm.* 167 (2005), pp. 103–128.

[102] Thomas D. Kühne et al. “CP2K: An electronic structure and molecular dynamics software package - Quickstep: Efficient and accurate electronic structure calculations”. In: *J. Chem. Phys.* 152.19 (2020), p. 194103. DOI: `10.1063/5.0007045`. eprint: `https://doi.org/10.1063/5.0007045`. URL: `https://doi.org/10.1063/5.0007045`.

[103] D. Frenkel and B. Smit. *Understanding Molecular Simulation.* Computational Science Series (Academic Press), 2nd ed, 2002.

[104] G. Kresse and J. Hafner. “Ab Initio Molecular Dynamics for Liquid Metals”. In: *Phys. Rev. B* 47 (1 1993), pp. 558–561. DOI: `10.1103/PhysRevB.47.558`. URL: `https://link.aps.org/doi/10.1103/PhysRevB.47.558`.

[105] M. T. Dove. *Introduction to Lattice Dynamics.* Cambridge: Cambridge University Press, 1993.

[106] J. M. Dickey and A. Paskin. “Computer Simulation of the Lattice Dynamics of Solids”. In: *Phys. Rev.* 188 (1969), p. 1407.

[107] M. P. Allen and D. J. Tildesley. *Computer Simulation of Liquid.* Clarendon Express, Oxford, 1986.

[108] A. L. Harris et al. “Vibrational Energy Transfer to Metal Surfaces Probed by Sum Generation: CO/Cu(100) and CH_3S/Ag(111)”. In: *J. Electron Spec. Related Phenomena* 54155 (1990), pp. 5–16. DOI: `10.1016/0368-2048(90)80196-H`. URL: `https://www.sciencedirect.com/science/article/abs/pii/036820489080196H`.

[109] A. L. Harris et al. “Molecular Vibrational Energy Relaxation at Metal Surfaces by Picosecond Infrared-Visible Sum Spectroscopy”. In: *International Quantum Electronics Conference.* Optical Society of America, 1990, QTHK1. URL: `http://www.osapublishing.org/abstract.cfm?URI=IQEC-1990-QTHK1`.

[110] H.-L. Dai and W. Ho. *Laser Spectroscopy and Photochemistry on Metal Surfaces: part 1.* World Scientific Publishing Co. Pte. Ldt., 1995.

[111] P. Halevi (Ed.) *Photonic Probes of Surfaces.* Progress in Quantum Electronics, 1996, p. 255.

[112] A. Wieckowski. *Interfacial Electrochemistry: Theory, Experiment and Applications.* CRC Press, 1999, p. 992.

[113] Z. Chen, D. Gracias, and G. Somorjai. “Sum Frequency Generation (SFG)-Surface Vibrational Spectroscopy Studies of Buried Interfaces: Catalytic Reaction Intermediates on Transition Metal Crystal Surfaces at High Reactant Pressures; Polymer Surface Structures at the Solid-Gas and Solid-Liquid Interfaces”. In: *Appl. Phys. B* 68 (1999), p. 549. DOI: `10.1007/s003400050664`. URL: `https://link.springer.com/article/10.1007/s003400050664`.

[114] Z. Chen. “Understanding Surfaces and Buried Interfaces of Polymer Materials at the Molecular Level Using Sum Frequency Generation Vibrational Spectroscopy”. In: *Polymer International* 56(5) (2007), pp. 577–587. DOI: `10.1002/pi.2201`. URL: `https://deepblue.lib.umich.edu/bitstream/handle/2027.42/56019/2201_ftp.pdf?sequence=1`.

[115] R. Khatib et al. “Water Orientation and Hydrogen-Bond Structure at the Fluorite/Water Interface”. In: *Scientific Reports* 6 (2016), p. 24287. DOI: `https://doi.org/10.1038/srep24287`. URL: `https://www.nature.com/articles/srep24287`.

[116] R. Khatib et al. “Molecular Dynamics Simulations of SFG Librational Modes Spectra of Water at the Water-Air Interface”. In: *J. Phys. Chem. C* 120 (2016), pp. 18665–18673. DOI: `https://doi.org/10.1021/acs.jpcc.6b06371`. URL: `https://pubs.acs.org/doi/abs/10.1021/acs.jpcc.6b06371`.

[117] R. Khatib and M. Sulpizi. “Sum Frequency Generation Spectra from Velocity-Velocity Correlation Functions”. In: *J. Phys. Chem. Lett.* 8 (2017), pp. 1310–1314. DOI: `https://doi.org/10.1021/acs.jpclett.7b00207`. URL: `https://pubs.acs.org/doi/abs/10.1021/acs.jpclett.7b00207`.

[118] S. Mukamel. *Principles of Nonlinear Optical Spectroscopy.* Oxford University Press, Oxford, 1995.

[119] C. M. Pradier and Y. J. Chabal (Ed.) *Biointerface Characterization by Advanced IR Spectroscopy.* Elsevier, 2011, p. 344.

[120] R. Vanselow and R. Howe. *Chemistry and Physics of Solid Surfaces VIII.* 2012, p. 464.

[121] A. Morita and J. T. Hynes. “A Theoretical Analysis of the Sum Frequency Generation Spectrum of the Water Surface. II. Time-Dependent Approach”. In: *J. Phys. Chem. B* 106 (2002), pp. 673–685. DOI: `10.1021/jp0133438`. URL: `https://pubs.acs.org/doi/abs/10.1021/jp0133438`.

[122] A. Morita and J. T. Hynes. “A Theoretical Analysis of the Sum Frequency Generation Spectrum of the Water Surface”. In: *J. Chem. Phys.* 258 (2000), pp. 371–390. DOI: `http://dx.doi.org/10.1016/S0301-0104(00)00127-0`. URL: `http://www.sciencedirect.com/science/article/pii/S0301010400001270`.

[123] S. Nihonyanagi et al. “Unified Molecular View of the Air/Water Interface Based on Experimental and Theoretical $\chi^{(2)}$ Spectra of an Isotopically Diluted Water Surface”. In: *J. Am. Chem. Soc.* 133 (2011), pp. 16875–16880. DOI: `10.1021/ja2053754`. URL: `https://pubs.acs.org/doi/abs/10.1021/ja2053754`.

[124] S. A. Corcelli and J. L. Skinner. “Infrared and Raman Line Shapes of Dilute HOD in Liquid H_2O and D_2O from 10 to 90 °C”. In: *J. Phys. Chem. A* 109 (2005), pp. 6154–6165. DOI: `https://doi.org/10.1021/jp0506540`. URL: `https://pubs.acs.org/doi/abs/10.1021/jp0506540`.

[125] N. Marzari and D. Vanderbilt. “Maximally Localized Generalized Wannier Functions for Composite Energy Bands”. In: *Phys. Rev. B* 56 (20 1997), pp. 12847–12865. DOI: 10.1103/PhysRevB.56.12847. URL: https://link.aps.org/doi/10.1103/PhysRevB.56.12847.

[126] M. Salanne et al. “Polarizabilities of individual molecules and ions in liquids from first principles”. In: *J. Phys. Condens. Matter.* 20.49 (2008), p. 494207. URL: http://stacks.iop.org/0953-8984/20/i=49/a=494207.

[127] M. Sulpizi et al. “Vibrational Sum Frequency Generation Spectroscopy of the Water Liquid-Vapor Interface from Density Functional Theory-Based Molecular Dynamics Simulations”. In: *J. Phys. Chem. Lett.* 4.1 (2013), pp. 83–87. DOI: 10.1021/jz301858g. eprint: http://dx.doi.org/10.1021/jz301858g. URL: http://dx.doi.org/10.1021/jz301858g.

[128] P. Salvador et al. “Polarizability of the Nitrate Anion and Its Solvation at the Air/Water Interface”. In: *Phys. Chem. Chem. Phys.* 5 (17 2003), pp. 3752–3757. DOI: 10.1039/B304537D. URL: http://dx.doi.org/10.1039/B304537D.

[129] A. M. Jubb, W. Hua, and H. Allen. “Environmental Chemistry at Vapor/Water Interfaces: Insights from Vibrational Sum Frequency Generation Spectroscopy”. In: *Ann. Rev. Phys. Chem.* 63 (2012), pp. 107–130. DOI: 10.1146/annurev-physchem-032511-143811. URL: https://www.annualreviews.org/doi/abs/10.1146/annurev-physchem-032511-143811.

[130] W. Hua, D. Verreault, and H. C. Allen. “Surface Electric Fields of Aqueous Solutions of NH_4NO_3, $Mg(NO_3)_2$, $NaNO_3$, and $LiNO_3$: Implications of Atmospheric Aerosol Chemistry”. In: *J. Phys. Chem. C* 118 (2014), pp. 24941–24949. DOI: https://doi.org/10.1021/jp505770t. URL: https://pubs.acs.org/doi/abs/10.1021/jp505770t.

[131] P. K. Weissenborn and R. J. Pugh. “Surface Tension and Bubble Coalescence Phenomena of Aqueous Solutions of Electrolytes”. In: *Langmuir* 11.5 (1995), pp. 1422–1426. DOI: 10.1021/la00005a002.

[132] Michael J. Hey et al. “Surface Tensions of Aqueous Solutions of Some 1:1 Electrolytes”. In: *J. Chem. Soc., Faraday Trans. 1* 77 (1 1981), pp. 123–128. DOI: 10.1039/F19817700123. URL: http://dx.doi.org/10.1039/F19817700123.

[133] N. L. Jarvis and M. A. Scheiman. “Surface Potentials of Aqueous Electrolyte Solution”. In: *Journal of Physical Chemistry* 72.1 (1968), pp. 74–78. ISSN: 00223654. DOI: 10.1021/j100847a014. URL: https://pubs.acs.org/doi/abs/10.1021/j100847a014.

[134] N L Jarvis. “Effect of Various Salts on the Surface Potential of Water-Air Interface”. In: 77.27 (1972), pp. 5177–5182. DOI: 10.1029/JC077i027p05177. URL: https://agupubs.onlinelibrary.wiley.com/doi/abs/10.1029/JC077i027p05177.

[135] L. M. Pegram and M. T. Record, Jr. “Partitioning of Atmospherically Relevant Ions between Bulk Water and the Water/Vapor Interface”. In: *Proceedings of the National Academy of Sciences* 103.39 (2006), pp. 14278–14281. ISSN: 0027-8424. DOI: 10.1073/pnas.0606256103. eprint: NIHMS150003. URL: http://www.pnas.org/cgi/doi/10.1073/pnas.0606256103.

[136] W. Hua, A. M. Jubb, and H. C. Allen. “Electric Field Reversal of Na_2SO_4, $(NH_4)_2SO_4$, and Na_2CO_3 Relative to $CaCl_2$ and NaCl at the Air/Aqueous Interface Revealed by Heterodyne Detected Phase-Sensitive Sum Frequency”. In: *J. Phys. Chem. Lett.* 2 (2011), pp. 2515–2520. DOI: `https://doi.org/10.1021/jz200888t`. URL: `https://pubs.acs.org/doi/abs/10.1021/jz200888t`.

[137] W. Hua, X. Chen, and H. C. Allen. “Phase-Sensitive Sum Frequency Revealing Accommodation of Bicarbonate Ions, and Charge Separation of Sodium and Carbonate Ions within the Air/Water Interface”. In: *J. Phys. Chem. A* 115 (2011), pp. 6233–6238. DOI: `10.1021/jp111552f`. URL: `https://pubs.acs.org/doi/abs/10.1021/jp111552f`.

[138] X. Chen, W. Hua, and H. C. Allen. “Interfacial Water Structure Associated with Phospholipid Membranes Studied by Phase-Sensitive Vibrational Sum Frequency Generation Spectroscopy”. In: *J. Am. Chem. Soc.* 132.32 (2010), pp. 11336–11342. DOI: `10.1021/ja1048237`. URL: `https://pubs.acs.org/doi/abs/10.1021/ja1048237`.

[139] D. Verreault and H. C. Allen. “Bridging the Gap between Microscopic and Macroscopic Views of Air/Aqueous Salt Interfaces”. In: *Chem. Phys. Lett.* 586 (2013), pp. 1–9. DOI: `10.1016/j.cplett.2013.08.054`. URL: `http://www.sciencedirect.com/science/article/pii/S0009261413010646`.

[140] D. Verreault and H. C. Allen. “Reactions at Surfaces in the Atmosphere: Integration of Experiments and Theory as Necessary (But Not Necessarily Sufficient) for Predicting the Physical Chemistry of Aerosols”. In: *Phys. Chem. Chem. Phys.* 11 (2009), pp. 7760–7779. DOI: `10.1039/b906540g`. URL: `http://pubs.rsc.org/en/content/articlepdf/2009/cp/b906540g`.

[141] L. Jiang et al. “Gas-Phase Vibrational Spectroscopy of Microhydrated Magnesium Nitrate Ions $[MgNO_3(H_2O)_{1-4}]^+$”. In: *J. Am. Chem. Soc.* 132 (2010), pp. 7398–7404. DOI: `10.1021/ja1011806`. URL: `https://pubs.acs.org/doi/abs/10.1021/ja1011806`.

[142] N. Heinea and K. R. Asmis. “Cryogenic Ion Trap Vibrational Spectroscopy of Hydrogen-Bonded Clusters Relevant to Atmospheric Chemistry”. In: *J. Am. Chem. Soc.* 34.1 (2015), pp. 1–34. DOI: `https://doi.org/10.1080/0144235X.2014.979659`. URL: `https://www.tandfonline.com/doi/full/10.1080/0144235X.2014.979659`.

[143] J. Teixeira, M. C. Bellisent-Funel, and S. H. Chen. “Dynamics of Water Studied by Neutron Scattering”. In: *J. Phys. Condens. Matter* 2 (1990), SA105. DOI: `10.1088/0953-8984/2/S/011`. URL: `http://iopscience.iop.org/0953-8984/2/S/011`.

[144] Sundaram Balasubramanian, Subrata Pal, and Biman Bagchi. “Hydrogen-Bond Dynamics Near a Micellar Surface: Origin of the Universal Slow Relaxation at Complex Aqueous Interfaces”. In: *Phys. Rev. Lett.* 89 (11 2002), p. 115505. DOI: `10.1103/PhysRevLett.89.115505`. URL: `https://link.aps.org/doi/10.1103/PhysRevLett.89.115505`.

[145] Jr. O. Rodriguez and J. M. Lisy. “Revisiting $Li^+(H_2O)_{3-4}Ar_1$ Clusters: Evidence of High-Energy Conformers from Infrared Spectra”. In: *J. Phys. Chem. Lett.* 2 (2011), p. 1444. DOI: `10.1021/jp112087e`. URL: `https://doi.org/10.1021/jp112087e`.

[146] D. J. Miller and J. M. Lisy. “Hydrated Alkali-Metal Cations: Infrared Spectroscopy and Ab Initio Calculations of $M^+(H_2O)_{x=2-5}Ar$ Cluster Ions for M = Li, Na, K, and Cs”. In: *J. Am. Chem. Soc.* 130 (2008), pp. 15381–15392. DOI: `10.1021/ja803665q`. URL: `https://pubs.acs.org/doi/abs/10.1021/ja803665q`.

[147] D. J. Miller and J. M. Lisy. “Entropic Effects on Hydrated Alkali-Metal Cations: Infrared Spectroscopy and Ab Initio Calculations of $M^+(H_2O)_{x=2-5}$ Cluster Ions for M = Li, Na, K, and Cs”. In: *J. Am. Chem. Soc.* 130 (2008), p. 15393. DOI: `10.1021/ja803666m`. URL: `https://pubs.acs.org/doi/abs/10.1021/ja803666m`.

[148] J. P. Beck and J. M. Lisy. “Infrared Spectroscopy of Hydrated Alkali Metal Cations: Evidence of Multiple Photon Absorption”. In: *J. Chem. Phys.* 135 (2011), p. 044302. DOI: `10.1063/1.3609760`. URL: `https://aip.scitation.org/doi/abs/10.1063/1.3609760`.

[149] D. E. Otten, P. B. Petersen, and R. J. Saykally. “Observation of Nitrate Ions at the Air/Water Interface by UV-Second Harmonic Generation”. In: *Chem. Phys. Lett.* 449 (4-6 2007), pp. 261–265. DOI: `10.1016/j.cplett.2007.10.081`. URL: `https://www.sciencedirect.com/science/article/abs/pii/S0009261407014017`.

[150] D. J. Tobias et al. “Simulation and Theory of Ions at Atmospherically Relevant Aqueous Liquid-Air Interfaces”. In: *Annu. Rev. Phys. Chem.* 64 (2013), pp. 339–359. DOI: `10.1146/annurev-physchem-040412-110049`. URL: `http://www.annualreviews.org/doi/pdf/10.1146/annurev-physchem-040412-110049`.

[151] E. S. Shamay et al. “At the Water’s Edge: Nitric Acid as Weak Acid”. In: *J. Am. Chem. Soc.* 129.43 (2007), p. 12910. DOI: `10.1021/ja074811f`. URL: `https://doi.org/10.1021/ja074811f`.

[152] Y. Marechál. “The Molecular Structure of Liquid Water Delivered by Absorption Spectroscopy in the Whole IR Region Completed with Thermodynamics Data”. In: *J. molecular structure* 1004 (2011), pp. 146–155. DOI: `10.1016/j.molstruc.2011.07.054`. URL: `https://www.sciencedirect.com/science/article/abs/pii/S0022286011006247`.

[153] S. Baldelli, C. Schnitzer, and M. J. Shultz. “Sum Frequency Generation Investigation of Water at the Surface of H_2O/H_2SO_4 Binary Systems”. In: *J. Phys. Chem. B* 101 (1997), pp. 10435–10441. DOI: `10.1021/jp972376d`. URL: `https://pubs.acs.org/doi/abs/10.1021/jp972376d`.

[154] L. M. Pegram and M. T. Record Jr. “Partitioning of Atmospherically Relevant Ions between Bulk Water and the Water/Vapor Interface”. In: *Proc. Natl. Acad. Sci. USA* 103 (2006), pp. 14278–14281.

[155] L. M. Pegram and M. T. Record, Jr. “Thermodynamic Origin of Hofmeister Ion Effects”. In: *J. Phys. Chem. B* 112 (2008), pp. 9428–9436. DOI: `10.1021/jp800816a`. URL: `https://pubs.acs.org/doi/abs/10.1021/jp800816a`.

[156] E. A. Carter et al. “Constrained Reaction Coordinate Dynamics for the Simulation of Rare Events”. In: *Chem. Phys. Lett.* 156 (1989), p. 472.

[157] M. Sprik and G. Ciccotti. “Free energy from constrained molecular dynamics”. In: *J. Chem. Phys.* 109 (1998), p. 7737.

[158] M. E. Tuckerman. *Statistical Mechanics: Theory and Molecular Simulation.* Oxford University Press, 2010.

[159] S. Ghosal et al. “Electron Spectroscopy of Aqueous Solution Interfaces Reveals Surface Enhancement of Halides”. In: *Science* 307 (2005), p. 563. DOI: `10.1126/science.1106525`. URL: `https://science.sciencemag.org/content/307/5709/563`.

[160] L. X. Dang and T.-M. Chang. “Molecular Mechanism of Ion Binding to the Liquid/Vapor Interface of Water”. In: *J. Phys. Chem. B* 106 (2002), pp. 235–238. DOI: `https://doi.org/10.1021/jp011853w`. URL: `https://pubs.acs.org/doi/abs/10.1021/jp011853w`.

[161] L. Vrbka et al. “Propensity of Soft Ions for the Air/Water Interface”. In: *Current Opinion in Colloid and Interface Science* 9 (2004), pp. 67–73. DOI: `10.1016/j.cocis.2004.05.028`. URL: `https://www.sciencedirect.com/science/article/pii/S1359029404000330`.

[162] B. C. Garrett. “Ions at the Air/Water Interface”. In: *Science* 303.5661 (2004), pp. 1146–1147. DOI: `10.1126/science.1089801`. URL: `https://science.sciencemag.org/content/303/5661/1146`.

[163] P. Bajaj, A. W. Götz, and F. Paesani. “Toward Chemical Accuracy in the Description of Ion-Water Interactions through Many-Body Representations. I. Halide-Water Dimer Potential Energy Surfaces”. In: *J. Chem. Theory Comput.* 12 (2016), pp. 2698–2705. DOI: `10.1021/acs.jctc.6b00302`. URL: `https://pubs.acs.org/doi/abs/10.1021/acs.jctc.6b00302`.

[164] D. F. Liu et al. “Vibrational Spectroscopy of Aqueous Sodium Halide Solutions and Air-Liquid Interfaces: Observation of Increased Interfacial Depth”. In: *J. Phys. Chem. B* 108 (2004), pp. 2252–2260. DOI: `10.1021/jp036169r`. URL: `https://pubs.acs.org/doi/abs/10.1021/jp036169r`.

[165] M. J. Shultz et al. “Sum Frequency Generation Spectroscopy of the Aqueous Interface: Ionic and Soluble Molecular Solutions”. In: *Int. Rev. Phys. Chem.* 19.1 (2010), pp. 123–153.

[166] A. Luzar. “Water Hydrogen-Bond Dynamics Close to Hydrophobic and Hydrophilic groups”. In: *Faraday Discuss.* 103 (0 1996), pp. 29–40. DOI: `10.1039/FD9960300029`. URL: `http://dx.doi.org/10.1039/FD9960300029`.

[167] Bernard Cabane and Rodolphe Vuilleumier. “The physics of liquid water”. In: 2005, pp. 159–171. DOI: `10.1016/j.crte.2004.09.018`.

[168] Janamejaya Chowdhary and Branka M. Ladanyi. “Hydrogen Bond Dynamics at the Water/Hydrocarbon Interface”. In: *The Journal of Physical Chemistry B* 113 (13 Nov. 2008), pp. 4045–4053. DOI: `10.1021/jp8061509`.

[169] L.-Å. Näslund et al. “X-ray Absorption Spectroscopy Study of the Hydrogen Bond Network in the Bulk Water of Aqueous Solutions”. In: *J. Phys. Chem. A* 109.27 (2005), 5995–6002. DOI: `10.1021/jp050413s`. URL: `https://doi.org/10.1021/jp050413s`.

[170] A. Tongraar, P. Tangkawanwanit, and B. M. Rode. “A Combined QM/MM Molecular Dynamics Simulations Study of Nitrate Anion (NO_3^-) in Aqueous Solution”. In: *J. Phys. Chem. A* 110.47 (2006), pp. 12918–12926. DOI: `10.1021/jp064779w`. URL: `https://pubs.acs.org/doi/abs/10.1021/jp064779w`.

[171] J. Chanda and S. Bandyopadhyay. “Hydrogen Bond Lifetime Dynamics at the Interface of a Surfactant Monolayer”. In: *J. Phys. Chem. B* 110.46 (2006), pp. 23443–23449.

[172] A. Tongraar, S. Hannongbua, and B. M. Rode. “QM/MM MD Simulations of Iodide Ion (I-) in Aqueous Solution: A Delicate Balance Between Ion-Water and Water-Water H-bond Interactions”. In: *J. Phys. Chem. A* 114.12 (2010), pp. 4334–4339. ISSN: 10895639. DOI: `10.1021/jp910435d`. URL: `https://www.ncbi.nlm.nih.gov/pubmed/20196599`.

[173] Puja Banerjee, Subramanian Yashonath, and Biman Bagchi. “Coupled jump rotational dynamics in aqueous nitrate solutions”. In: *The Journal of Chemical Physics* 145.23 (2016), p. 234502. DOI: `10.1063/1.4971864`. eprint: `https://aip.scitation.org/doi/pdf/10.1063/1.4971864`. URL: `https://aip.scitation.org/doi/abs/10.1063/1.4971864`.

[174] Jasper C. Werhahn et al. “Dynamics of Weak, Bifurcated, and Strong Hydrogen Bonds in Lithium Nitrate Trihydrate”. In: *J. Phys. Chem. Lett.* 2 (2011), pp. 1633–1638. DOI: `dx.doi.org/10.1021/jz200591v`. URL: `https://pubs.acs.org/doi/abs/10.1021/jz200591v`.

[175] J. A. Fournier et al. “Interplay of Ion-Water and Water-Water Interactions within the Hydration Shells of Nitrate and Carbonate Directly Probed with 2D IR Spectroscopy”. In: *J. Am. Chem. Soc.* 138.30 (2016), pp. 9634–9645. DOI: `10.1021/jacs.6b05122`.

[176] A. Luzar and D. Chandler. “Effect of Environment on Hydrogen Bond Dynamics in Liquid Water”. In: *Phys. Rev. Lett.* 76 (6 1996), pp. 928–931. DOI: `10.1103/PhysRevLett.76.928`. URL: `https://link.aps.org/doi/10.1103/PhysRevLett.76.928`.

[177] D. Chandler. *Introduction to Morden Statistical Mechanics*. Oxford University press, Oxford, 1987.

[178] Amalendu Chandra. “Effects of Ion Atmosphere on Hydrogen-Bond Dynamics in Aqueous Electrolyte Solutions”. In: *Phys. Rev. Lett.* 85 (4 2000), pp. 768–771. DOI: `10.1103/PhysRevLett.85.768`. URL: `https://link.aps.org/doi/10.1103/PhysRevLett.85.768`.

[179] S. Pal, B. Bagchi, and S. Balasubramanian. “Hydration Layer of a Cationic Micelle, C_{10}TAB: Structure, Rigidity, Slow Reorientation, Hydrogen Bond Lifetime, and Solvation Dynamics”. In: *J. Phys. Chem. B* 109 (2005), pp. 12879–12890. DOI: `10.1021/jp0510793`. URL: `https://pubs.acs.org/doi/abs/10.1021/jp0510793`.

[180] A. K. Soper and M. G. Phillips. “A New Determination of the Structure of Water at 25 °C”. In: *Chem. Phys* 107 (1986), pp. 47–60. DOI: `10.1016/0301-0104(86)85058-3`. URL: `https://www.sciencedirect.com/science/article/abs/pii/0301010486850583`.

[181] F. Sciortino and S. Pornili. “Hydrogen Bond Cooperativity in Simulated Water: Time Dependence Analysis of Pair Interactions”. In: *J. Chem. Phys.* 90.5 (1989), pp. 2786–2792. DOI: `10.1063/1.455927`. URL: `https://doi.org/10.1063/1.455927`.

[182] Alenka Luzar and David Chandler. “Structure and hydrogen bond dynamics of water–dimethyl sulfoxide mixtures by computer simulations”. In: *J. Chem. Phys.* 98.10 (1993), pp. 8160–8173. DOI: `10.1063/1.464521`. URL: `https://doi.org/10.1063/1.464521`.

[183] D. C. Rapaport. “Hydrogen Bonds in Water: Network Organization and Lifetimes”. In: *Mol. Phys.* 50 (1983), pp. 1151–1162. DOI: `10.1080/00268978300102931`. URL: `https://doi.org/10.1080/00268978300102931`.

[184] G. G. Malenkov. “Structure and Dynamics of Liquid Water”. In: *J. Struct. Chem.* 47 (2006), S1–S31. DOI: `https://doi.org/10.1007/s10947-006-0375-8`. URL: `https://doi.org/10.1007/s10947-006-0375-8`.

[185] G. G. Malenkov, A. V. Teplukhin, and V. I. Poltev. “I-and F-Structures of Liquid Water”. In: *J. Struct. Chem.* 30.1 (1990), pp. 89–97. URL: `https://link.springer.com/content/pdf/10.1007/BF00751454.pdf`.

[186] Rustam Z. Khaliullin and Thomas D. Kühne. “Microscopic Properties of Liquid Water from Combined Ab Initio Molecular Dynamics and Energy Decomposition Studies”. In: *Phys. Chem. Chem. Phys.* 15 (38 2013), pp. 15746–15766. DOI: `10.1039/C3CP51039E`. URL: `http://dx.doi.org/10.1039/C3CP51039E`.

[187] S. Chowdhuri and A. Chandra. “Dynamics of Halide Ion-Water Hydrogen Bonds in Aqueous Solutions: Dependence on Ion Size and Temperature”. In: *J. Phys. Chem. B* 110 (2006), pp. 9674–9680. DOI: `10.1021/jp057544d`. URL: `https://pubs.acs.org/doi/abs/10.1021/jp057544d`.

[188] F. Sciortino et al. “Lifetime of the Bond Network and Gel-Like Anomalies in Supercooled Water”. In: *Phys. Rev. Lett.* 64.14 (1990), pp. 1686–1689. DOI: `10.1103/PhysRevLett.64.1686`. URL: `https://link.aps.org/doi/10.1103/PhysRevLett.64.1686`.

[189] T. Krausche and W. Nadler. “Statistical Mechanics of Hydrogen Bond Networks”. In: *Z. Phys. B: Condens. Matter* 86.5 (1992), p. 433. URL: `https://link.springer.com/content/pdf/10.1007/BF01323737.pdf`.

[190] F. W. Starr, J. K. Nielsen, and H. E. Stanley. “Fast and Slow Dynamics of Hydrogen Bonds in Liquid Water”. In: *Phys. Rev. Lett.* 82.11 (1999), p. 2294.

[191] V. P. Voloshin and Yu. I. Naberukhin. “Hydrogen Bond Lifetime Distributions in Computer-Simulated Water”. In: *J. Structural Chem.* 50 (2009), pp. 78–89.

[192] A. Geiger et al. “Structure and Dynamics of the Hydrogen Bond Network in Water by Computer Simulations”. In: *J. Phys. (Paris)* 45 (1984), pp. C7–13–C7–30.

[193] O. Mishima M. R. Sadr-Lahijany A. Scala H. E. Stanley S. V. Buldyrev and F. W. Starr. “Unsolved Mysteries of Water in its Liquid and Glassy Phases”. In: *J. Phys.: Condens. Matter* 12 (2000). URL: `https://iopscience.iop.org/article/10.1088/0953-8984/12/8A/355/pdf`.

[194] A. Luzar. “Resolving the Hydrogen Bond Dynamics Conundrum”. In: *J. Chem. Phys.* 113 (2000), p. 10663. DOI: `10.1063/1.1320826`. URL: `https://aip.scitation.org/doi/abs/10.1063/1.1320826`.

[195] F. W. Starr, J. K. Nielsen, and H. Eugene Sta. “Hydrogen-Bond Dynamics for the Extended Simple Point-Charge Model of Water”. In: *Phys. Rev. E* 62 (2000), pp. 579–587. DOI: `10.1103/physreve.62.579`. URL: `https://www.ncbi.nlm.nih.gov/pubmed/11088494`.

[196] D. Chandler. “Roles of Classical Dynamics and Quantum Dynamics on Activated Processes Occurring in Liquids”. In: *J. Stat. Phys.* 42 (1986), pp. 49–67. DOI: `10.1007/BF01010840`. URL: `https://link.springer.com/article/10.1007/BF01010840`.

[197] D. Chandler. “Statistical Mechanics of Isomerization Dynamics in Liquids and the Transition State Approximation”. In: *J. Chem. Phys.* 68 (1978), pp. 2959–2970. DOI: `10.1063/1.436049`. URL: `https://aip.scitation.org/doi/abs/10.1063/1.436049`.

[198] J. Kessler et al. “Structure and Dynamics of the Instantaneous Water/Vapor Interface Revisited by Path-Integral and Ab Initio Molecular Dynamics Simulations”. In: *J. Phys. Chem. B* 199.31 (2015), pp. 10079–10086. DOI: `10.1021/acs.jpcb.5b04185`. URL: `https://pubs.acs.org/doi/10.1021/acs.jpcb.5b04185`.

[199] A. Luzar and D. Chandler. “Hydrogen-Bond Kinetics in Liquid Water”. In: *Nature* 379 (1996), pp. 55–57. DOI: `10.1038/379055a0`. URL: `https://www.nature.com/articles/379055a0`.

[200] Hee-Seung Lee and Mark E. Tuckerman. “Dynamical Properties of Liquid Water from Ab Initio Molecular Dynamics Performed in the Complete Basis Set Limit”. In: *J. Chem. Phys.* 126.16 (2007), p. 164501. DOI: `10.1063/1.2718521`. URL: `https://doi.org/10.1063/1.2718521`.

[201] H. Ishikita and K. Saito. “Proton Transfer Reactions and Hydrogen-Bond Networks in Protein Environments”. In: *J. R. Soc. Interface* 11.91 (2013), p. 20130518. DOI: `10.1098/rsif.2013.0518`. URL: `https://www.ncbi.nlm.nih.gov/pmc/articles/PMC3869154/`.

[202] H. Tanaka, K. Nakanishi, and N. Watanabe. “Constant Temperature Molecular Dynamics Calculation on Lennard-Jones Fluid and Its Application to Water”. In: *J. Chem. Phys.* 78.5 (1983), pp. 2622–2634. DOI: `https://doi.org/10.1063/1.445020`. URL: `https://aip.scitation.org/doi/10.1063/1.445020`.

[203] Yu. I. Naberukhin and V. P. Voloshin. “Distributions of Hydrogen Bond Lifetimes in Instantaneous and Inherent Structures of Water”. In: *Z. Phys. Chem.* 223 (2009), pp. 999–1011. DOI: `10.1524/zpch.2009.6062`.

[204] A. P. Willard and D. Chandler. “Instantaneous Liquid Interfaces”. In: *J. Phys. Chem. B* 114.5 (2010), p. 1954.

[205] A Luzar and D Chandler. *Application of the Reactive Flux Formalism to Study Water Hydrogen Bond Dynamics. In: Bellissent-Funel MC., Dore J. C. (eds) Hydrogen Bond Networks*. Vol. 435. Springer, Dordrecht, 1994.

[206] S. Yadav, A. Choudhary, and A. Chandra. “A First-Principles Molecular Dynamics Study of the Solvation Shell Structure, Vibrational Spectra, Polarity, and Dynamics around a Nitrate Ion in Aqueous Solution”. In: *J. Phys. Chem. B* 121 (2017), pp. 9032–9044.

[207] P. L. Silvestrelli and M. Parrinello. “Water Molecule Dipole in the Gas and in the Liquid Phase”. In: *Phys. Rev. Lett.* 82.16 (1999), pp. 3308–3311. DOI: `https://doi.org/10.1103/PhysRevLett.82.3308`. URL: `https://journals.aps.org/prl/abstract/10.1103/PhysRevLett.82.3308`.

[208] E. B. Wilson. *Molecular Vibrations*. New York: McGraw-Hill Book Company, Inc., 1955.

[209] E. A. Carter et al. “Constrained Reaction Coordinate Dynamics for the Simulation of Rare Events”. In: *Chem. Phys. Lett.* 156 (1989), p. 472. DOI: `10.1016/S0009-2614(89)87314-2`. URL: `https://www.sciencedirect.com/science/article/abs/pii/S0009261489873142`.

[210] M. Sprik and G. Ciccotti. “Free Energy from Constrained Molecular Dynamics”. In: *J. Chem. Phys.* 109 (1998), pp. 7737–7744. DOI: `10.1063/1.477419`. URL: `https://ui.adsabs.harvard.edu/abs/1998JChPh.109.7737S`.

[211] Paul C. Hiemenz and Raj. Rajagopalan. *Principles of Colloid and Surface Chemistry.* 3rd ed. New York: Marcel Dekker, Inc, 1997.

[212] M. Ferrario, M. Haughney, and R. McDonald M. L. Klein. “Molecular-Dynamics Simulation of Aqueous Mixtures: Methanol Acetone, and Ammonia”. In: *J. Chem. Phys.* 93 (1990), p. 5156. DOI: `10.1063/1.458652`. URL: `https://aip.scitation.org/doi/abs/10.1063/1.458652`.

[213] Raymond D. Mountain. “Comparison of a Fixed-Charge and a Polarizable Water Model”. In: *J. Chem. Phys.* 103.8 (1995), pp. 3084–3090. DOI: `10.1063/1.470497`. eprint: `https://doi.org/10.1063/1.470497`. URL: `https://doi.org/10.1063/1.470497`.

[214] L. J. Root and B. J. Berne. “Effect of Pressure on Hydrogen Bonding in Glycerol: A Molecular Dynamics Investigation”. In: *J. Chem. Phys.* 107 (1997), pp. 4350–4357. DOI: `10.1063/1.474776`. URL: `https://doi.org/10.1063/1.474776`.

[215] L. D. Landau and E. M. Lifshitz. *Statistical Physics: Part 1.* Elsevier Ltd, 3rd ed, 1980.